The EUMETSAT Network of Satellite Application Facilities

ROM SAF
Radio Occultation Meteorology

ROM SAF CDOP-2

Visiting Scientist Report 20:

Statistical analysis of systematic errors in RO measurements

Michael Gorbunov

Danish Meteorological Institute (DMI)
European Centre for Medium-Range Weather Forecasts (ECMWF)
Institut d'Estudis Espacials de Catalunya (IEEC)
Met Office (METO)

Ref: SAF/ROM/DMI/REP/VS20/001
Version: 1.0
Date: 11 March 2014

DOCUMENT AUTHOR TABLE

	Author(s)	*Function*	*Date*	*Comment*
Prepared by:	Michael Gorbunov	ROM SAF Visiting Scientist	30/01/2014	
Reviewed by (internal):	Stig Syndergaard	ROM SAF Scientist	24/02/2014	
Approved by:	Kent B. Lauritsen	ROM SAF Project Manager	24/02/2014	

DOCUMENT CHANGE RECORD

Issue/Revision	*Date*	*By*	*Description*
Draft 1	30/01/2014	MG	First draft
Draft 2	07/03/2014	MG	Second revision
1.0	11/03/2014	MG	Final version
1.1	30/11/2014	MG	Updated acknowledgements

VS Author

This VS study was carried out by Dr. Michael Gorbunov, IAP, Moscow, Russia; Email: michael.gorbunov@zmaw.de

VS Duration

The VS study was performed during October – December 2013 at the home institute of the candidate and with a three weeks visit to DMI during October 2013.

ROM SAF

The Radio Occultation Meteorology Satellite Application Facility (ROM SAF) is a decentralized processing center under EUMETSAT which is responsible for operational processing of GRAS radio occultation data from the Metop satellites and radio occultation (RO) data from other missions. The ROM SAF delivers bending angle, refractivity, temperature, pressure, and humidity profiles in near-real time and offline for NWP and climate users. The offline profiles are further processed into climate products consisting of gridded monthly zonal means of bending angle, refractivity, temperature, humidity, and geopotential heights together with error descriptions.

The ROM SAF also maintains the Radio Occultation Processing Package (ROPP) which contains software modules that will aid users wishing to process, quality-control and assimilate radio occultation data from any radio occultation mission into NWP and other models.

The ROM SAF Leading Entity is the Danish Meteorological Institute (DMI), with Cooperating Entities: i) European Centre for Medium-Range Weather Forecasts (ECMWF) in Reading, United Kingdom, ii) Institut D'Estudis Espacials de Catalunya (IEEC) in Barcelona, Spain, and iii) Met Office in Exeter, United Kingdom. To get access to our products or to read more about the ROM SAF please go to: http://www.romsaf.org

Intellectual Property Rights

All intellectual property rights of the ROM SAF products belong to EUMETSAT. The use of these products is granted to every interested user, free of charge. If you wish to use these products, EUMETSAT's copyright credit must be shown by displaying the words “copyright (year) EUMETSAT” on each of the products used.

List of Contents

Executive Summary

This VS study has the following objectives:

O1. Perform a detailed statistical analysis of COSMIC RO data for year 2008 and, eventually, 2009 and GRAS data for years 2009 and 2010 and compare the retrieved refractivity with corresponding ECMWF re-analyses; include analysis of bending angles for selected regions;

O2. Perform realistic simulations of RO observations using the Wave Optics Propagator (WOP) from the WOP ITT study [25]; realistic simulations will be performed for 4 days from different seasons.

The following tasks were found necessary for the implementation of the project are the following:

T1. Setting up the automated processing of large array of RO data from GRAS and COSMIC missions;

T2. Statistical analysis of inversions of COSMIC data for year 2008 and, eventually, 2009 and GRAS data for years 2009 and 2010 with a detailed regionalization for different lat-lon bands, seasons and, eventually, daytime;

T3. Optimization of WOP package for the simulation of small scale isotropic and anisotropic turbulence;

T4. Simulation of RO data for 4 days from different seasons using a model including regular horizontally non-uniform atmosphere and atmospheric turbulence;

T5. Inversions and statistical analysis of artificial RO data.

T6. Perform a statistical analysis and comparison of realistic (idealised) simulations and bending angle and refractivity retrievals and describe and discuss the results in the final report;

T7. The EUMETSAT WOP ITT study introduced a set of four categories for atmospheric conditions which should be used in the present VS project. The 50+ data set used in that study should be included in the larger data set to be used in the present VS project.

T8. Select high resolution radiosondes for selected regions (and categories) from the University Wyoming database and use them in the simulation and comparison studies under task T6.

In this study we performed detailed regionalized statistical analysis of COSMIC and GRAS radio occultation (RO) observation. The analysis included comparison of retrieved refractivities and bending angles with background ECMWF data. Background bending angles were simulated using the Wave Optics Propagator (WOP) package developed by M. Gorbunov [15]. COSMIC, GRAS, and simulated RO data were processed by OCC package developed by M. Gorbunov [16]. Simulations included turbulence model. It was demonstrated that, along with super-refraction in marine boundary layer concentrated in a few relatively narrow areas, a systematic error of refractivity retrievals is also caused by

random turbulence. Simple theoretical considerations show that the effect of turbulence must be negative, which agrees with the observations. We performed a statistical analysis of the 55 cases chosen for the previous EUMETSAT WOP-ITT study aimed at the optimization of occultation tracking strategy [25]. It was found that the tropical WOP-ITT cases are located in super-refraction areas. We performed a series of simulations with tropical radiosondes. It was shown that such simulations may overestimate the negative systematic retrieval error in the height range of 1–3 km. On the other hand, simulation based ECMWF with turbulence provide a more realistic patter of N-bias that significantly increase in the lowest 1 km.

1. Introduction

1.1 Purpose of Document

This document contains the results from the ROM SAF Visiting Scientist activity on the statistical investigation of negative bias of refractivity and bending angles retrieved from RO observations.

The document is organized as follows: Chapter 2 describes the statistical analysis of COSMIC-retrieved refractivities and bending angles with a detailed regionalization, both for the whole year and for separate seasons. Chapter 3 describes a similar analysis of GRAS/METOP observations. Chapter 4 describes the results of end-to-end numerical simulations performed by WOP package on the basis of ECMWF analyses with a superimposed turbulence model. Chapter 5 presents a statistical analysis of 55 cases used in the WOP-ITT study [25]. Chapter 6 describes end-to-end numerical simulations made on the material of radiosonde observations. In Chapter 7 we offer our conclusions.

1.2 Introduction

Radio occultations (RO) are nowadays commonly accepted as one of the most powerful techniques of sounding the Earth's atmosphere for purposes of numerical weather prediction and monitoring global climate change. Advantages of RO are well-known: stability, no necessity for calibration, low cost, global coverage, all-weather capability, high vertical resolution. Nevertheless, this technique has some drawbacks: low horizontal resolution, sensitivity to residual ionospheric noise above 30 km, systematic errors in the lower troposphere. In this report, we will statistically analyze the systematic errors in the lower troposphere.
The general scheme of RO observation can be summarized as follows. The satellite borne receiver observes the electromagnetic waves originating from a GPS satellite and propagating through the atmosphere. The observations are transformed into amplitude and phase excess at a receiver-specific sampling rate (50 Hz for COSMIC and 1000 Hz for GRAS) and sent to ground stations. Ground-stations also collect GPS navigation bits needed for the correct demodulation of the signal. Processing of RO observations has the following basic steps: 1) derivation of bending angles from observed amplitudes and phase excesses, and 2) derivation of refractivity from bending angles. Both bending angles and refractivity profiles can then be assimilated into numerical weather prediction models.
There are different biases, which are introduced at different step of data acquisition and processing. Due to the observation geometry, there are limitations for the maximum value of observable bending angle [1]. This is explained by the fact that large bending angles require observations of signals with low amplitude at low elevation with respect to the planet limb. Such signals are susceptible to noise. Systematic loss of large bending angles manifests itself in a negative bias [1].
Even if the signal is correctly measured without a significant cut-off of low-amplitude fragments, bending angles may still be biased, because their derivation relies upon the assumption of low horizontal gradients, such that the bending angle as function of impact parameter is a single-valued function. This is the basic assumption of all the approaches based on Fourier Integral Operators (FIO): Back Propagation (BP) [2,3], Canonical

Transform (CT or CT2) [4,5,6], Full Spectrum Inversion (FSI) [9,10] and Phase Matching (PM) [11]. The aforementioned condition can be broken in presence of strong horizontal gradients of refractivity. In this case, FIO-derived bending angles may indicate a negative bias. The use of Wigner Distribution Function (WDF) was proposed in order to reduce this effect [7]. However, statistical analysis [8] did not indicate any significant reduction of the negative bias, which suggests that the role of this effect is not statistically significant.
Another factor that may result in biases are random fluctuations of atmospheric refractivity field, which are mapped into random fluctuations of amplitude and phase. Due to the non-linear nature of operators mapping refractivity to wave field and wave field to bending angle, random fluctuation will translate into a bias. In the main order, the bias is quadratic with respect to fluctuations. In particular, if the refractivity fluctuations are assumed to have Kolmogorov – von Kármán power-law spectrum characterized by the structural constant C_N^2, the bias should be proportional to C_N^2.
The inverse problem of the derivation of refractivity from bending angles only has a single solution, if the refractivity gradient does not exceed the critical value, which corresponds to the super-refraction conditions [12,13]. The use of the standard Abel inversion under the super-refraction conditions results in a negative bias, even with unbiased bending angles. Nevertheless, super-refraction results in sharp (formally infinity) spike of the bending angle. As noticed above, such sharp spikes are lost in bending angle retrievals. So super-refraction must also result in a negative bias of bending angle. An interesting study was presented in [14], where a detailed statistical analysis revealed relatively small regions over oceans with a significant negative bias attributed to super-refraction in marine boundary layer.
Because there are many factors resulting in biased bending angles, the statistical analysis of RO data must also be carried out on the level of bending angles. The means of such analysis are realistic forward numerical simulations using high-quality fields of atmospheric variables and wave-optics technique (WOP).
In this report, we describe our statistical analysis of COSMIC and GRAS/METOP data. We use the analysis fields of European Center for Medium Range Weather Prediction (ECMWF). The RO data are processed using the latest version of OCC program [16]. We also perform forward simulations using the WOP program [15], which implements the phase screen (split-step) method. The forward simulations are performed in two variants: without and with turbulence. In order to optimize simulations with a model of small-scale turbulence, we updated WOP by adding the capability of simulating realizations of fluctuation of the optical path between phase screens.

2. Statistical Analysis of COSMIC Observations

2.1 Whole Year Statistics

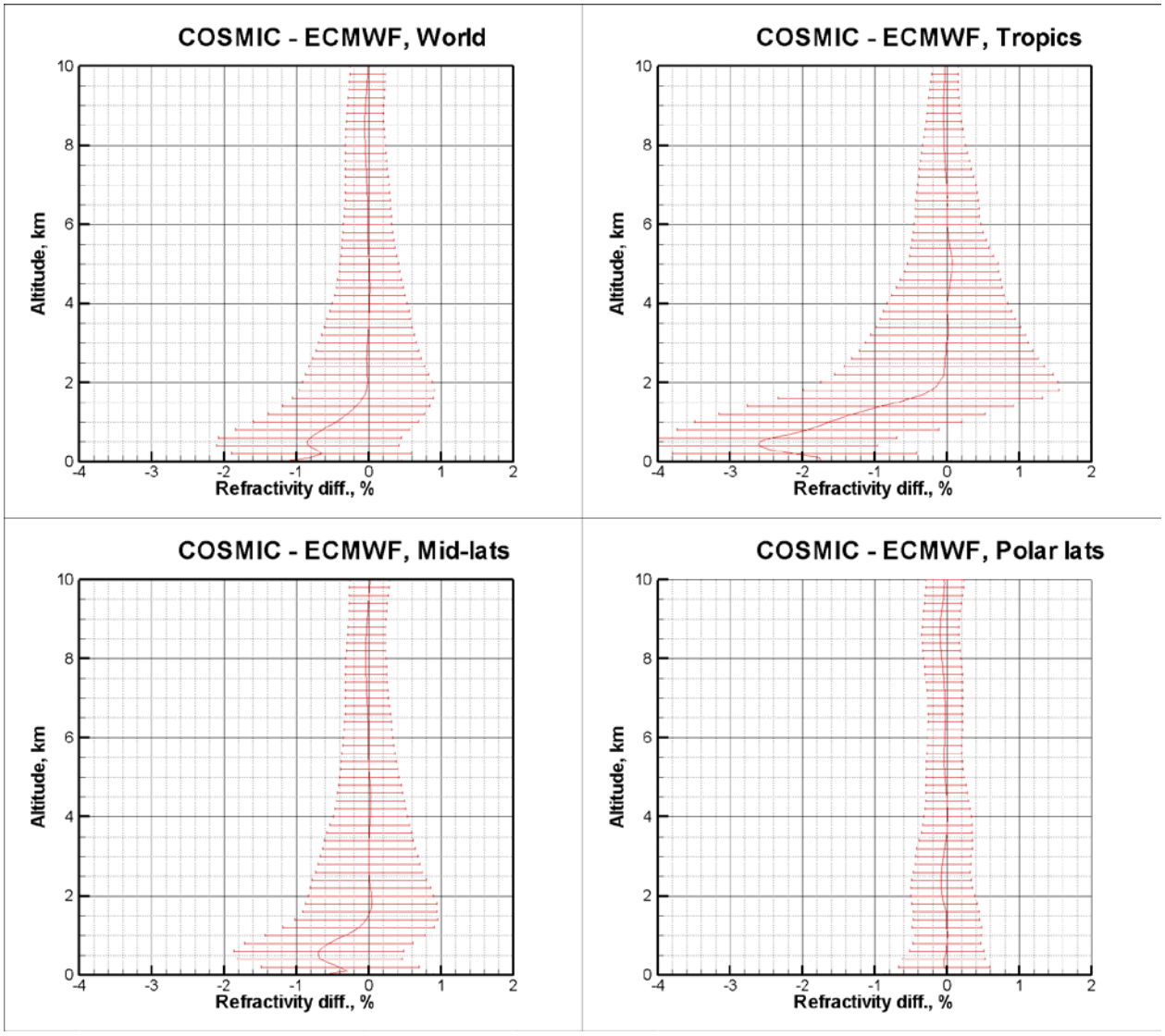

Fig. 1. Statistical comparison of refractivity from COSMIC observations and ECMWF analyses.

Fig. 1 presents the statistical comparison of refractivity derived from COSMIC with ECMWF analyses observations for year 2008. The ECMWF analyses are obtained by the assimilation of large number of different observation, also including COSMIC. In this comparisons, the background is understood as the local profile of refractivity derived from the ECMWF pressure, temperature, and humidity. The statistics is evaluated for a rough regionalization (tropics, mid-latitudes, and polar latitudes). The statistical results are similar to those presented in [16]. The negative bias of refractivity is observed below 2 km, and its larges values reaching −2.6% are located in tropics. In mid-latitudes the negative bias is below 1%, and it practically vanishes in polar latitudes.

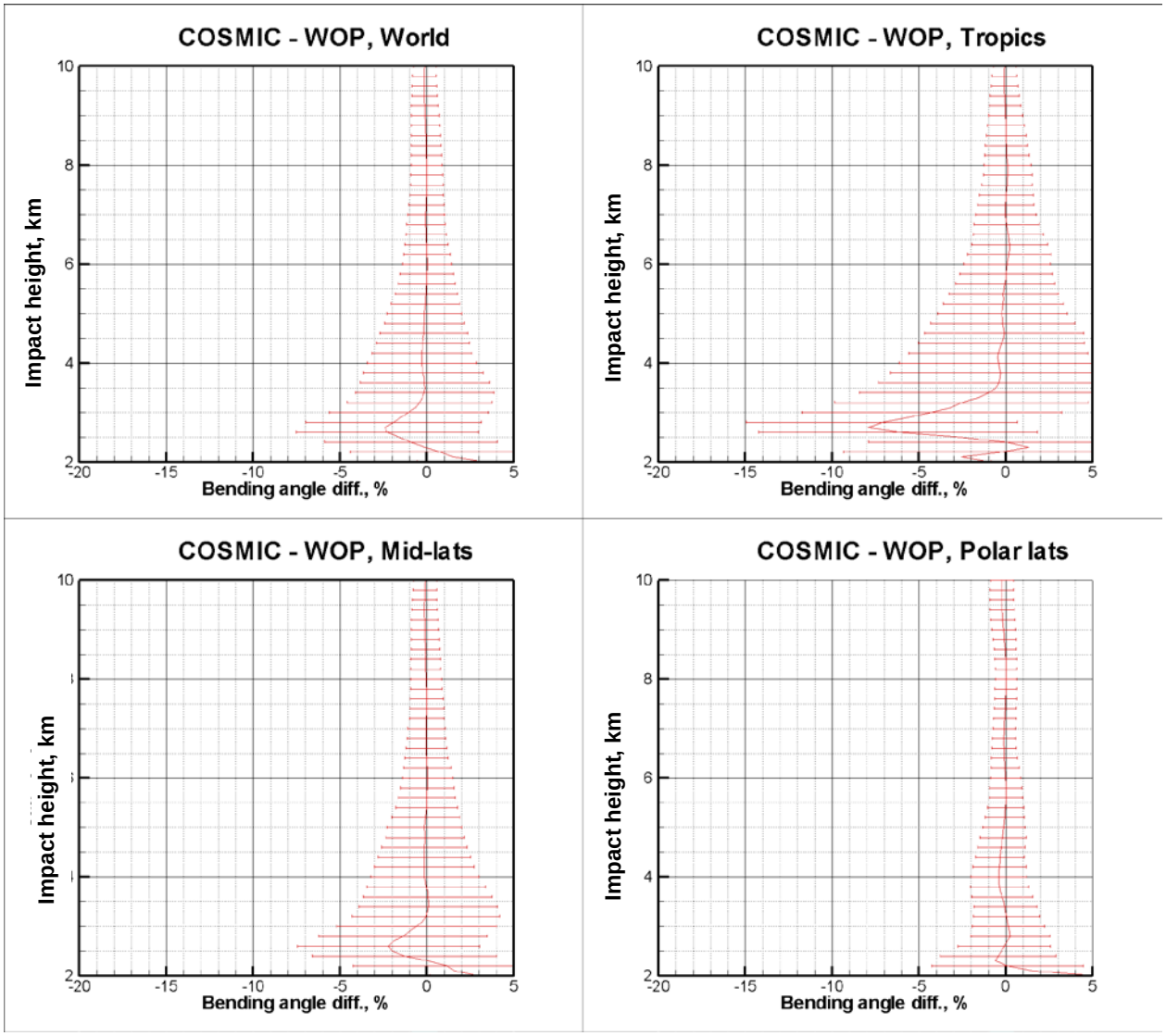

Fig. 2. Statistical comparison of bending angles from COSMIC observations and derived by WOP from ECMWF analyses. 10 days of year 2008.

Fig. 2 shows a similar statistical analysis of bending angles. The COSMIC bending angles hereinafter were obtained with the ionospheric correction and smoothing [17]. The background bending angles were obtained by means of forward wave optical simulation based on ECMWF analyses [18,19]. Bending angles are presented as function of impact height, defined as $p - R_E$, where p is the impact parameter and R_E is the local curvature radius of the cross-section of the Earth's reference ellipsoid by the occultation plane. The lowest value of the impact height corresponding to rays touching the Earth's surface is about 2 km. Vertical profiles of systematic deviation of observed bending angles from background values have a more complicated, alternating-sign structure. However, the negative-sign fragments prevail in the Abel integral inversion.

Fig. 3 through Fig. 12 present the detailed regionalized analysis of systematic differences of COSMIC and ECWMF refractivities at different altitudes. The altitudes are defined with respect to the geoid. The whole globe is subdivided into 36×36=1296 latitude-longitude bins with a size of 5°×10°.

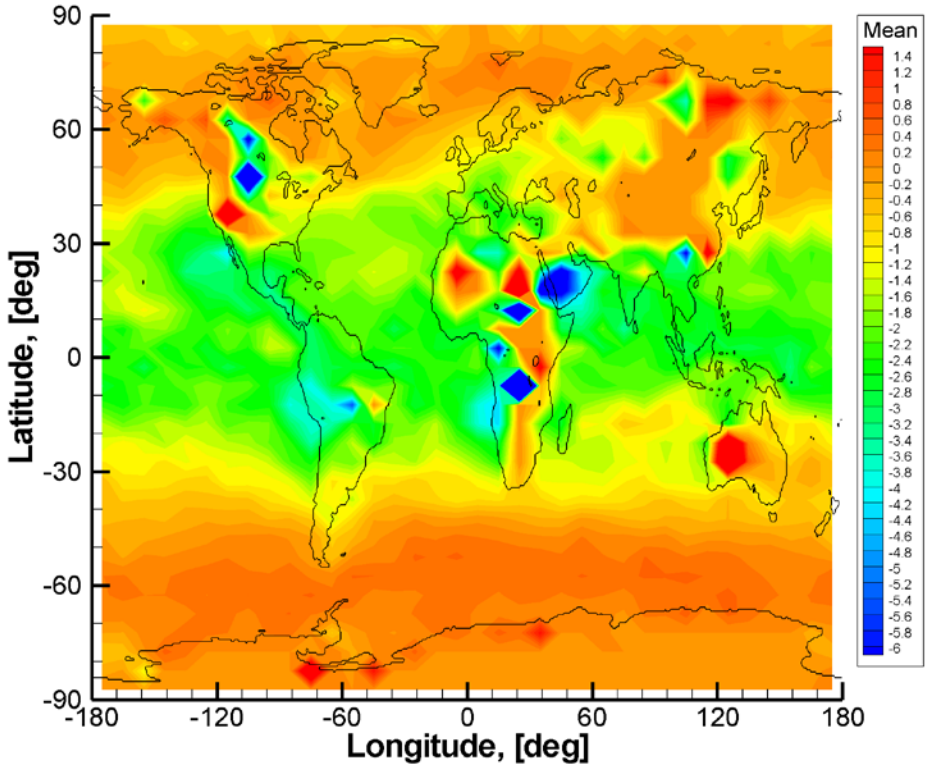

Fig. 3. Statistical comparison of COSMIC–ECMWF refractivities (O-B/B, %) at an altitude of 0.2 km.

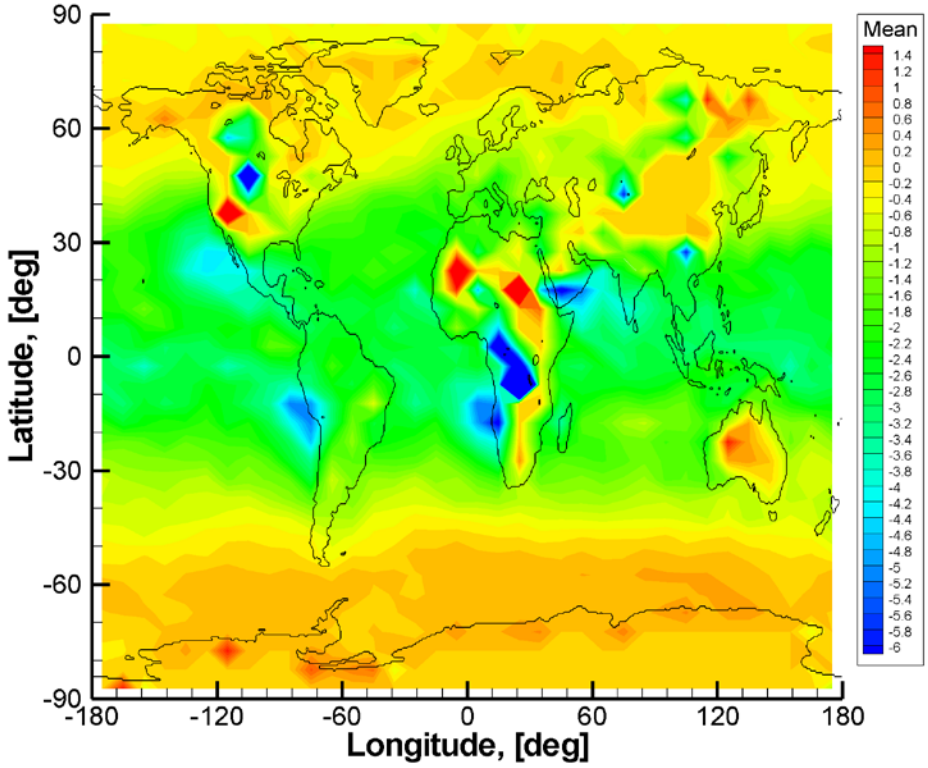

Fig. 4. Statistical comparison of COSMIC–ECMWF refractivities (O-B/B, %) at an altitude of 0.3 km.

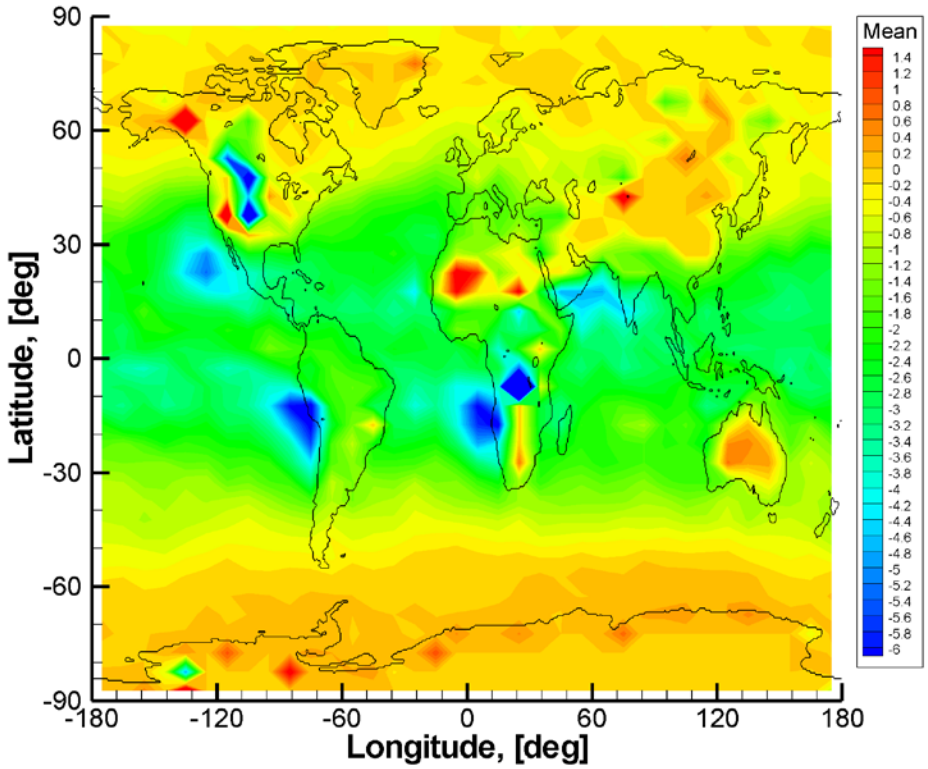

Fig. 5. Statistical comparison of COSMIC–ECMWF refractivities (O-B/B, %) at an altitude of 0.4 km.

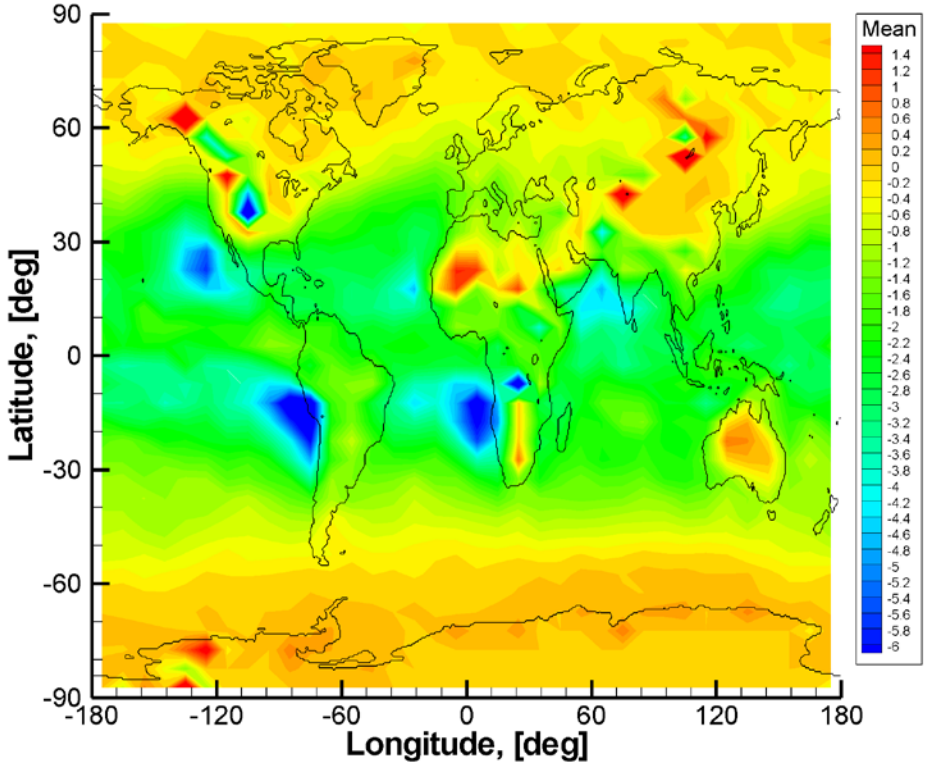

Fig. 6. Statistical comparison of COSMIC–ECMWF refractivities (O-B/B, %) at an altitude of 0.5 km.

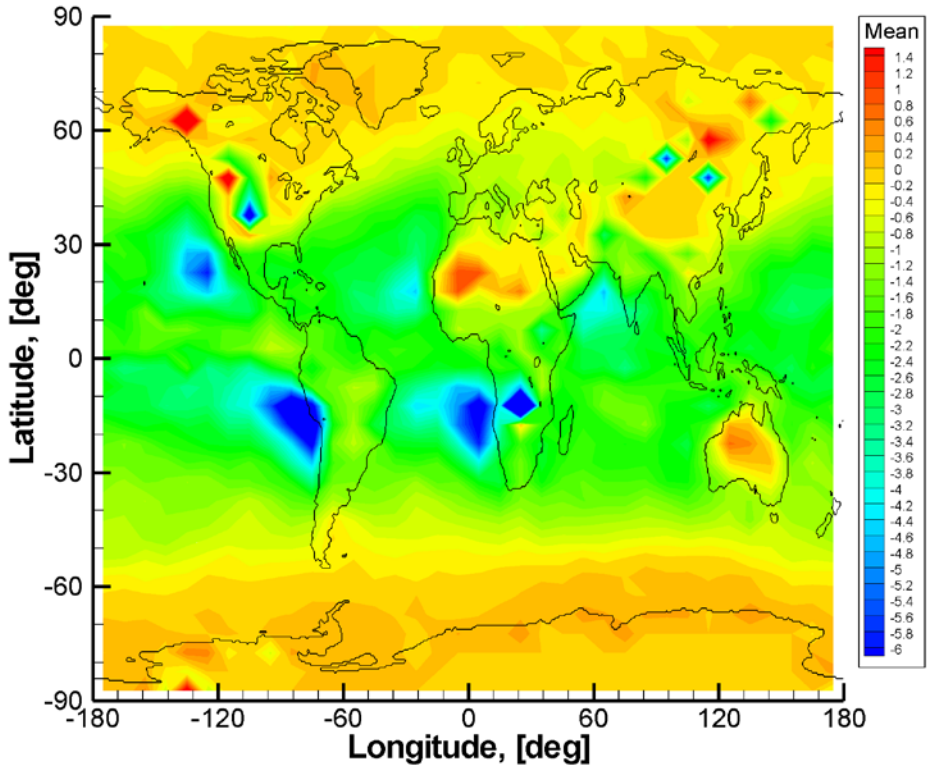

Fig. 7. Statistical comparison of COSMIC–ECMWF refractivities (O-B/B, %) at an altitude of 0.6 km.

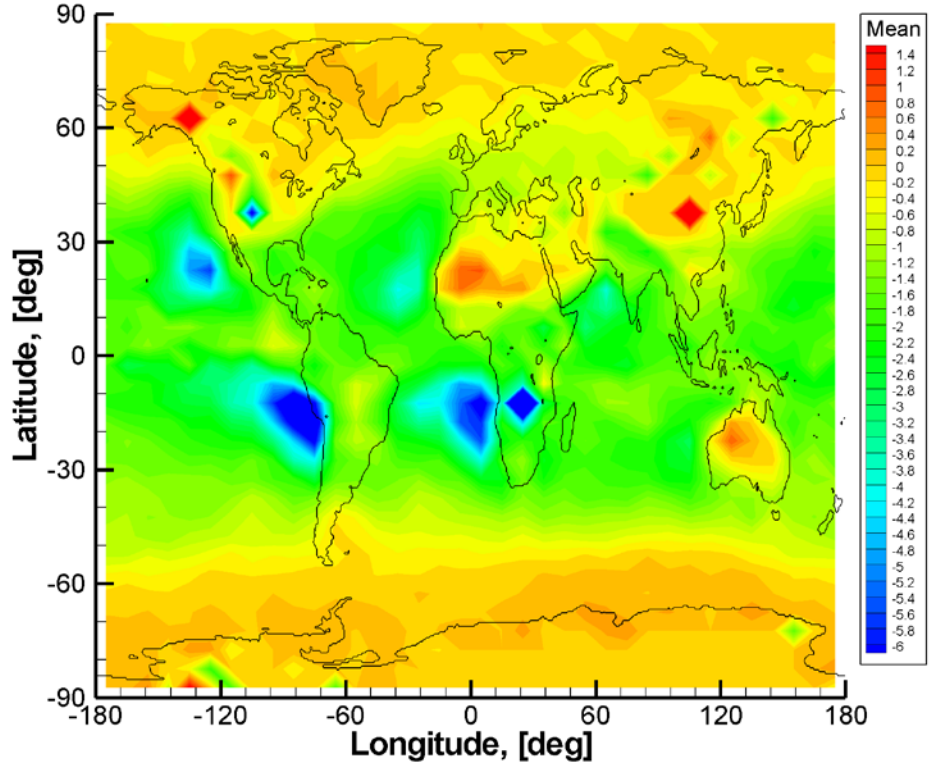

Fig. 8. Statistical comparison of COSMIC–ECMWF refractivities (O-B/B, %) at an altitude of 0.7 km.

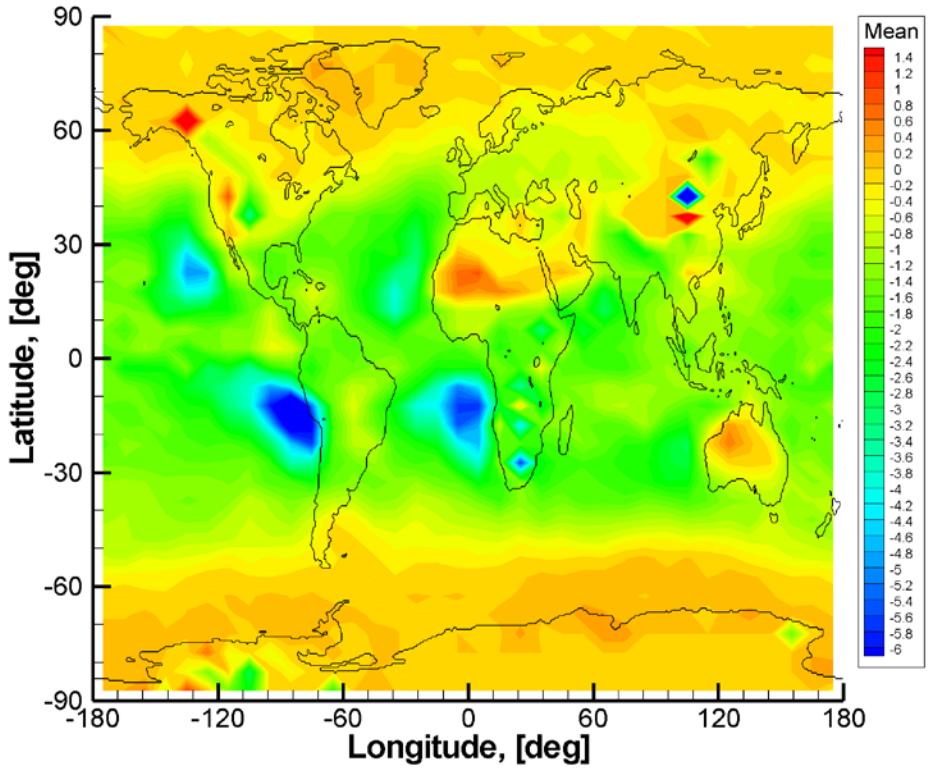

Fig. 9. Statistical comparison of COSMIC–ECMWF refractivities (O-B/B, %) at an altitude of 0.8 km.

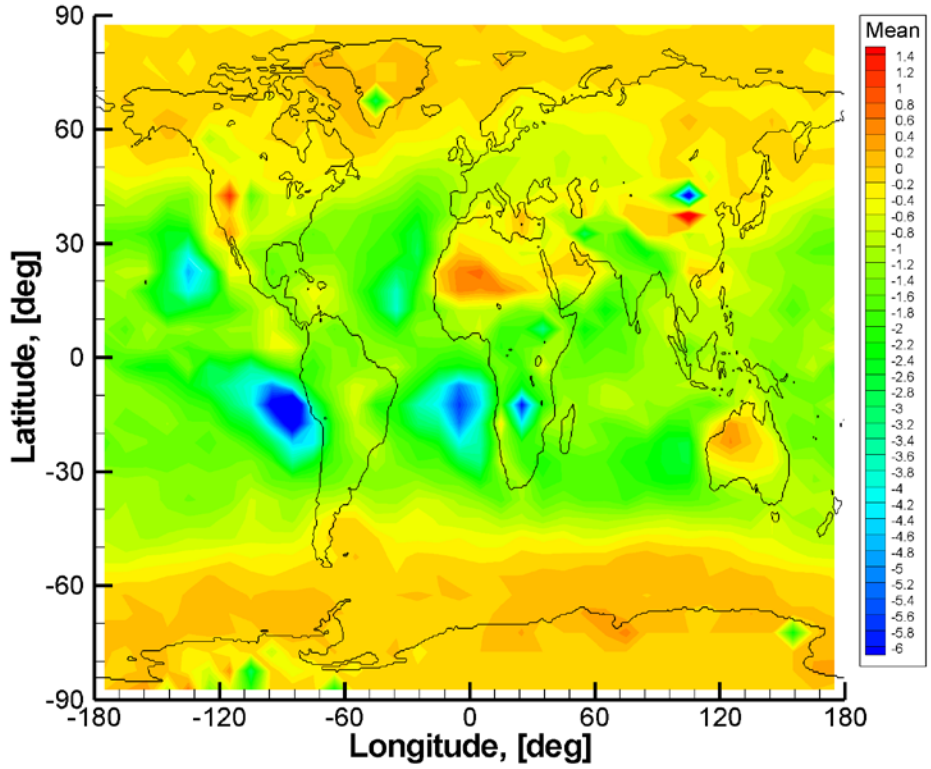

Fig. 10. Statistical comparison of COSMIC–ECMWF refractivities (O-B/B, %) at an altitude of 0.9 km.

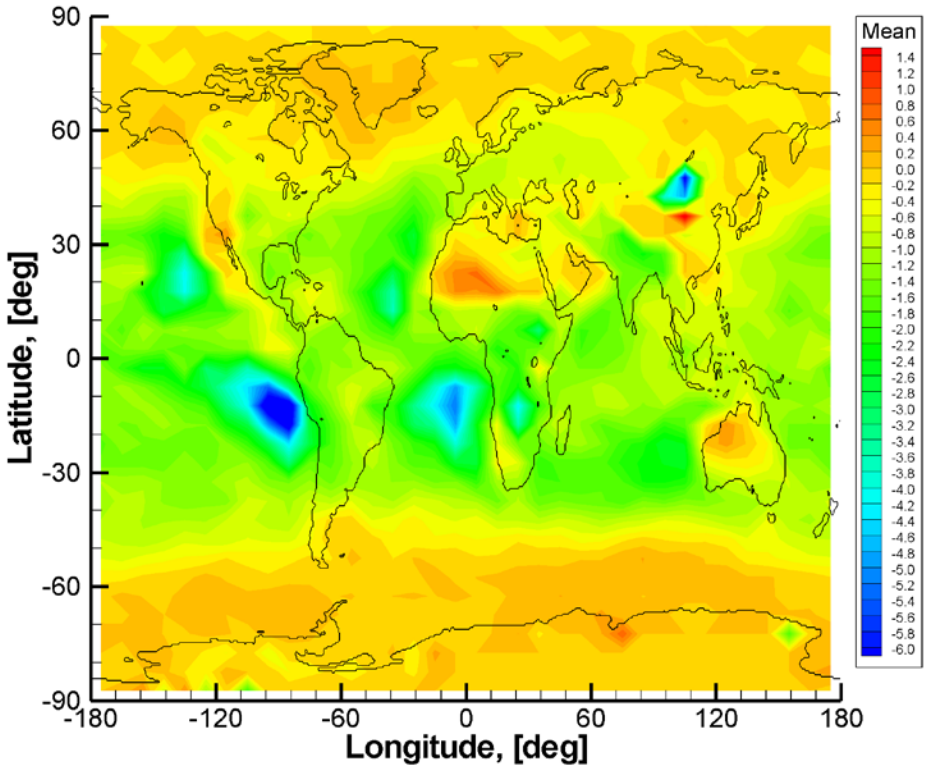

Fig. 11. Statistical comparison of COSMIC–ECMWF refractivities (O-B/B, %) at an altitude of 1.0 km.

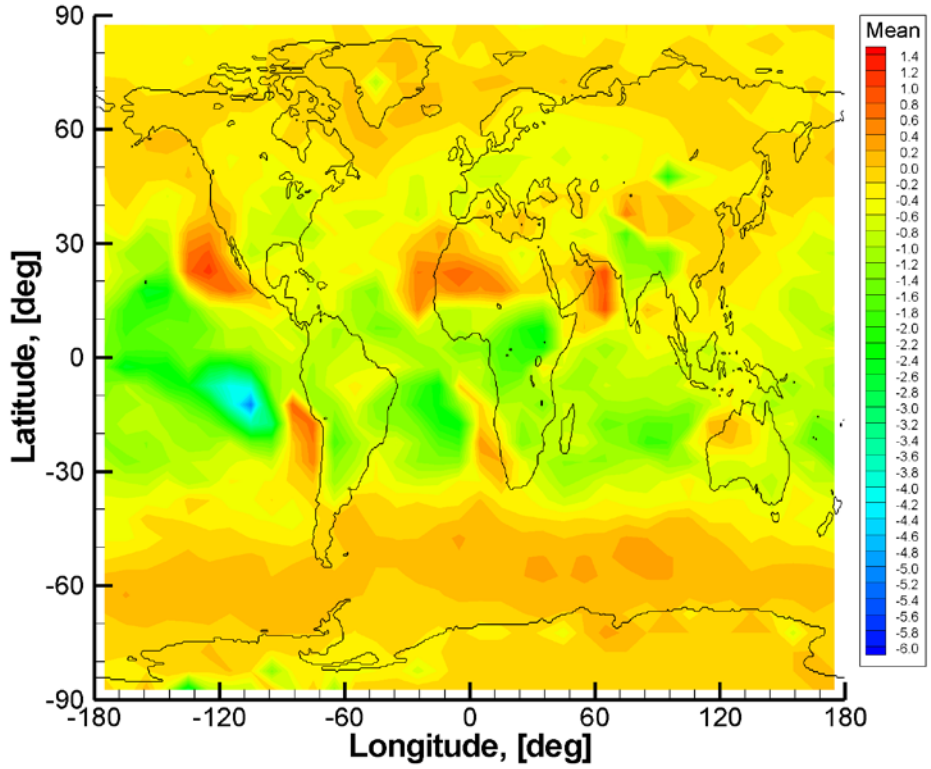

Fig. 12. Statistical comparison of COSMIC–ECMWF refractivities (O-B/B, %) at an altitude of 1.5 km.

At low altitudes, these plots indicate some outliers looking as diamonds centered at some of the grid points. They are explained by fluctuations due to a low number of observations in the corresponding meshes. The number of outliers decreases with the altitude.
The results are similar to those presented in [14]. The systematic difference COSMIC–ECMWF has a complicated structure. It has both areas with a pronounced negative bias and with a positive bias. The negative bias is attributed to strong super-refraction in marine boundary layer.
Fig. 13 through Fig. 22 show the numbers of data in each bin for different altitudes.

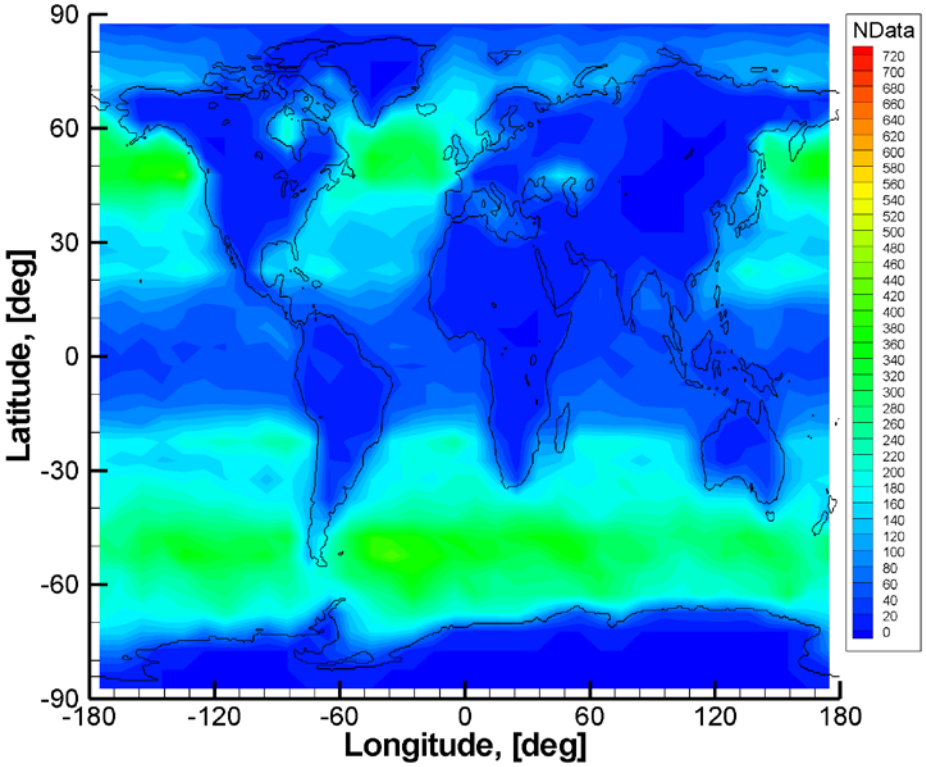

Fig. 13. Number of data for statistical comparison of COSMIC–ECMWF refractivities at an altitude of 0.2 km.

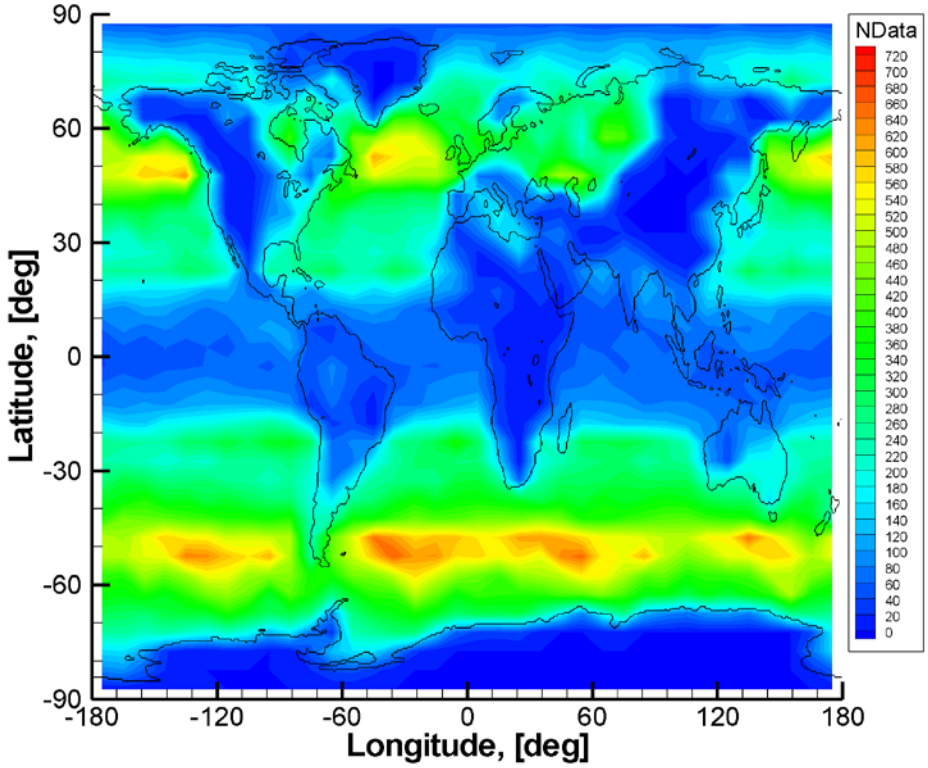

Fig. 14. Number of data for statistical comparison of COSMIC–ECMWF refractivities at an altitude of 0.5 km.

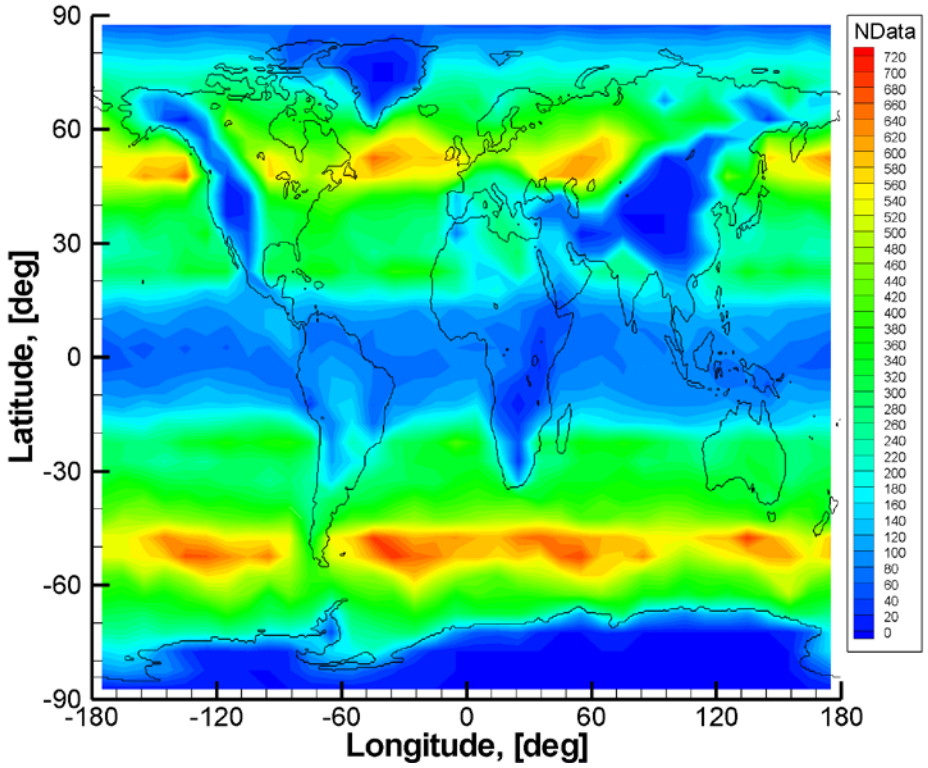

Fig. 15. Number of data for statistical comparison of COSMIC–ECMWF refractivities at an altitude of 1.0 km.

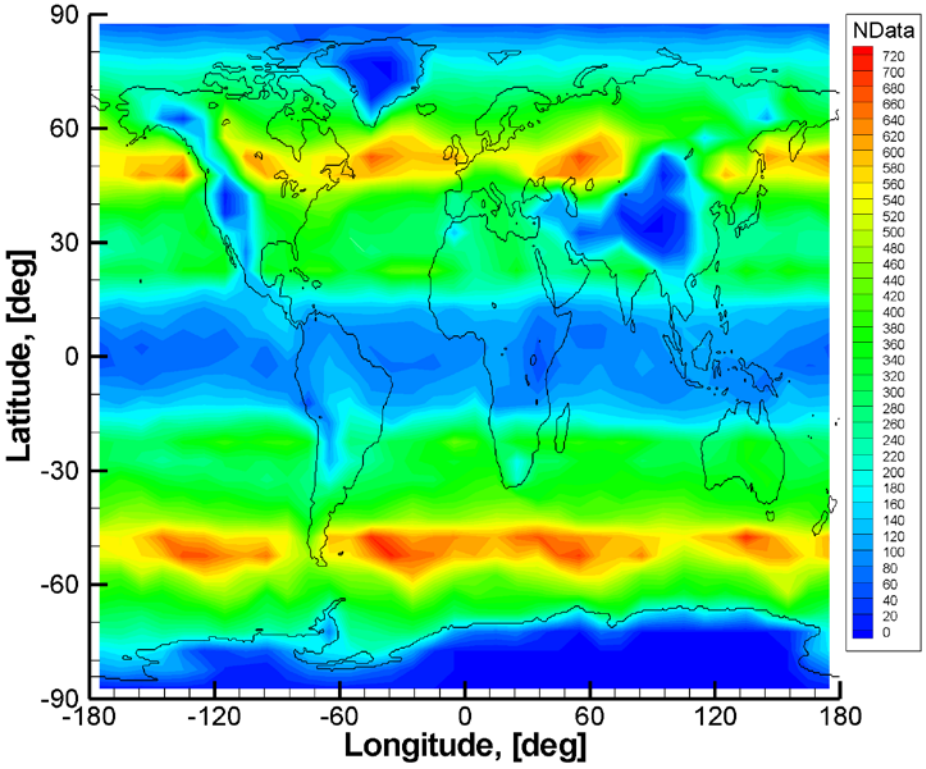

Fig. 16. Number of data for statistical comparison of COSMIC–ECMWF refractivities at an altitude of 1.5 km.

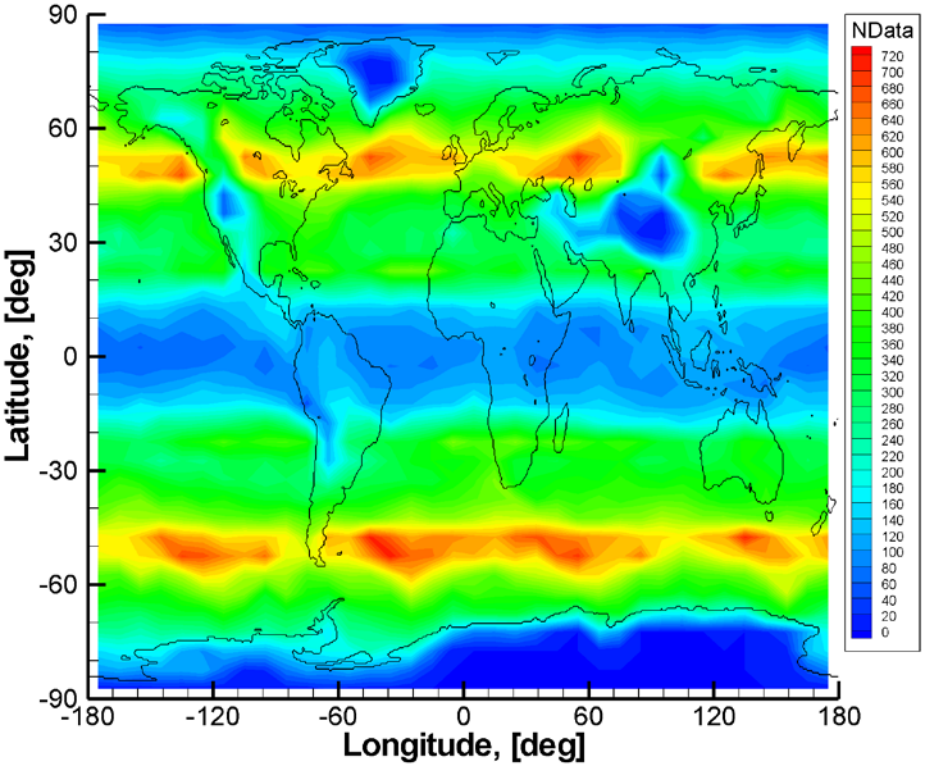

Fig. 17. Number of data for statistical comparison of COSMIC–ECMWF refractivities at an altitude of 2.0 km.

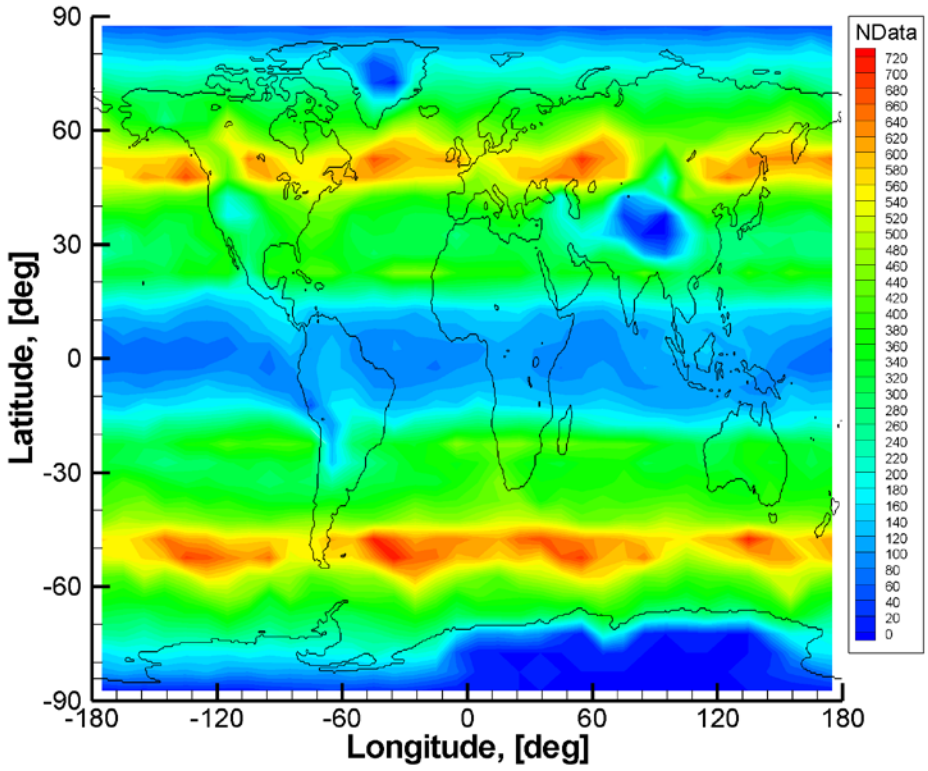

Fig. 18. Number of data for statistical comparison of COSMIC–ECMWF refractivities at an altitude of 2.5 km.

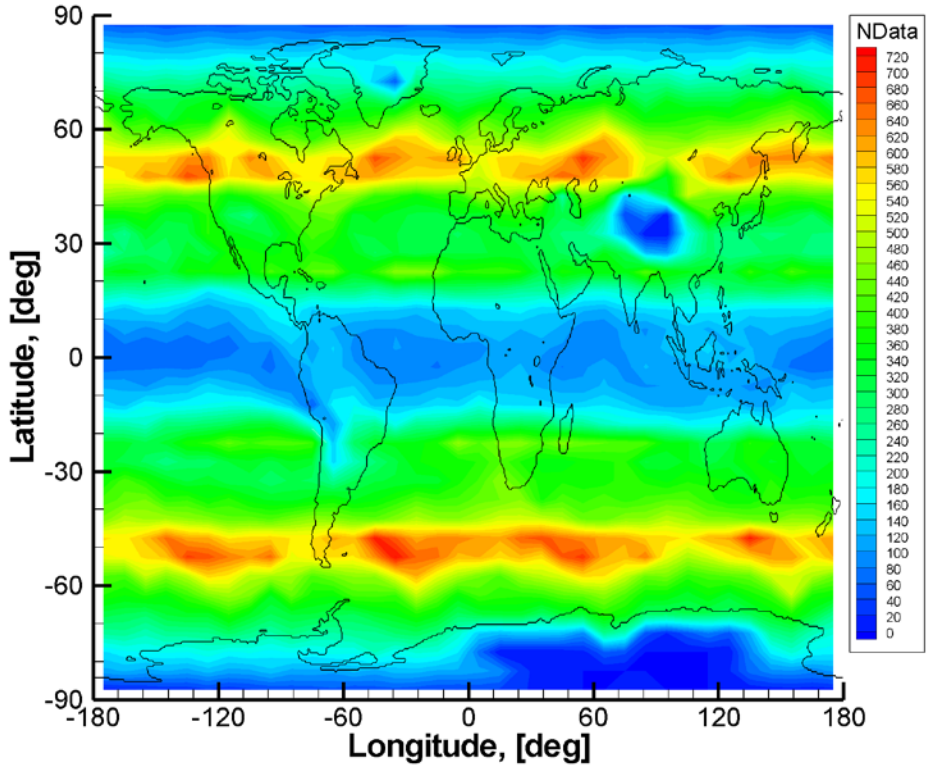

Fig. 19. Number of data for statistical comparison of COSMIC–ECMWF refractivities at an altitude of 3.0 km.

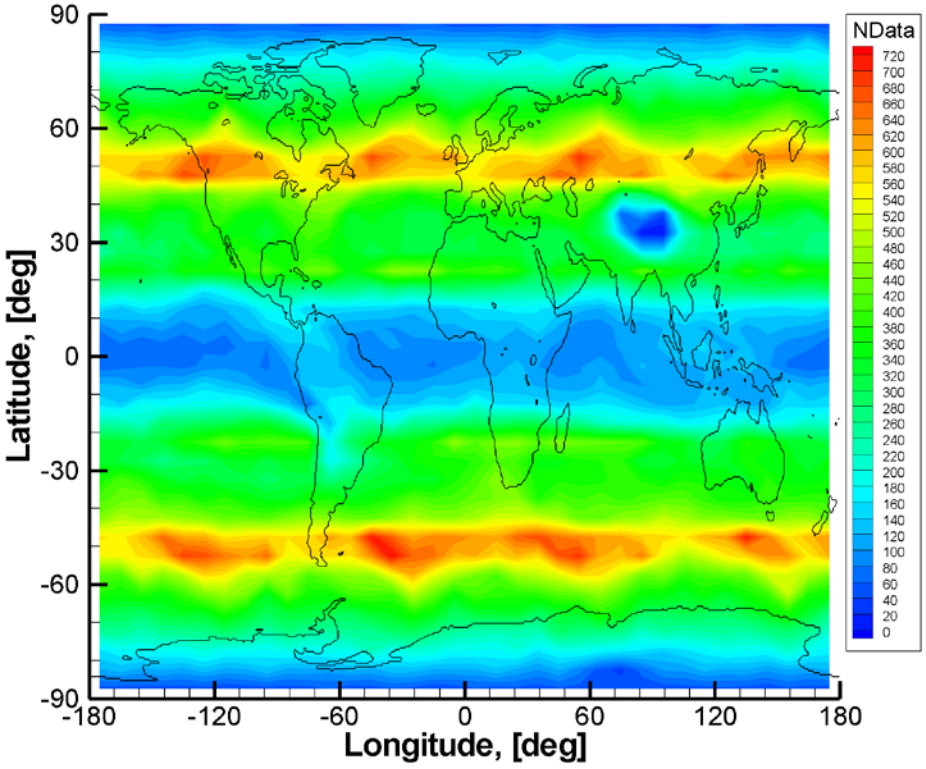

Fig. 20. Number of data for statistical comparison of COSMIC–ECMWF refractivities at an altitude of 4.0 km.

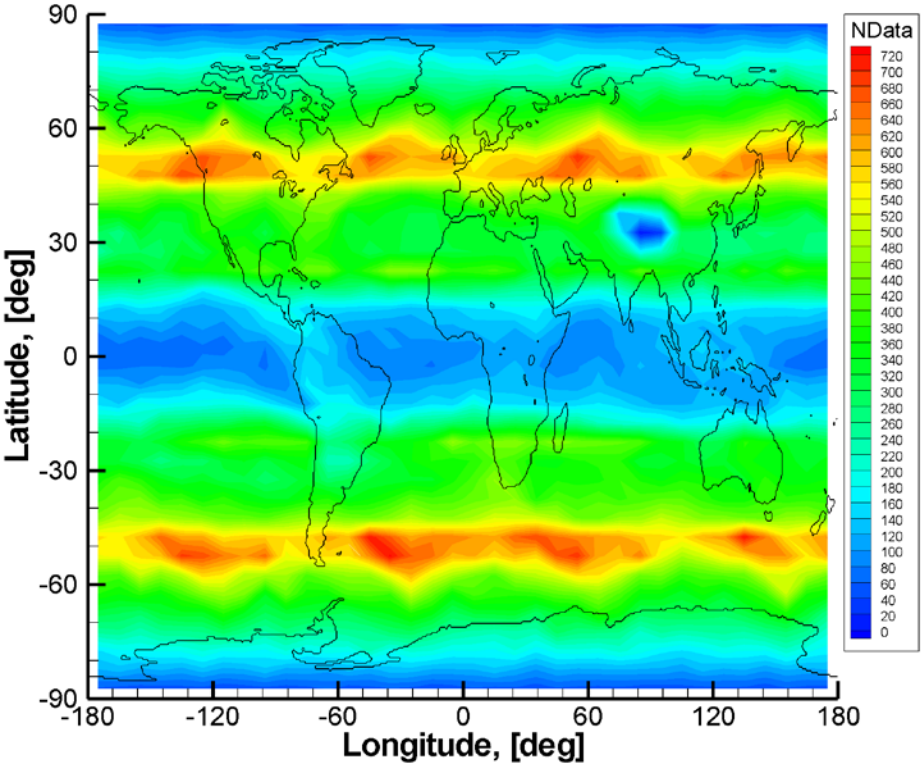

Fig. 21. Number of data for statistical comparison of COSMIC–ECMWF refractivities at an altitude of 5.0 km.

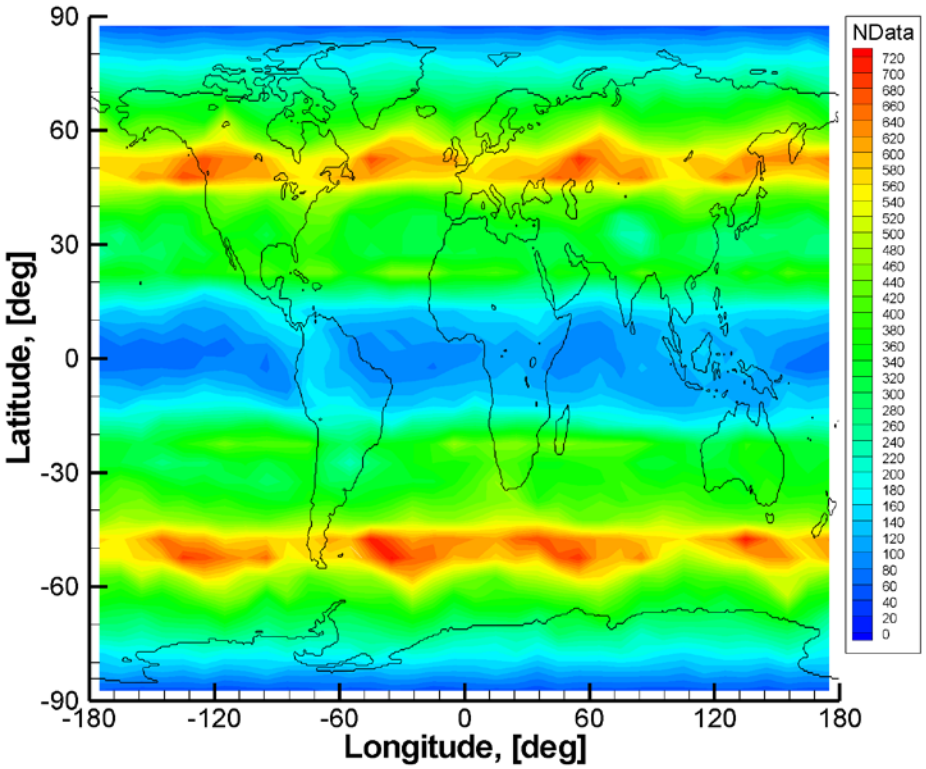

Fig. 22. Number of data for statistical comparison of COSMIC–ECMWF refractivities at an altitude of 6.0 km.

The number of data increases with altitude. It decreases in regions where the orography details like high mountains obscures observations. It also indicates global patterns defined by the COSMIC constellation geometry.
Fig. 23 through Fig. 35 present the statistical comparison of bending angles.

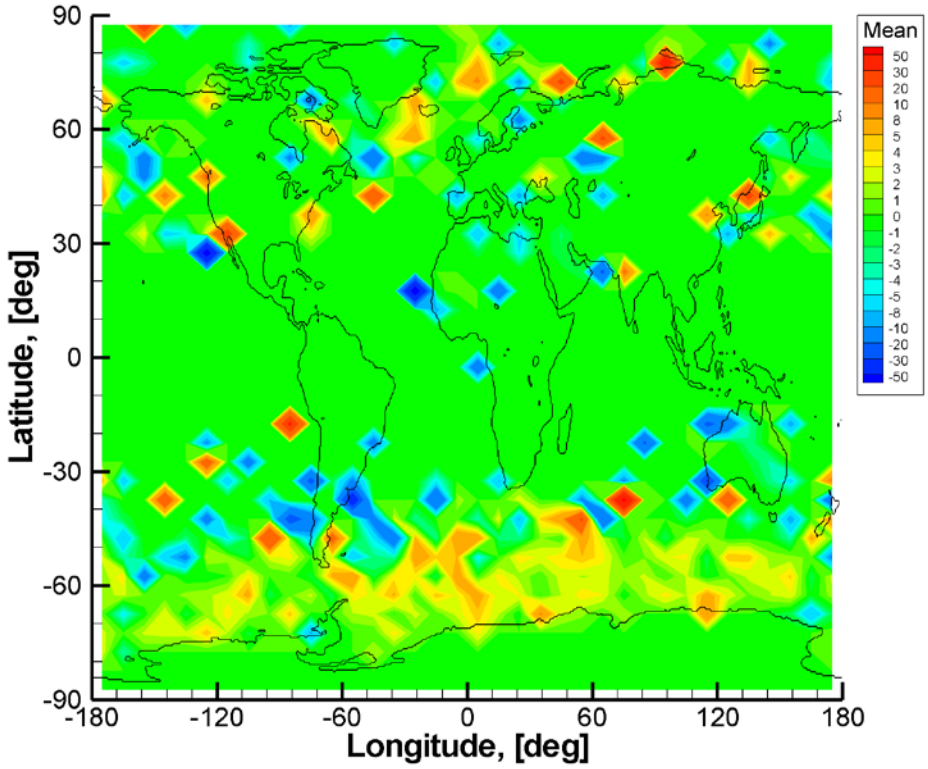

Fig. 23. Statistical comparison of COSMIC–ECMWF bending angles (O-B/B, %) at an impact height of 2.0 km.

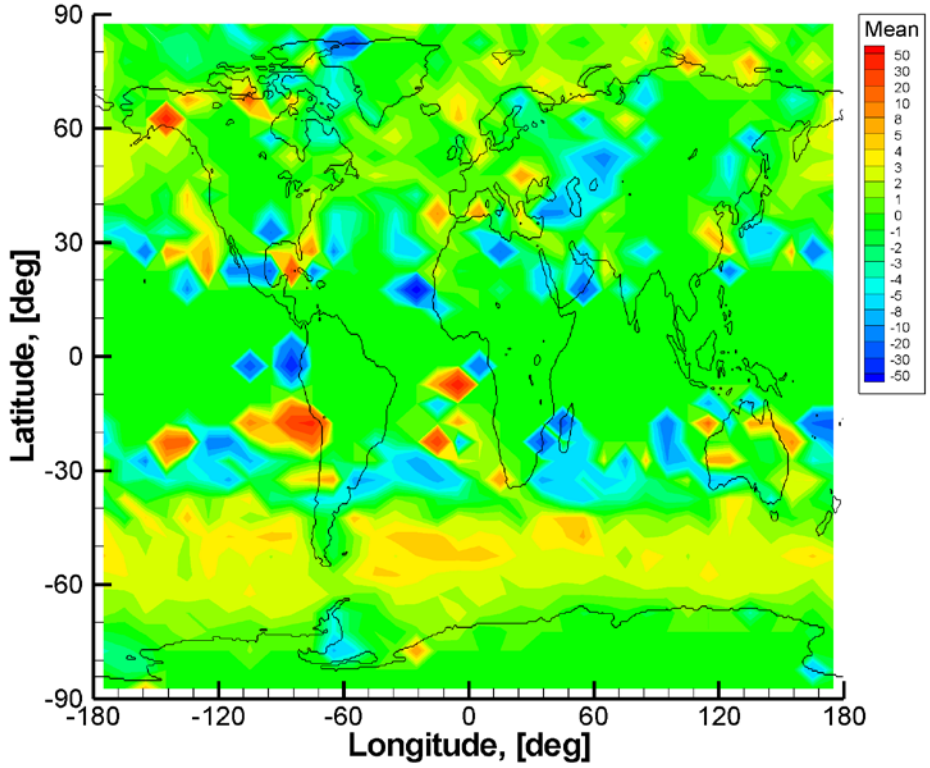

Fig. 24. Statistical comparison of COSMIC–ECMWF bending angles (O-B/B, %) at an impact height of 2.1 km.

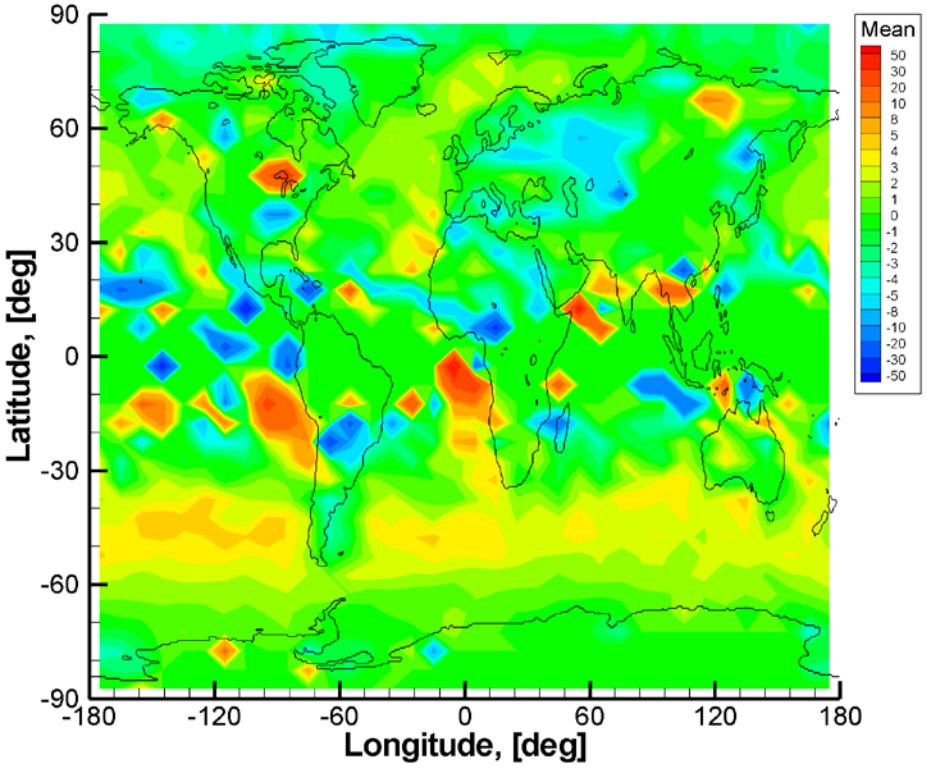

Fig. 25. Statistical comparison of COSMIC–ECMWF bending angles (O-B/B, %) at an impact height of 2.2 km.

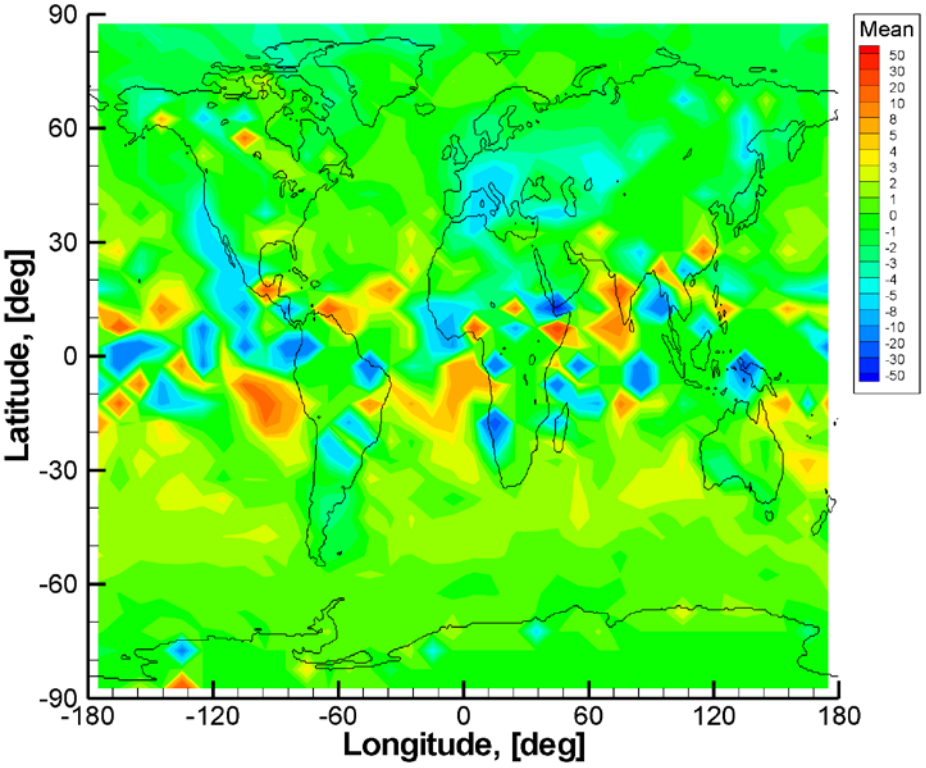

Fig. 26. Statistical comparison of COSMIC–ECMWF bending angles (O-B/B, %) at an impact height of 2.3 km.

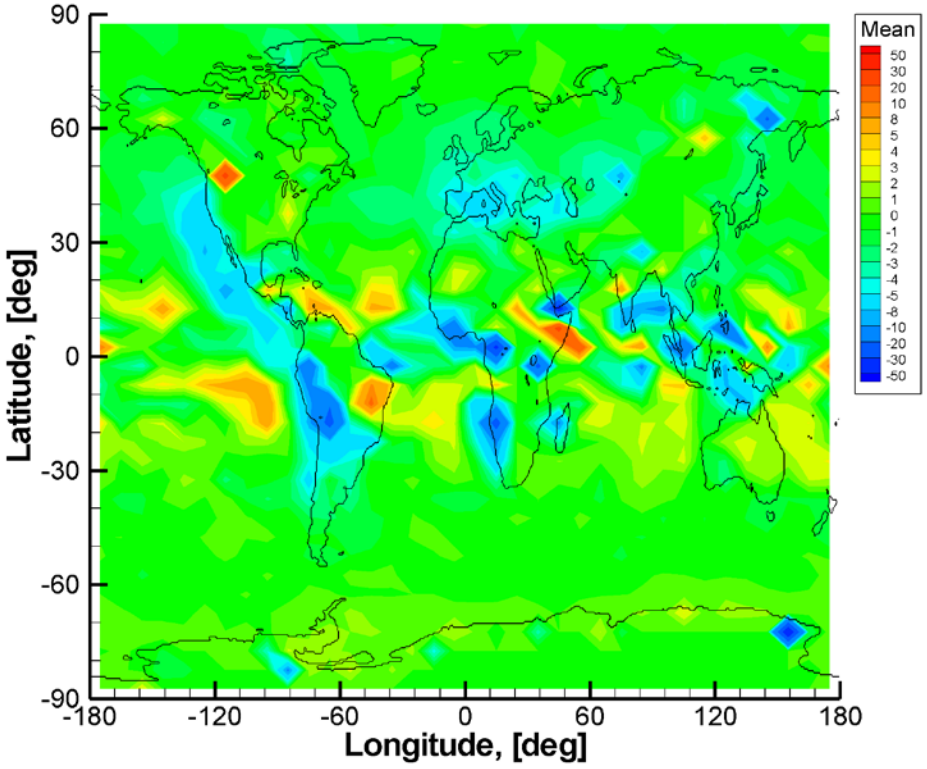

Fig. 27. Statistical comparison of COSMIC–ECMWF bending angles (O-B/B, %) at an impact height of 2.4 km.

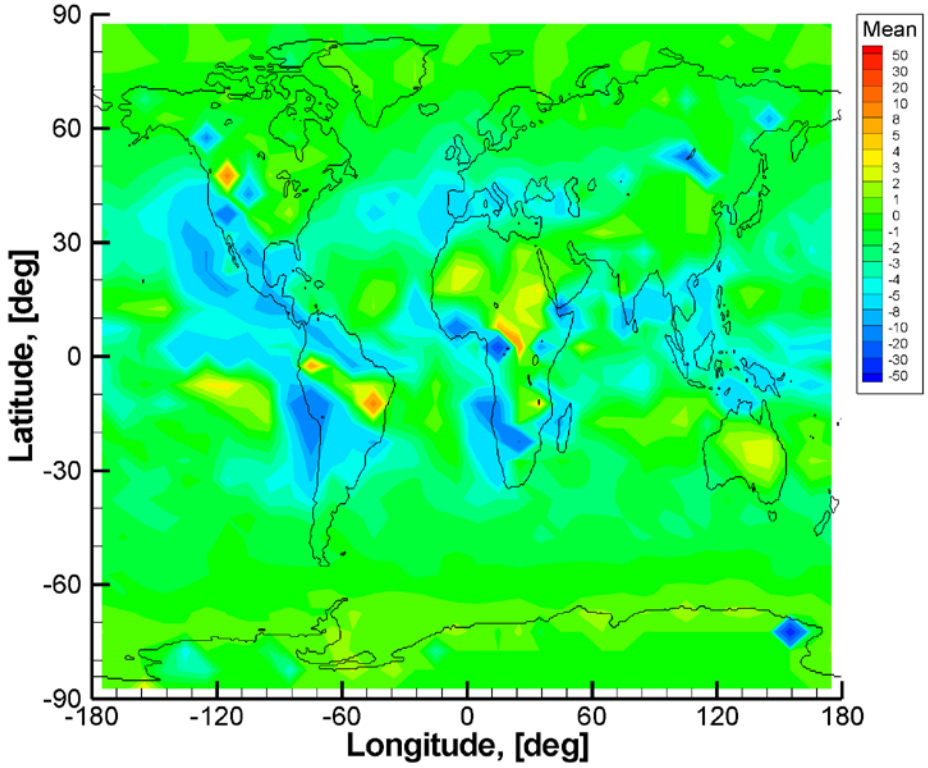

Fig. 28. Statistical comparison of COSMIC–ECMWF bending angles (O-B/B, %) at an impact height of 2.5 km.

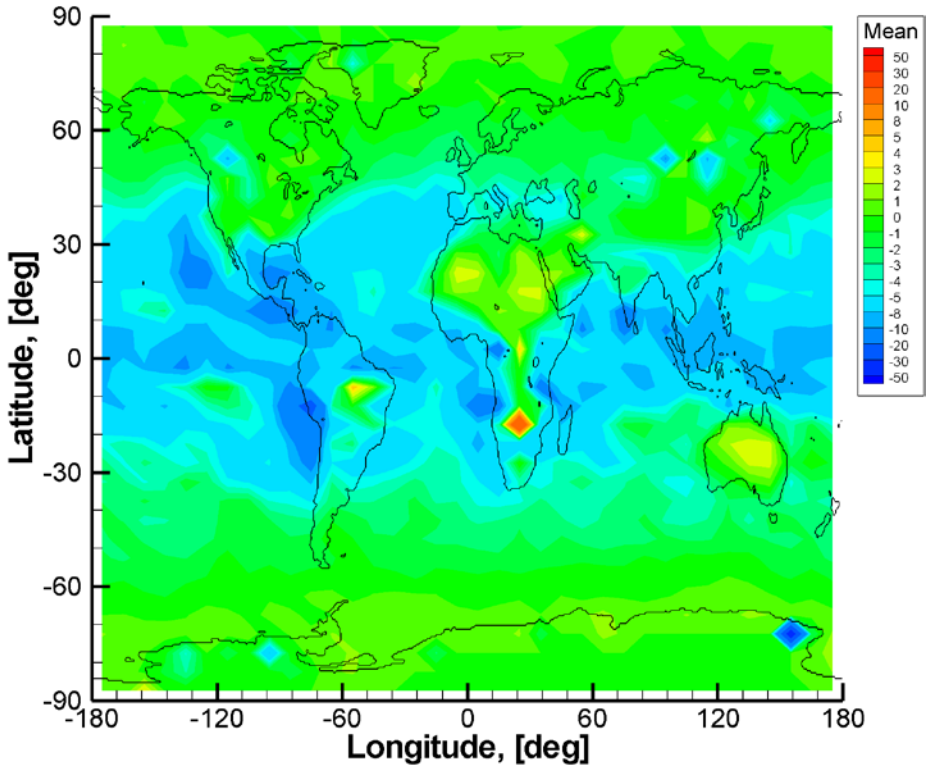

Fig. 29. Statistical comparison of COSMIC–ECMWF bending angles (O-B/B, %) at an impact height of 2.6 km.

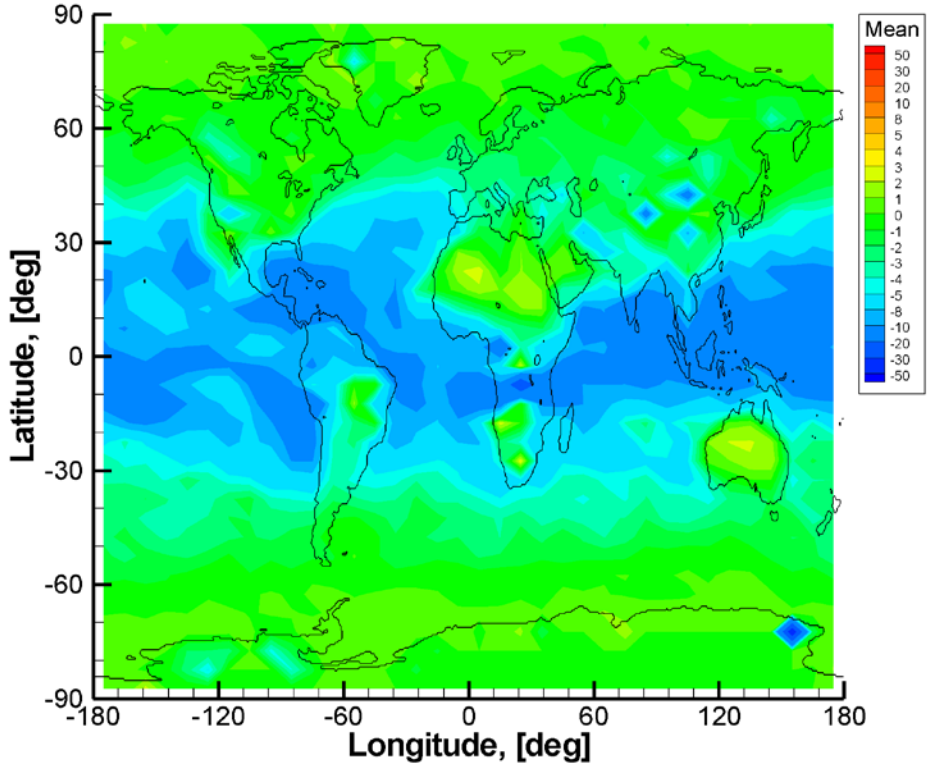

Fig. 30. Statistical comparison of COSMIC–ECMWF bending angles (O-B/B, %) at an impact height of 2.7 km.

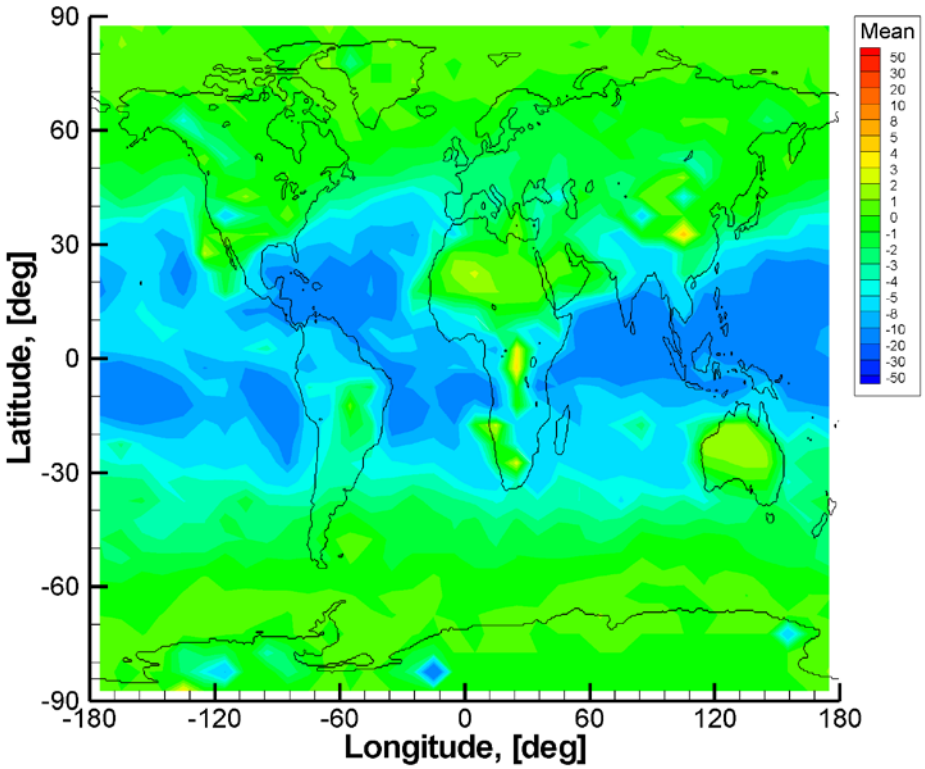

Fig. 31. Statistical comparison of COSMIC–ECMWF bending angles (O-B/B, %) at an impact height of 2.8 km.

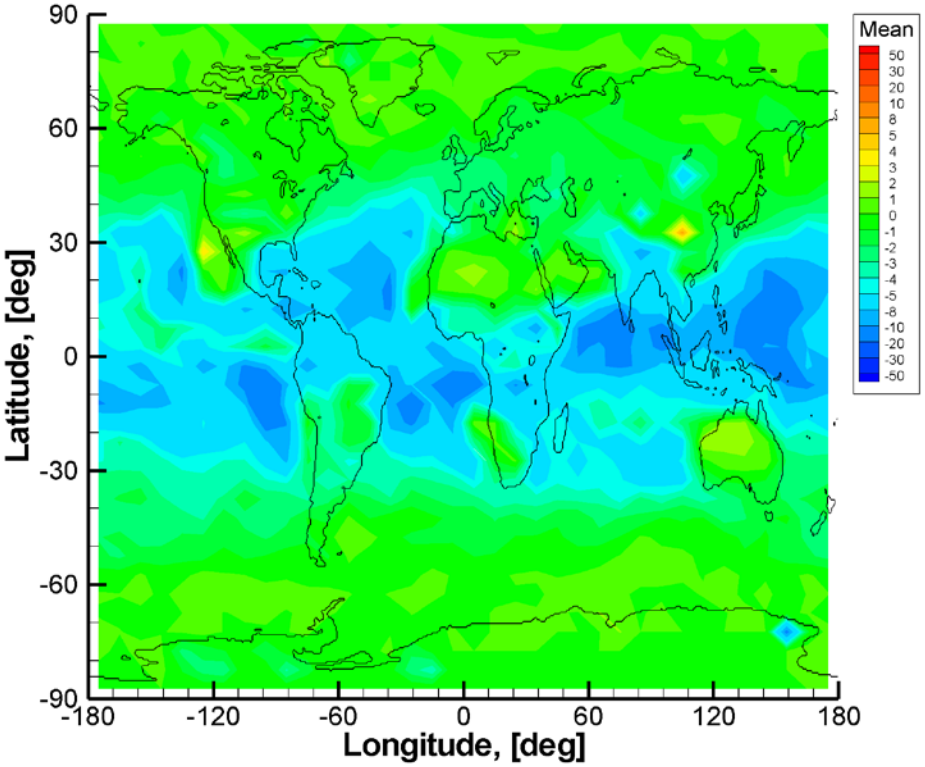

Fig. 32. Statistical comparison of COSMIC–ECMWF bending angles (O-B/B, %) at an impact height of 2.9 km.

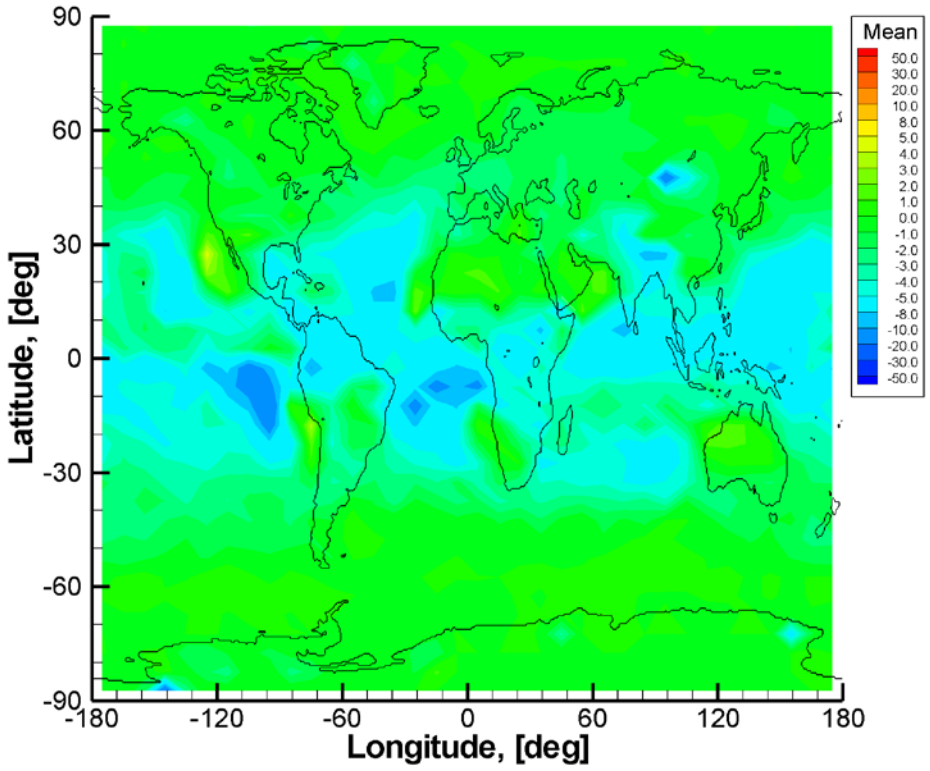

Fig. 33. Statistical comparison of COSMIC–ECMWF bending angles (O-B/B, %) at an impact height of 3.0 km.

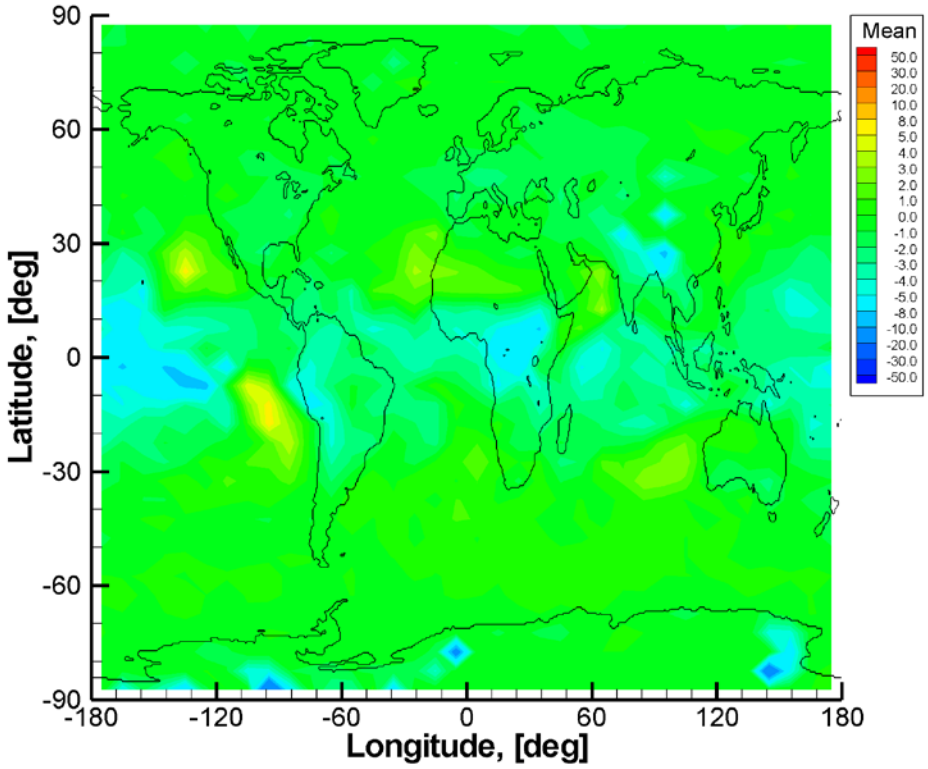

Fig. 34. Statistical comparison of COSMIC–ECMWF bending angles (O-B/B, %) at an impact height of 3.5 km.

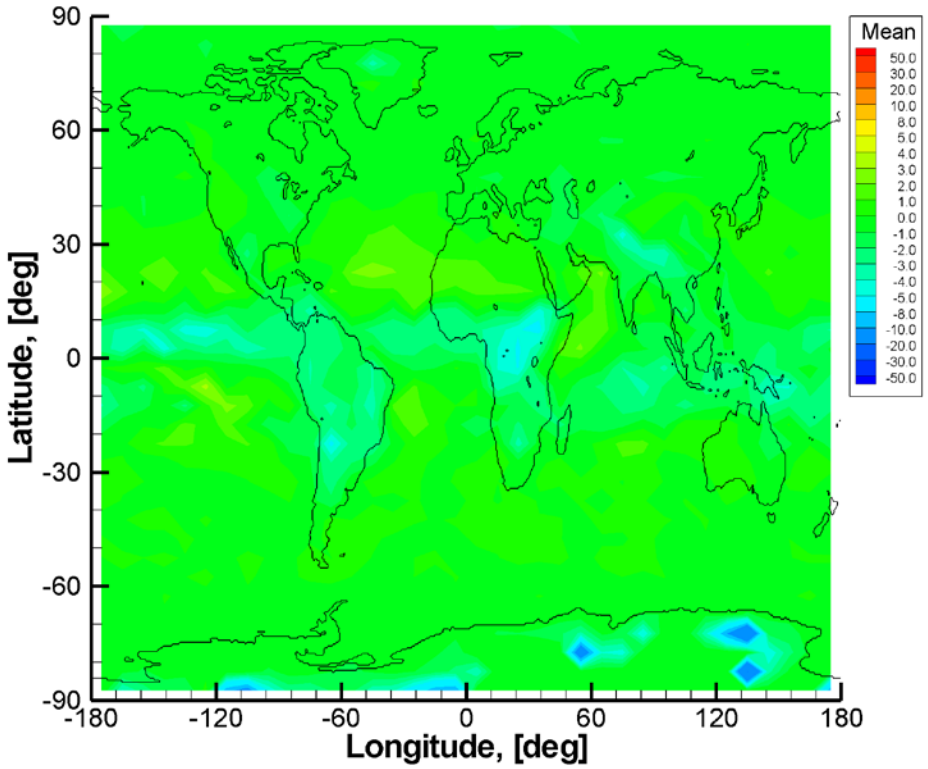

Fig. 35. Statistical comparison of COSMIC–ECMWF bending angles (O-B/B, %) at an impact height of 4.0 km.

The distribution of the bending angle bias differs from the distribution of refractivity bias. Bending angles do indicate negative bias in the aforementioned areas of strong super-refraction in the marine boundary layer. However, negative bias of bending angles is also observed in many other areas, mostly correlated with oceans in tropics.
Fig. 36 through Fig. 54 present scatter plot of ECMWF and COSMIC bending angles for the impact height below 10 km.

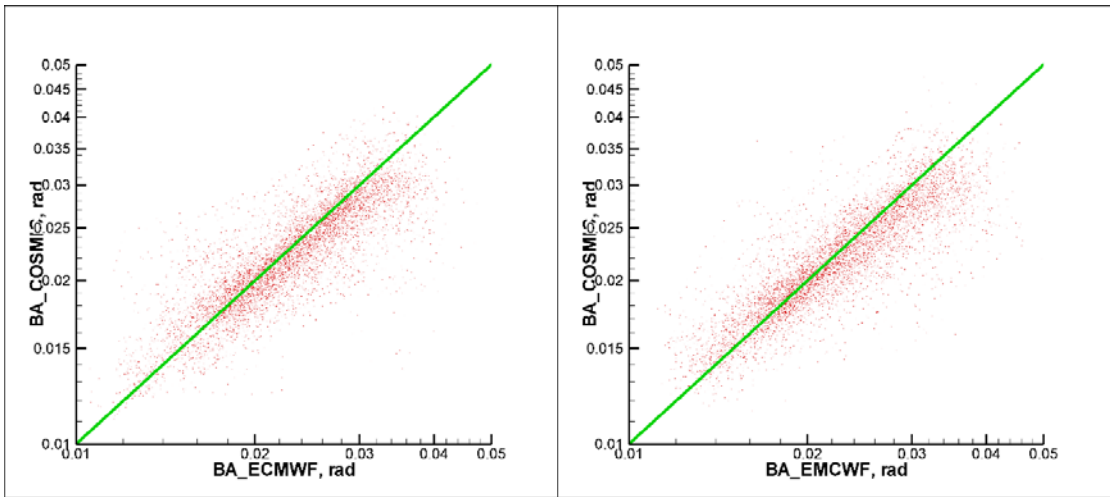

Fig. 36. Scatter plot for ECMWF and COSMIC bending angles for all latitude bins centered at 2.5°N (left) and 2.5°S (right).

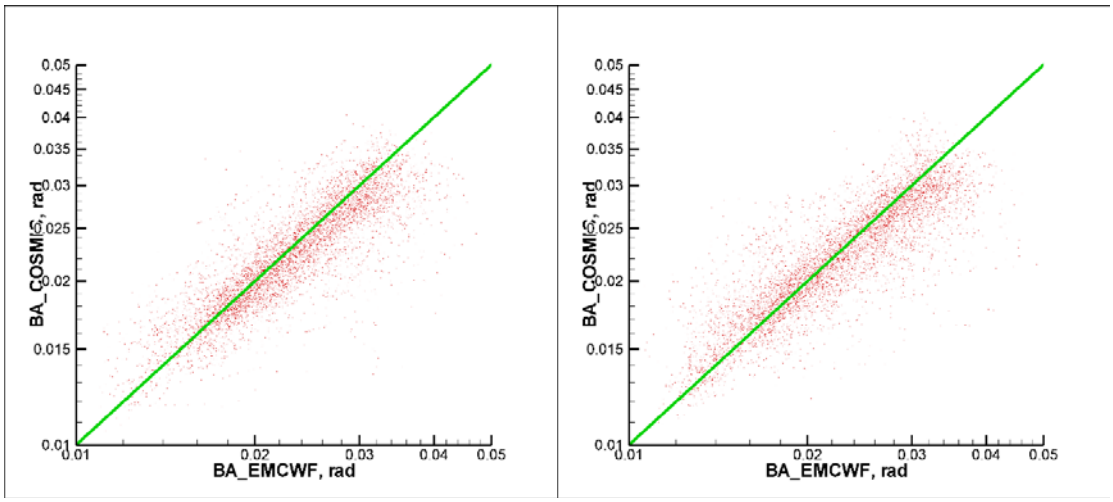

Fig. 37. Scatter plot for ECMWF and COSMIC bending angles for all latitude bins centered at 7.5°N (left) and 7.5°S (right).

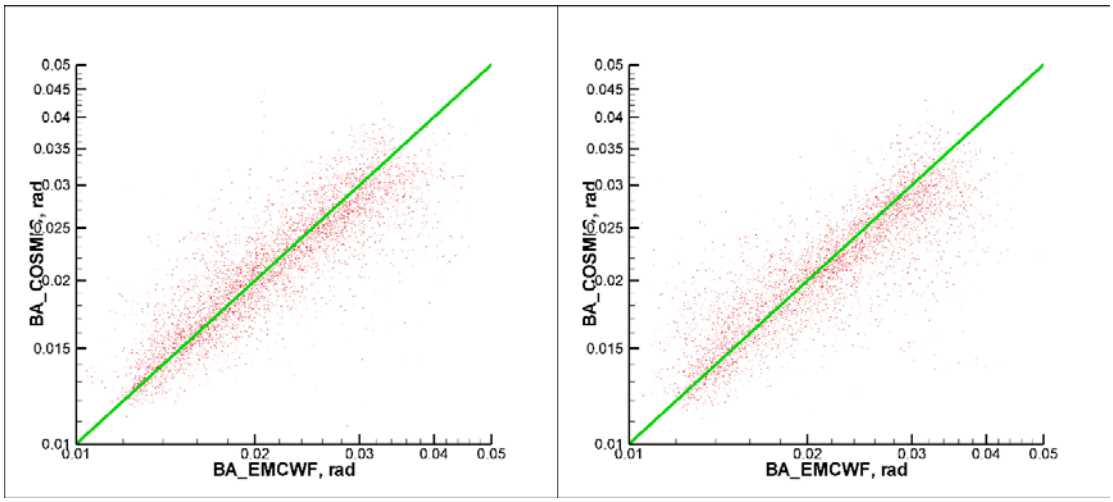

Fig. 38. Scatter plot for ECMWF and COSMIC bending angles for all latitude bins centered at 12.5°N (left) and 12.5°S (right).

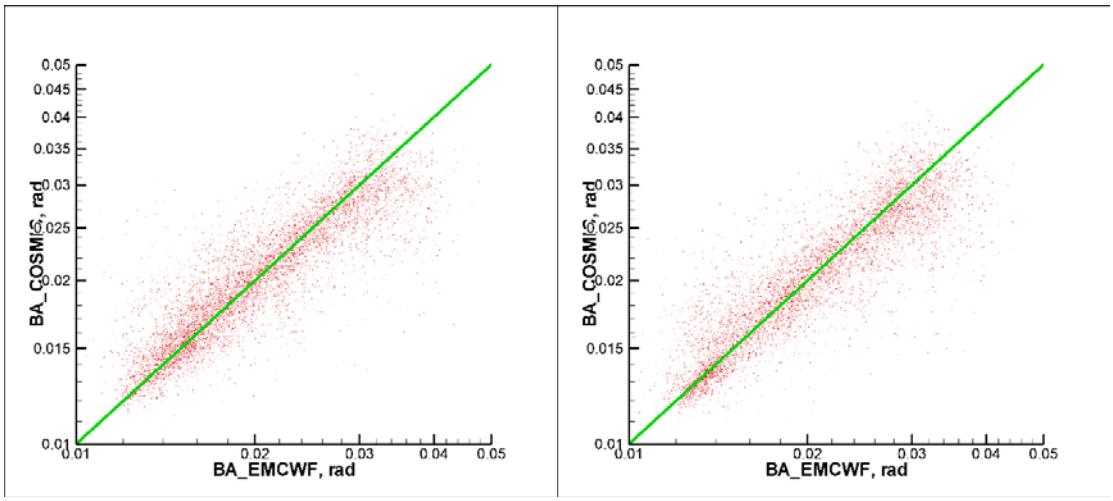

Fig. 39. Scatter plot for ECMWF and COSMIC bending angles for all latitude bins centered at 17.5°N (left) and 17.5°S (right).

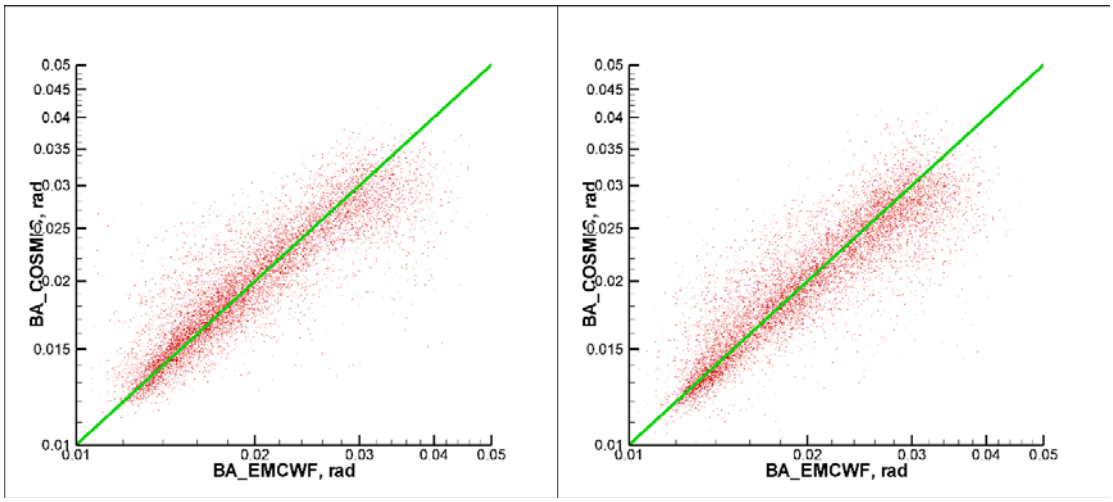

Fig. 40. Scatter plot for ECMWF and COSMIC bending angles for all latitude bins centered at 22.5°N (left) and 22.5°S (right).

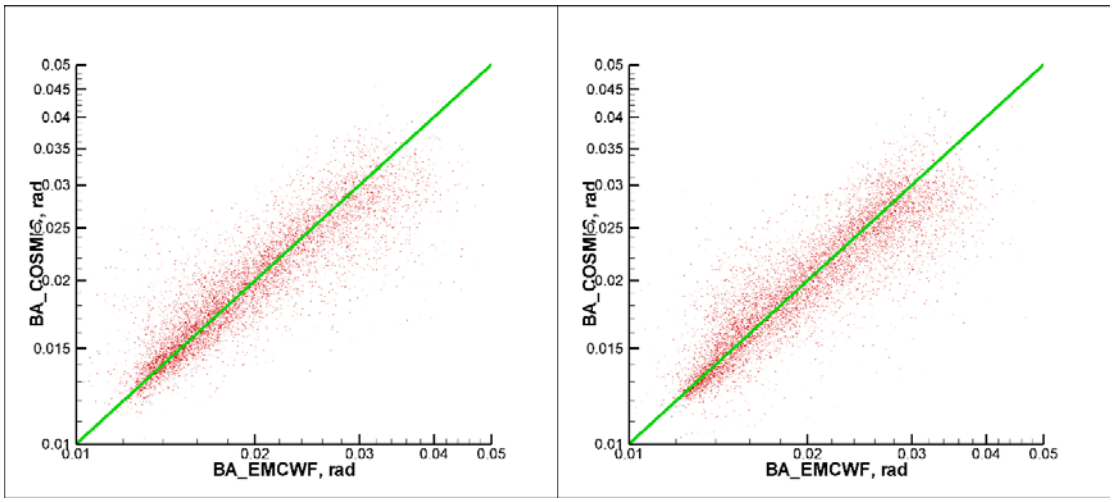

Fig. 41. Scatter plot for ECMWF and COSMIC bending angles for all latitude bins centered at 27.5°N (left) and 27.5°S (right).

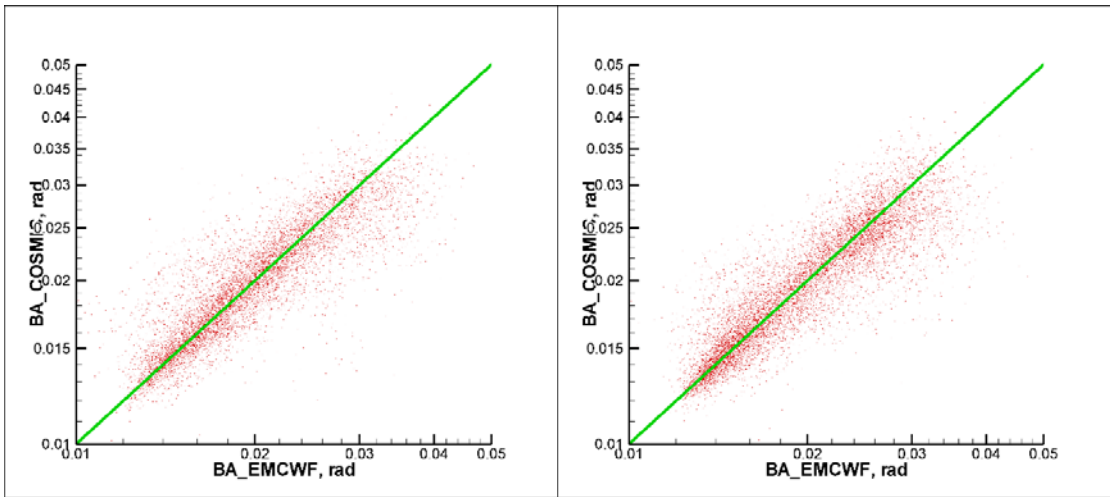

Fig. 42. Scatter plot for ECMWF and COSMIC bending angles for all latitude bins centered at 32.5°N (left) and 32.5°S (right).

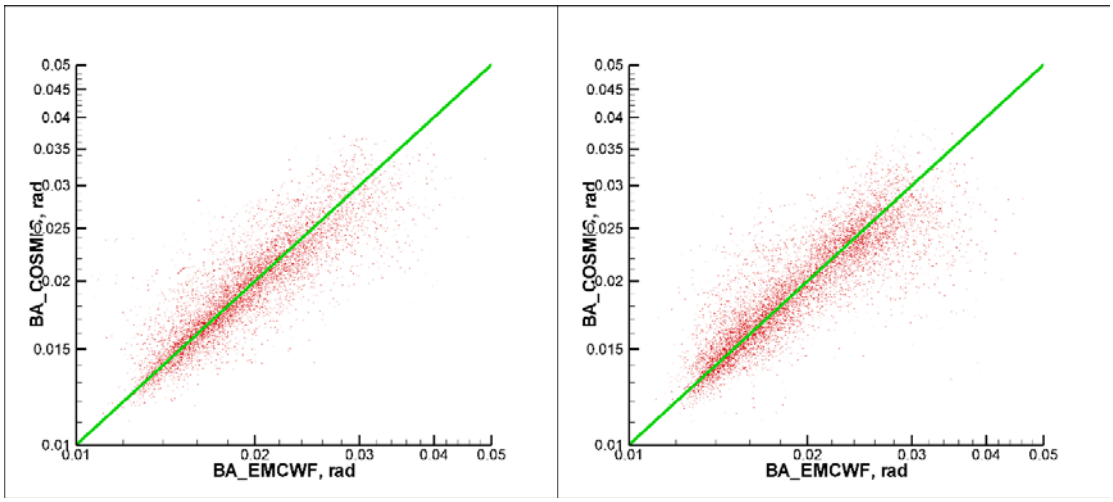

Fig. 43. Scatter plot for ECMWF and COSMIC bending angles for all latitude bins centered at 37.5°N (left) and 37.5°S (right).

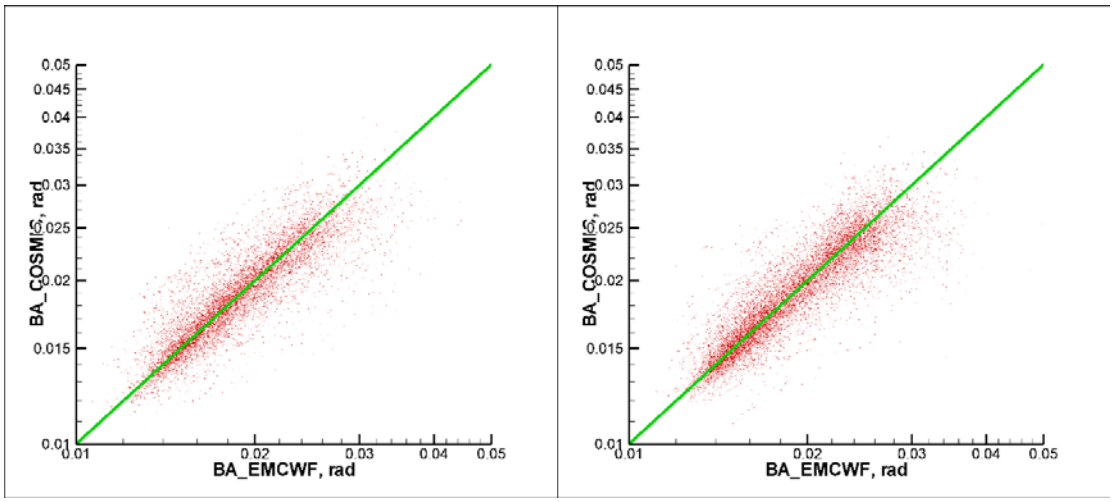

Fig. 44. Scatter plot for ECMWF and COSMIC bending angles for all latitude bins centered at 42.5°N (left) and 42.5°S (right).

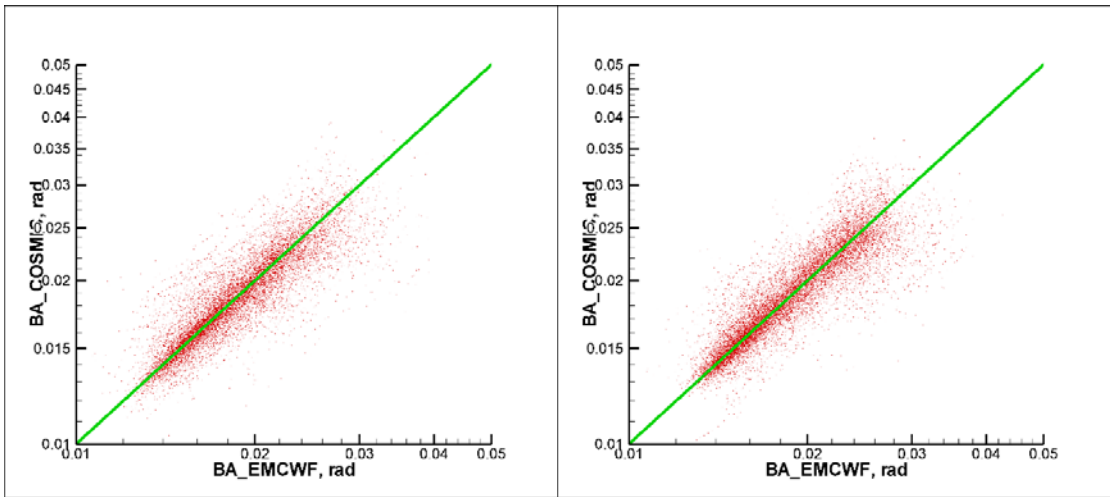

Fig. 45. Scatter plot for ECMWF and COSMIC bending angles for all latitude bins centered at 47.5°N (left) and 47.5°S (right).

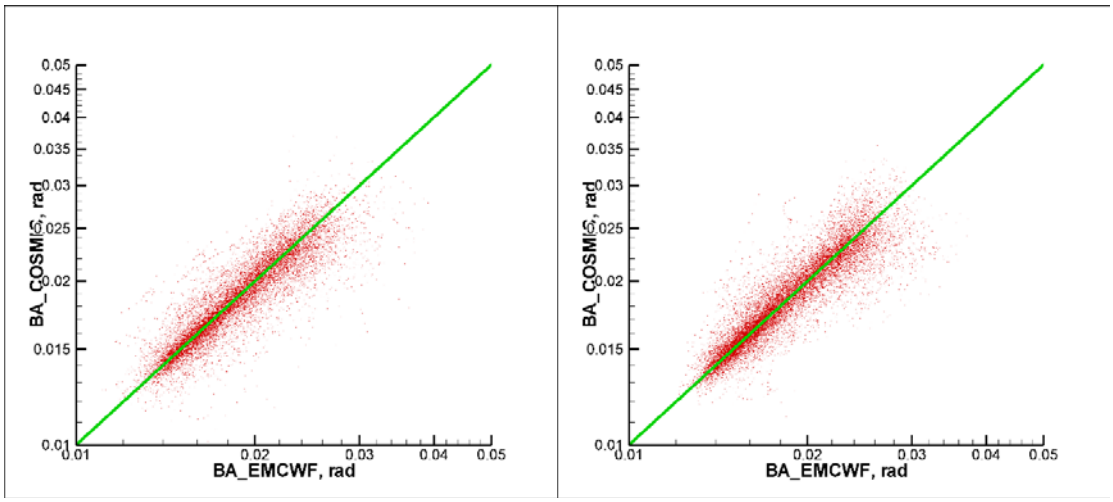

Fig. 46. Scatter plot for ECMWF and COSMIC bending angles for all latitude bins centered at 52.5°N (left) and 52.5°S (right).

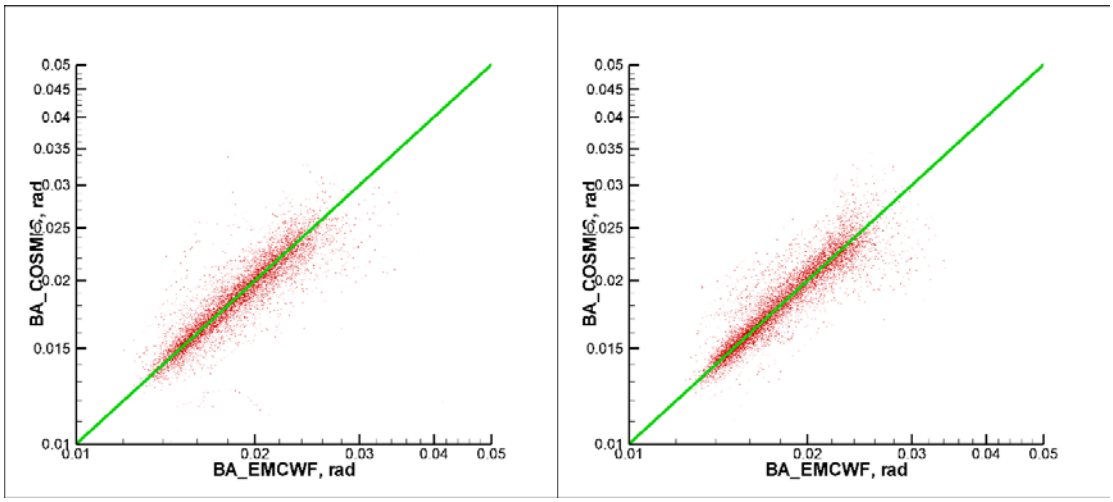

Fig. 47. Scatter plot for ECMWF and COSMIC bending angles for all latitude bins centered at 57.5°N (left) and 57.5°S (right).

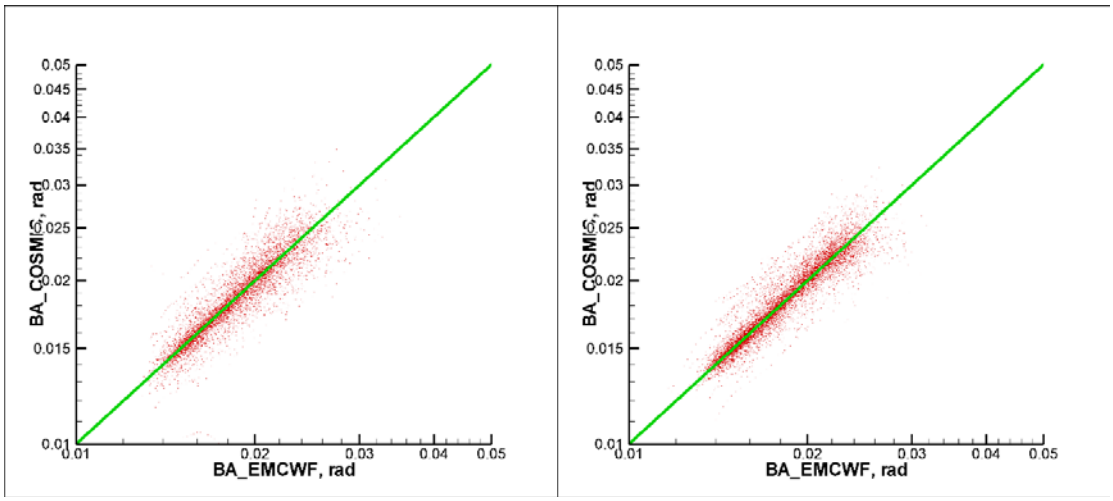

Fig. 48. Scatter plot for ECMWF and COSMIC bending angles for all latitude bins centered at 62.5°N (left) and 62.5°S (right).

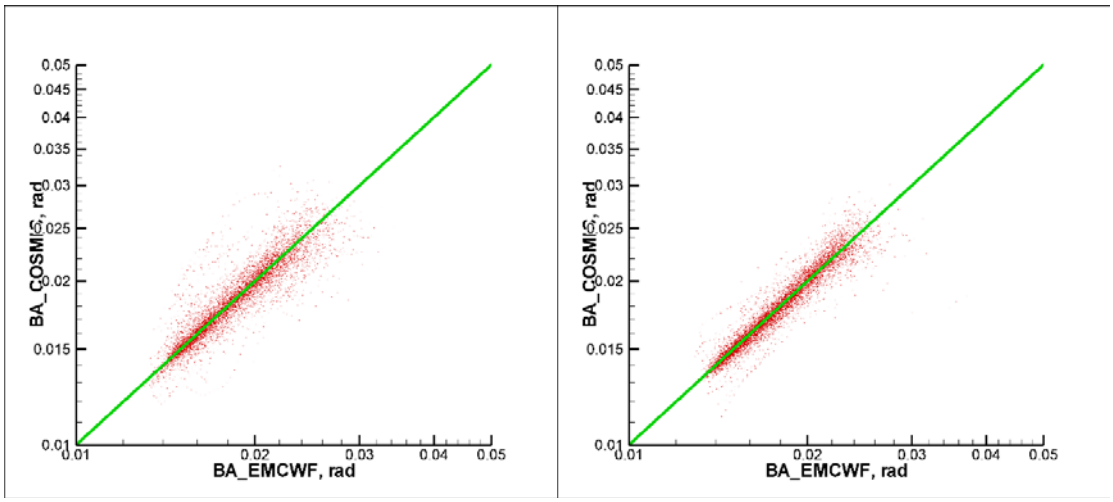

Fig. 49. Scatter plot for ECMWF and COSMIC bending angles for all latitude bins centered at 67.5°N (left) and 67.5°S (right).

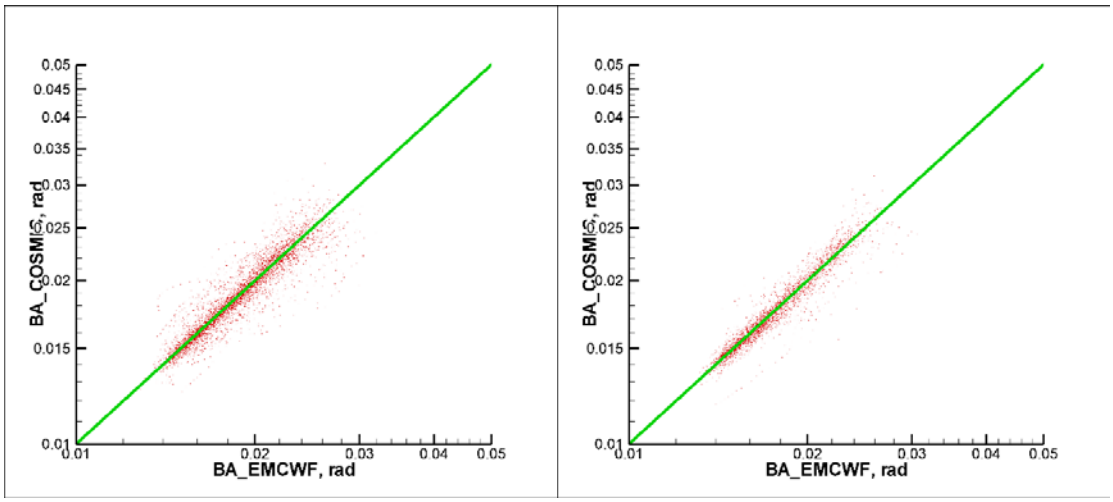

Fig. 50. Scatter plot for ECMWF and COSMIC bending angles for all latitude bins centered at 72.5°N (left) and 72.5°S (right).

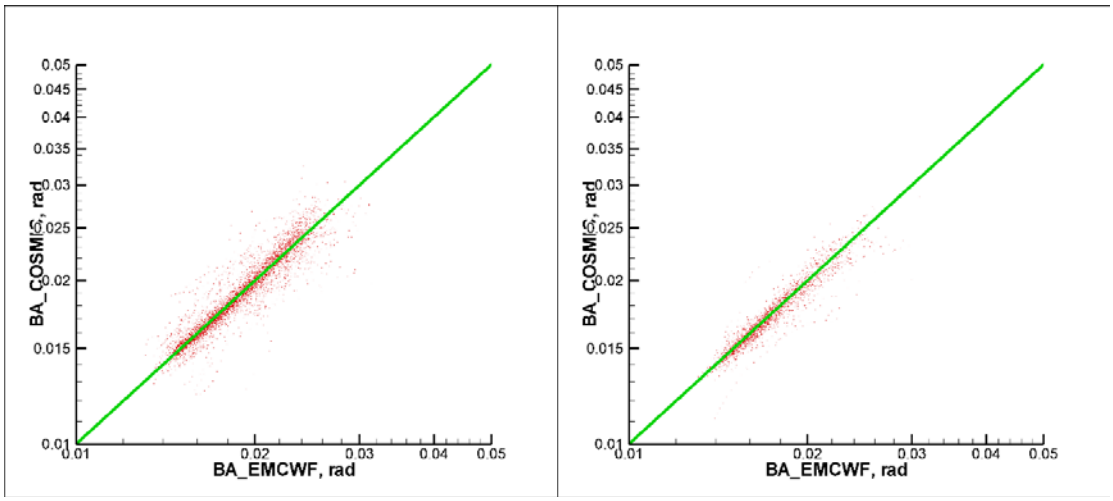

Fig. 51. Scatter plot for ECMWF and COSMIC bending angles for all latitude bins centered at 77.5°N (left) and 77.5°S (right).

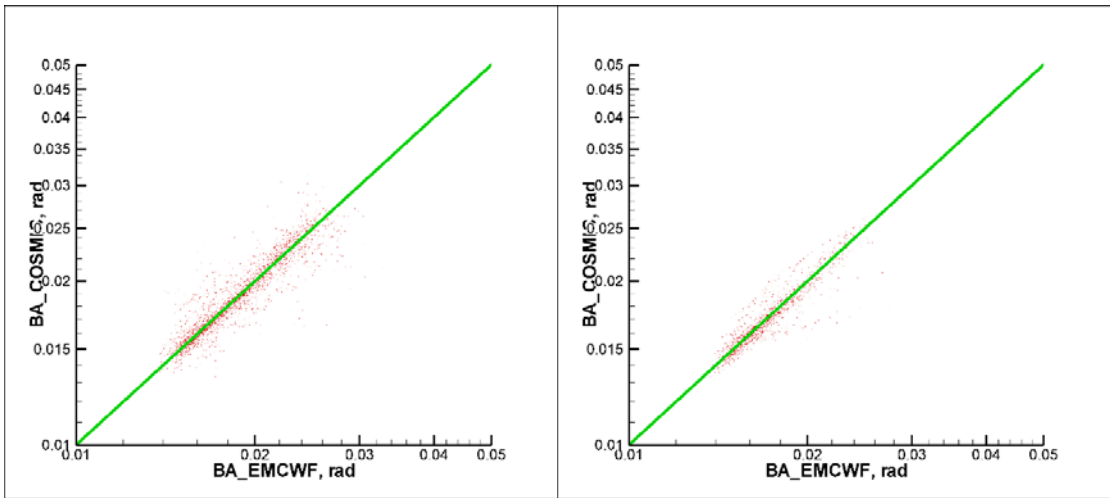

Fig. 52. Scatter plot for ECMWF and COSMIC bending angles for all latitude bins centered at 82.5°N (left) and 82.5°S (right).

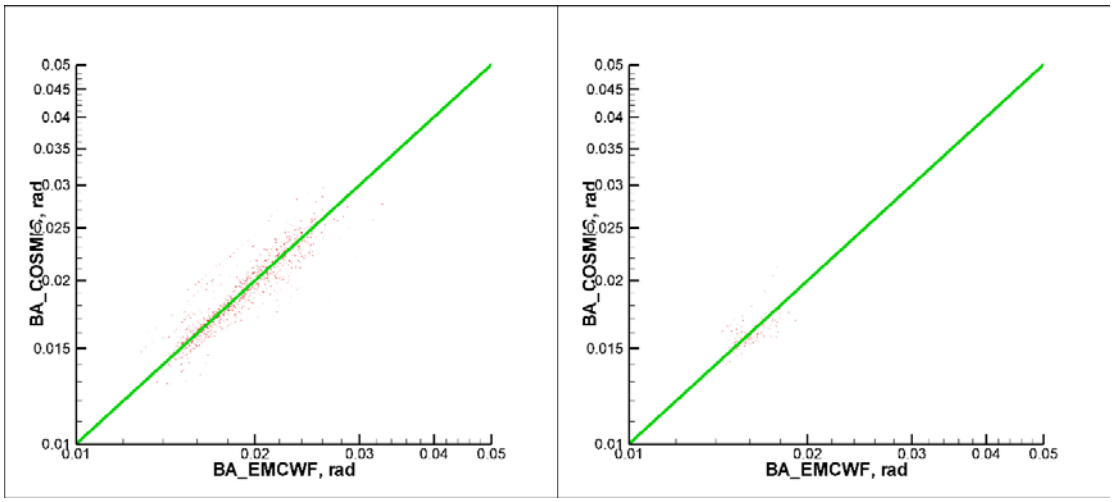

Fig. 53. Scatter plot for ECMWF and COSMIC bending angles for all latitude bins centered at 87.5°N (left) and 87.5°S (right).

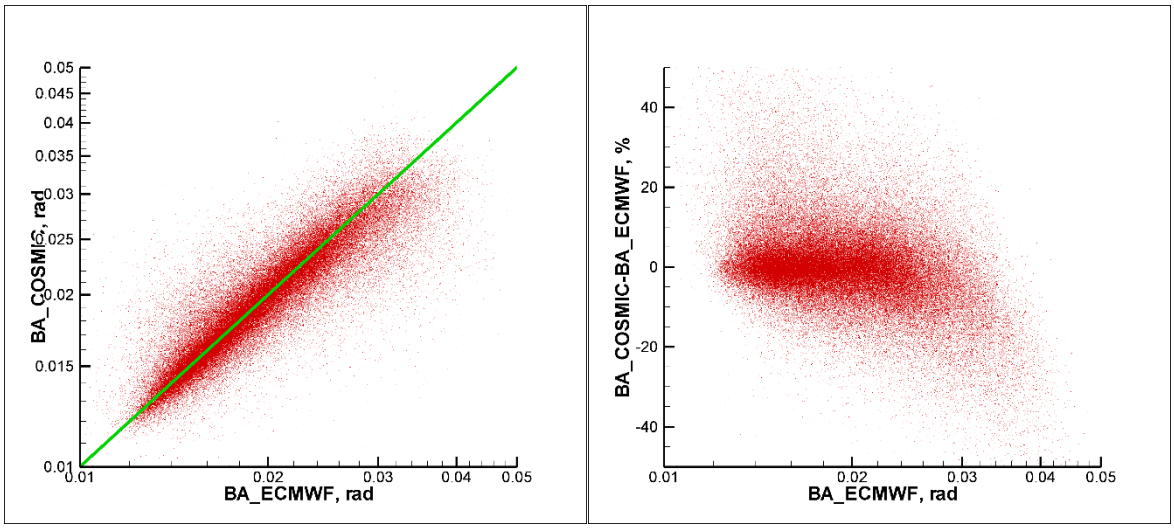

Fig. 54. Scatter plot for all latitudes. Left: ECMWF and COSMIC bending angles. Right: ECMWF bending angles and relative difference COSMIC–ECMWF (O-B/B, %).

An important observation is that the systematic difference correlates with the bending angle value. Bending angles below 0.025 radians are unbiased, for larger bending angles the bias increases. This dependence is universal for all the latitudes, which allows for plotting all the points in a single plot for the whole globe (Fig. 54).

2.2 Seasonal dependencies

Fig. 55 through Fig. 80 show the seasonal dependencies of the refractivity bias.

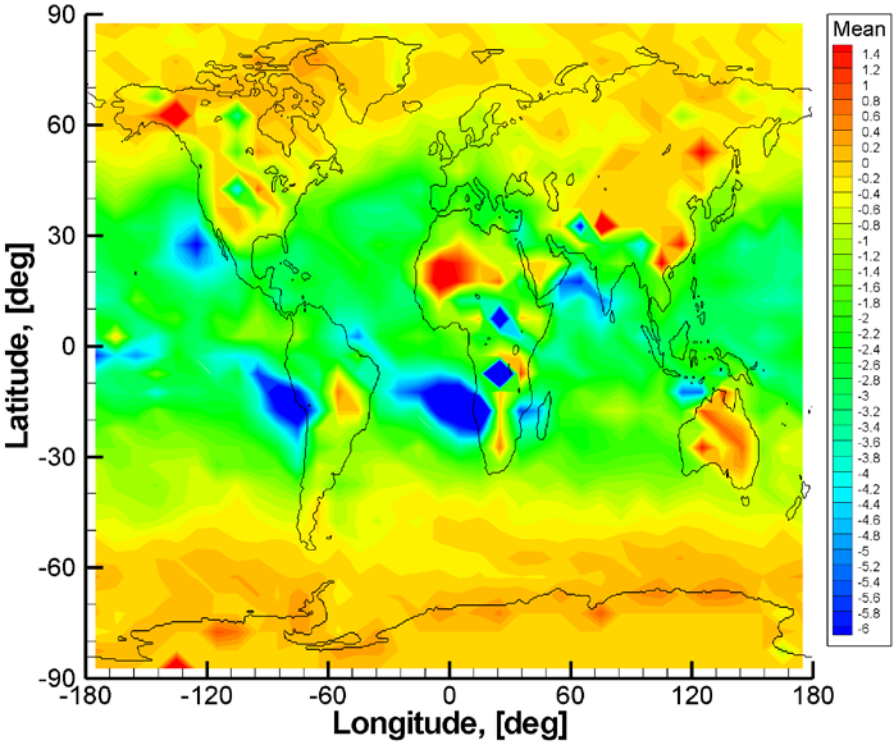

Fig. 55. Statistical comparison of COSMIC–ECMWF refractivities (O-B/B, %) at an altitude of 0.4 km for autumn.

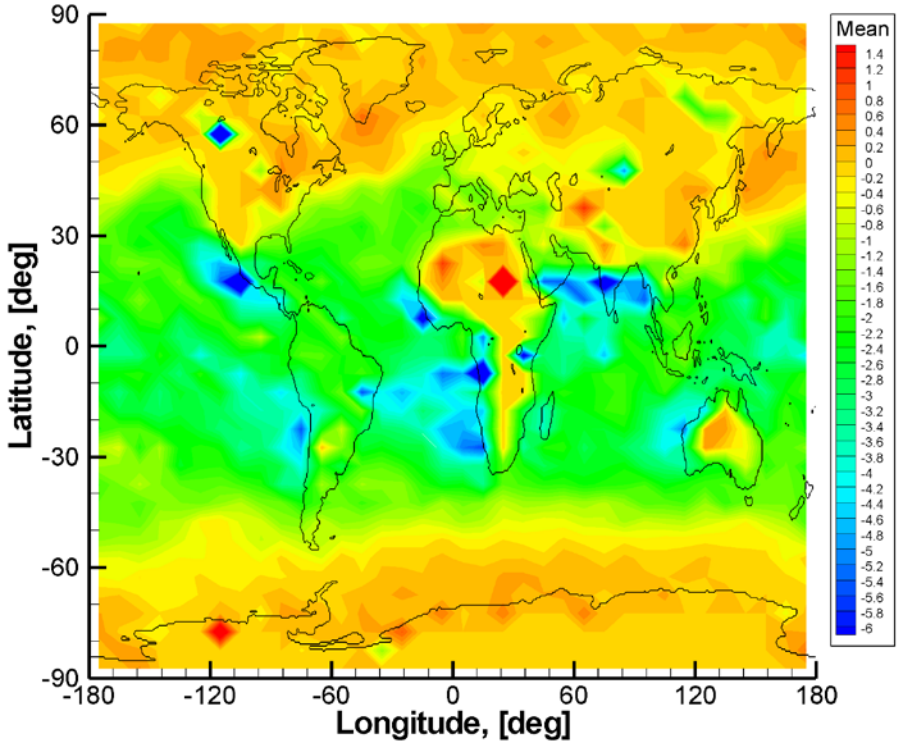

Fig. 56. Statistical comparison of COSMIC–ECMWF refractivities (O-B/B, %) at an altitude of 0.4 km for winter.

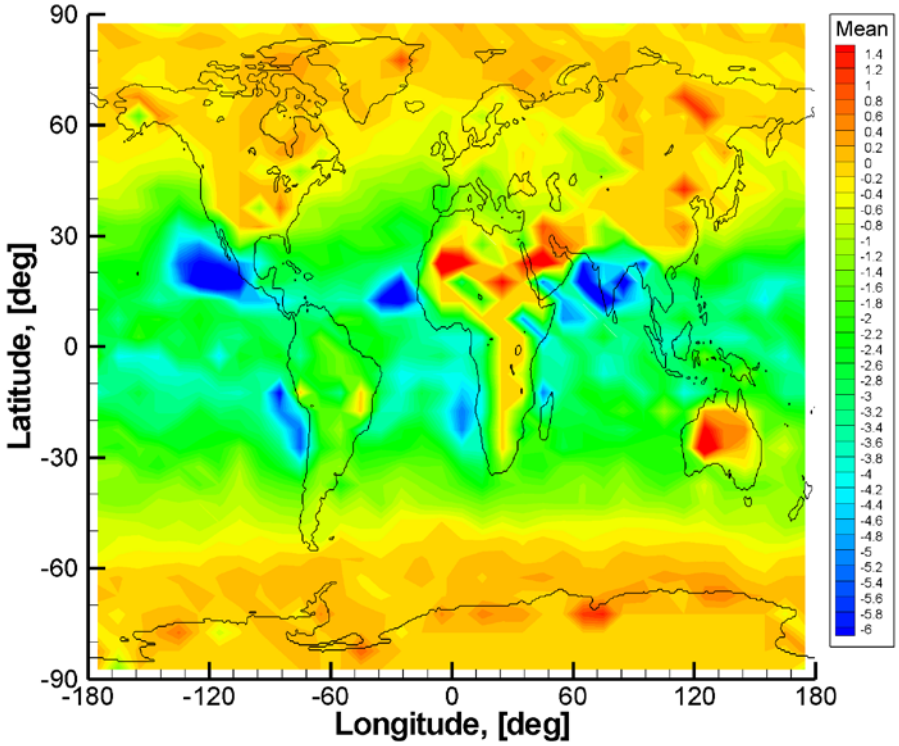

Fig. 57. Statistical comparison of COSMIC–ECMWF refractivities (O-B/B, %) at an altitude of 0.4 km for spring.

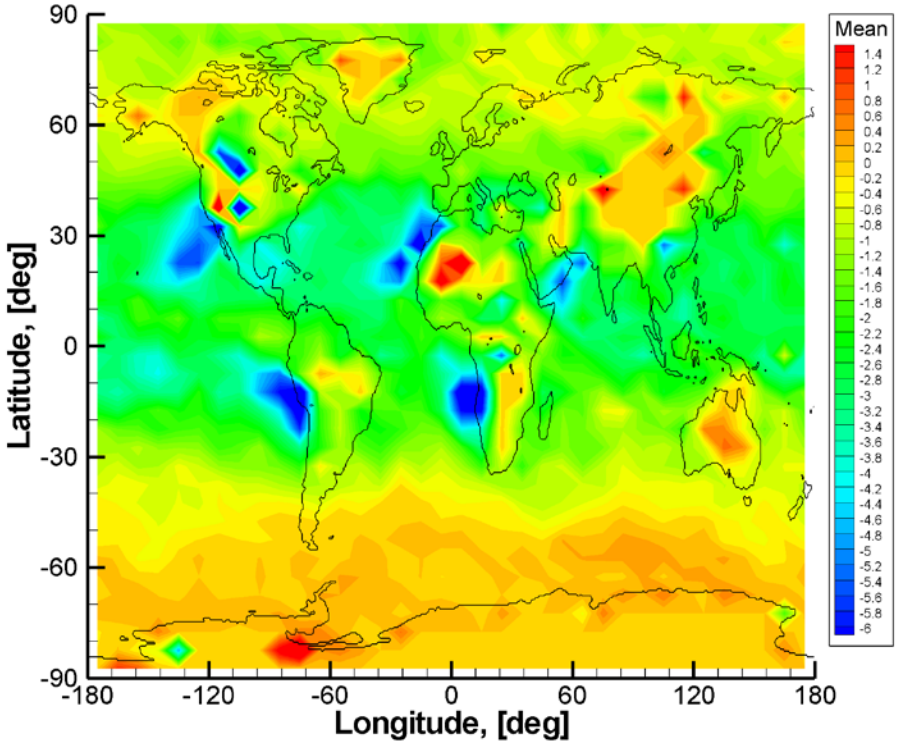

Fig. 58. Statistical comparison of COSMIC–ECMWF refractivities (O-B/B, %) at an altitude of 0.4 km for summer.

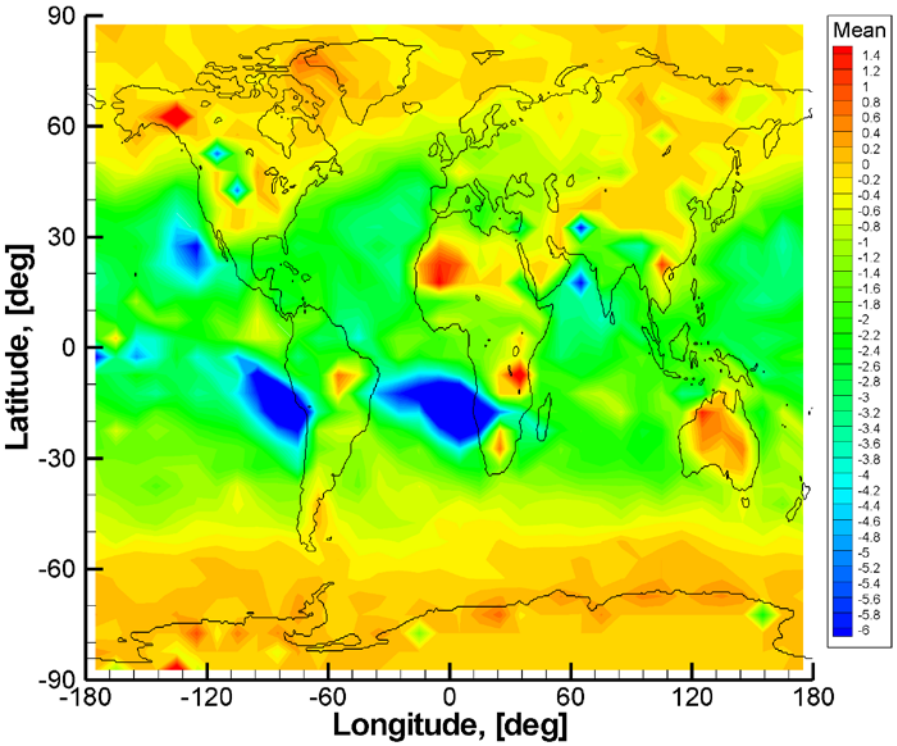

Fig. 59. Statistical comparison of COSMIC–ECMWF refractivities (O-B/B, %) at an altitude of 0.6 km for autumn.

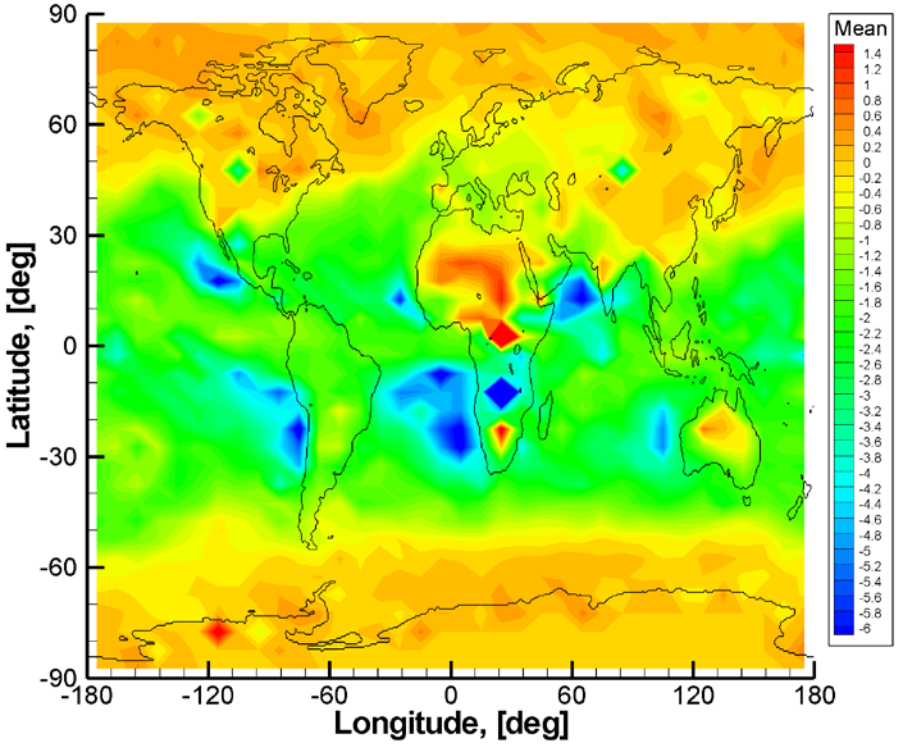

Fig. 60. Statistical comparison of COSMIC–ECMWF refractivities (O-B/B, %) at an altitude of 0.6 km for winter.

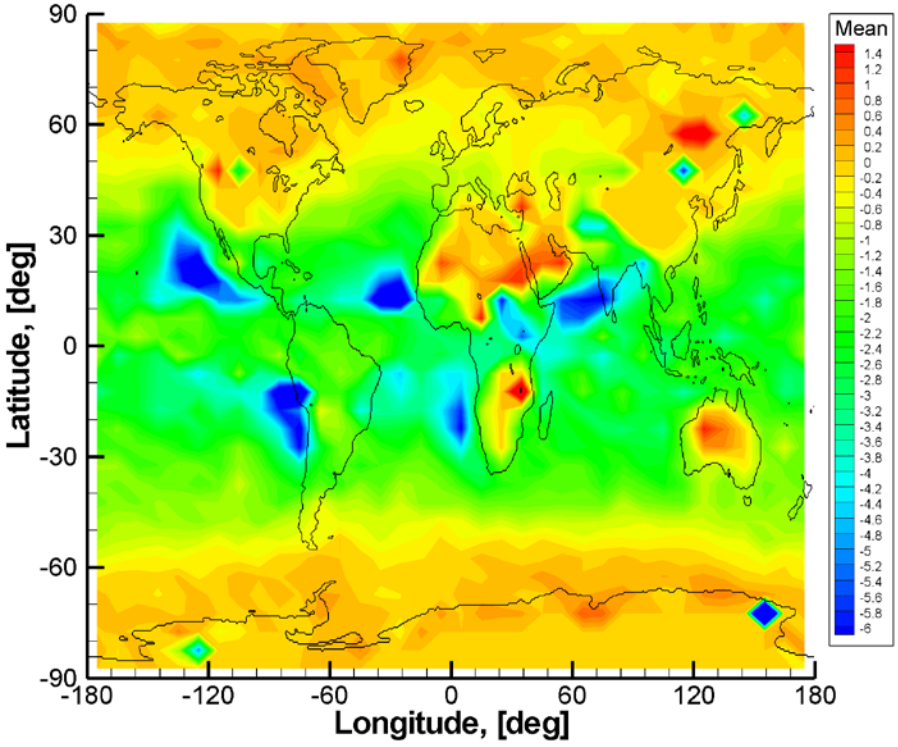

Fig. 61. Statistical comparison of COSMIC–ECMWF refractivities (O-B/B, %) at an altitude of 0.6 km for spring.

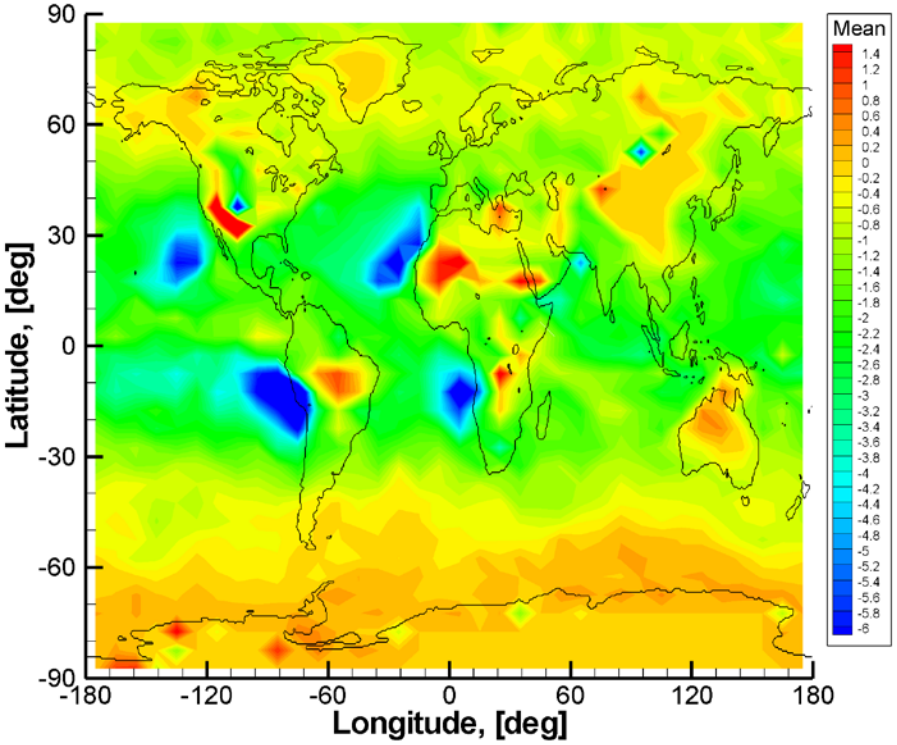

Fig. 62. Statistical comparison of COSMIC–ECMWF refractivities (O-B/B, %) at an altitude of 0.6 km for summer.

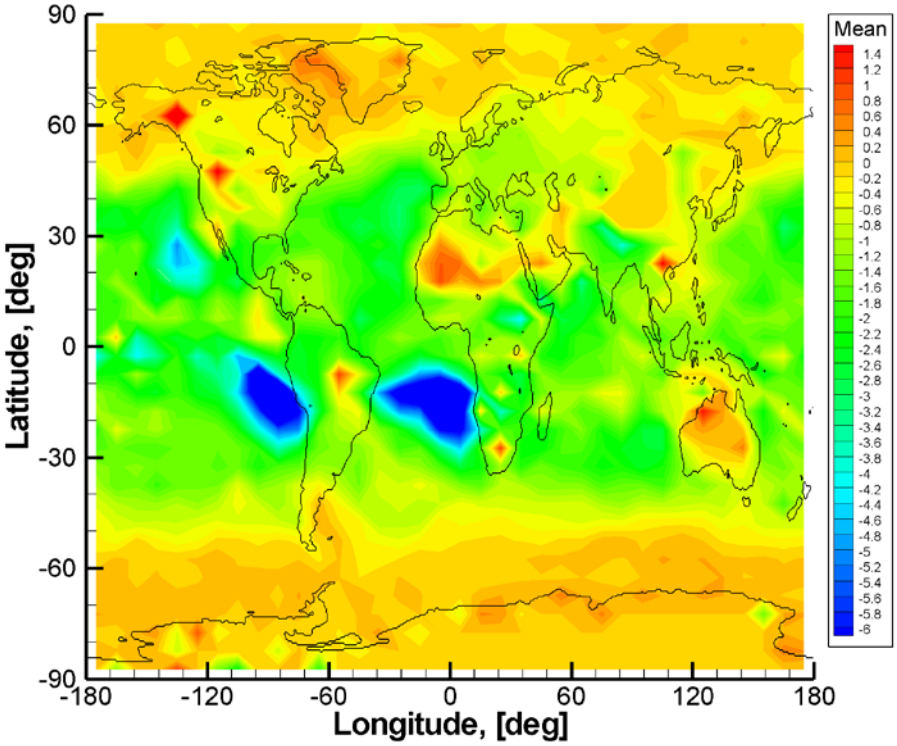

Fig. 63. Statistical comparison of COSMIC–ECMWF refractivities (O-B/B, %) at an altitude of 0.8 km for autumn.

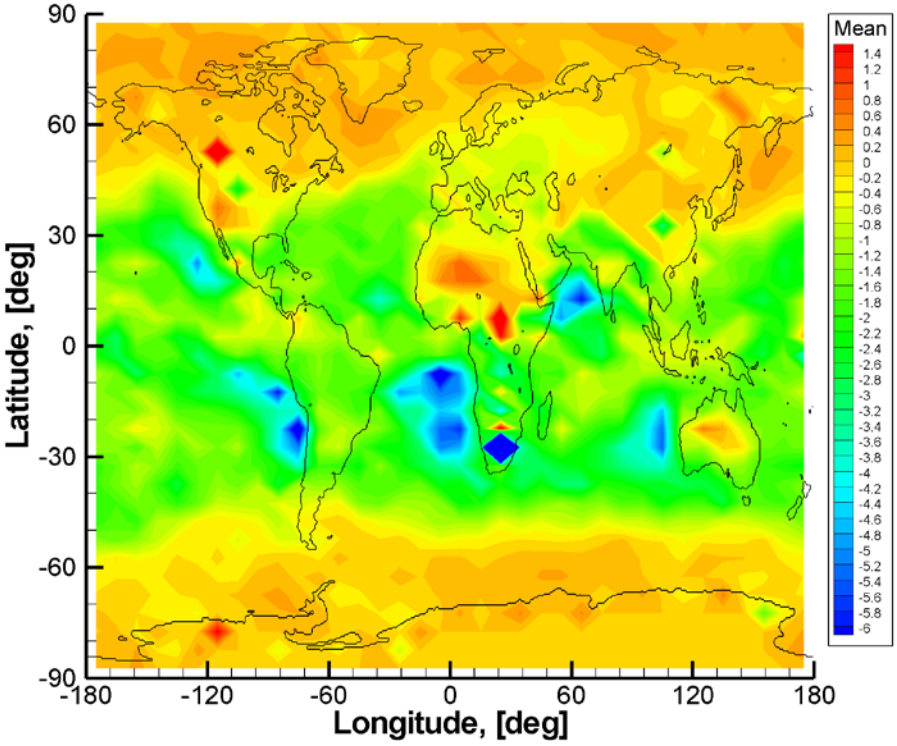

Fig. 64. Statistical comparison of COSMIC–ECMWF refractivities (O-B/B, %) at an altitude of 0.8 km for winter.

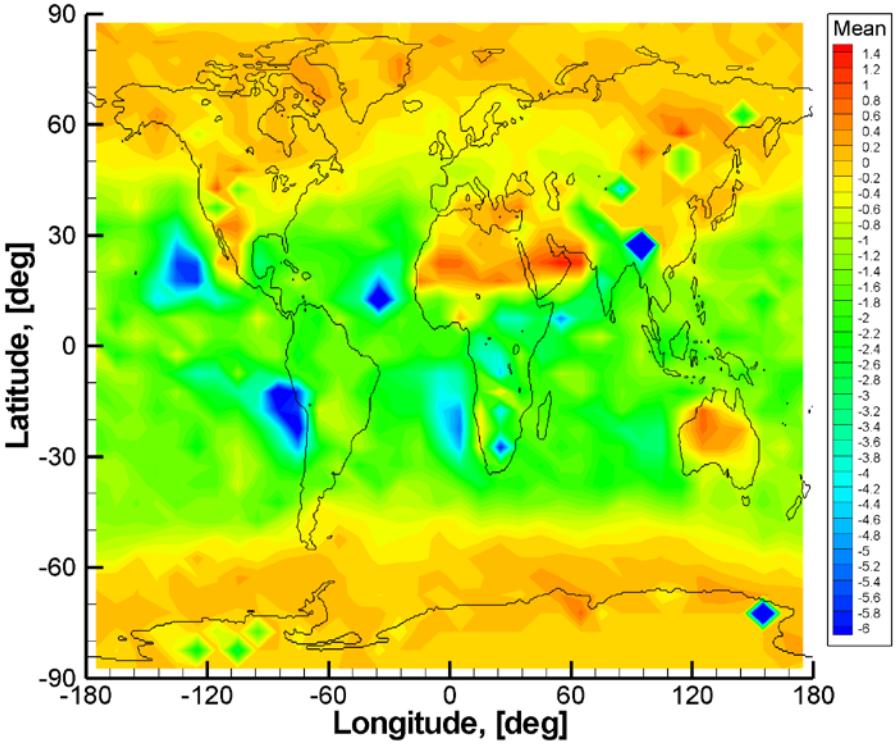

Fig. 65. Statistical comparison of COSMIC–ECMWF refractivities (O-B/B, %) at an altitude of 0.8 km for spring.

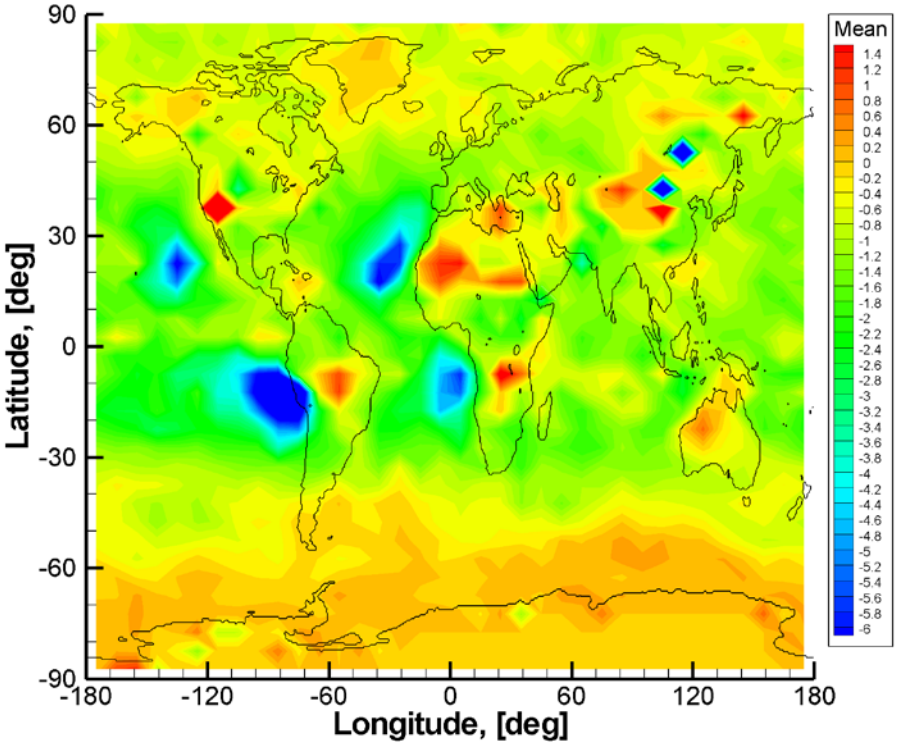

Fig. 66. Statistical comparison of COSMIC–ECMWF refractivities (O-B/B, %) at an altitude of 0.8 km for summer.

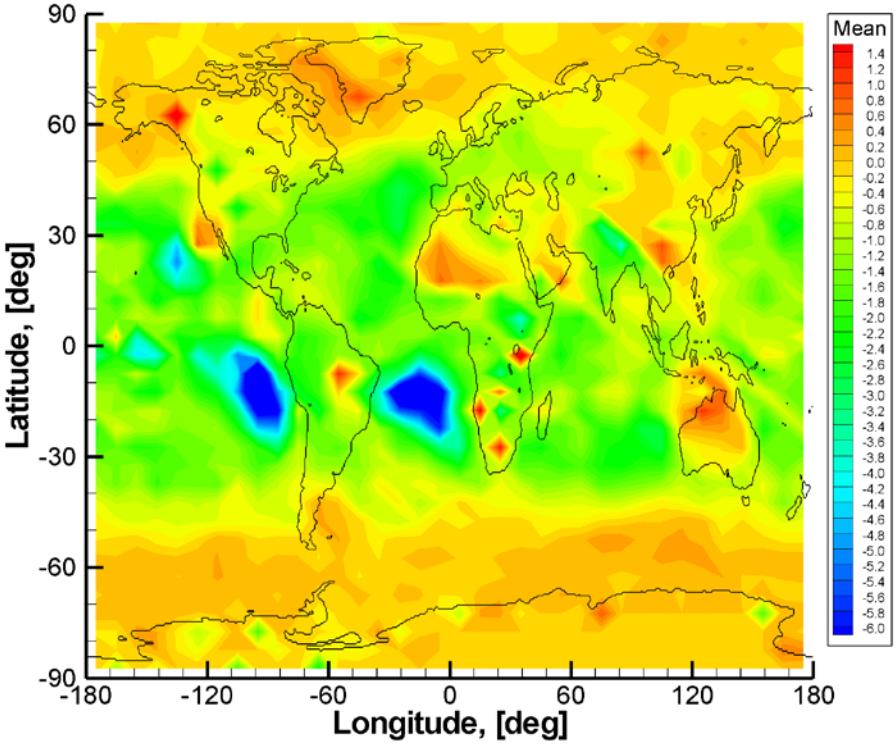

Fig. 67. Statistical comparison of COSMIC–ECMWF refractivities (O-B/B, %) at an altitude of 1.0 km for autumn.

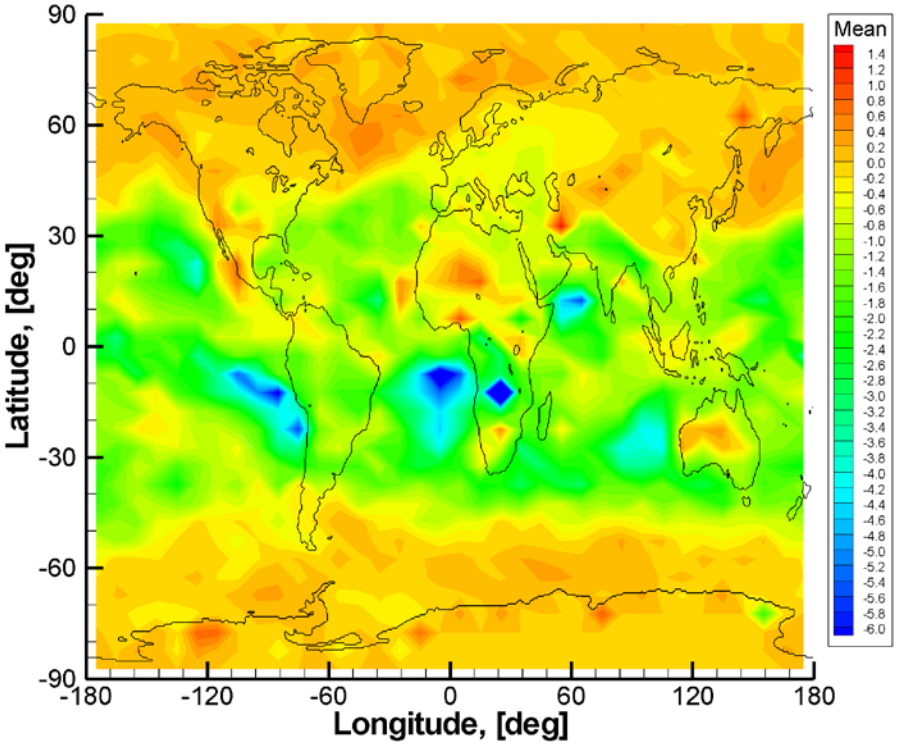

Fig. 68. Statistical comparison of COSMIC–ECMWF refractivities (O-B/B, %) at an altitude of 1.0 km for winter.

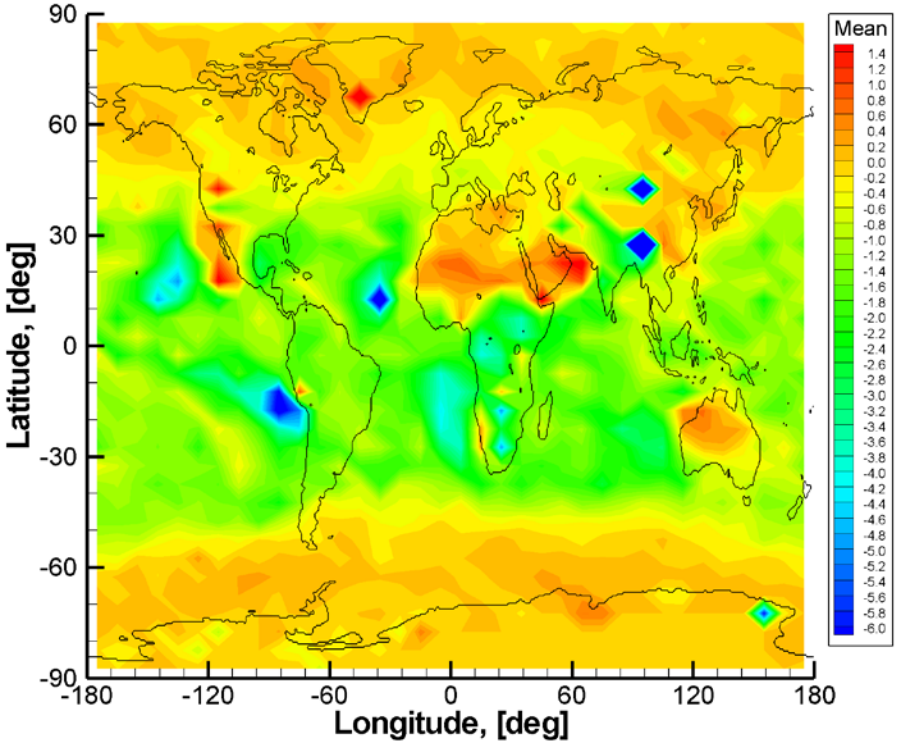

Fig. 69. Statistical comparison of COSMIC–ECMWF refractivities (O-B/B, %) at an altitude of 1.0 km for spring.

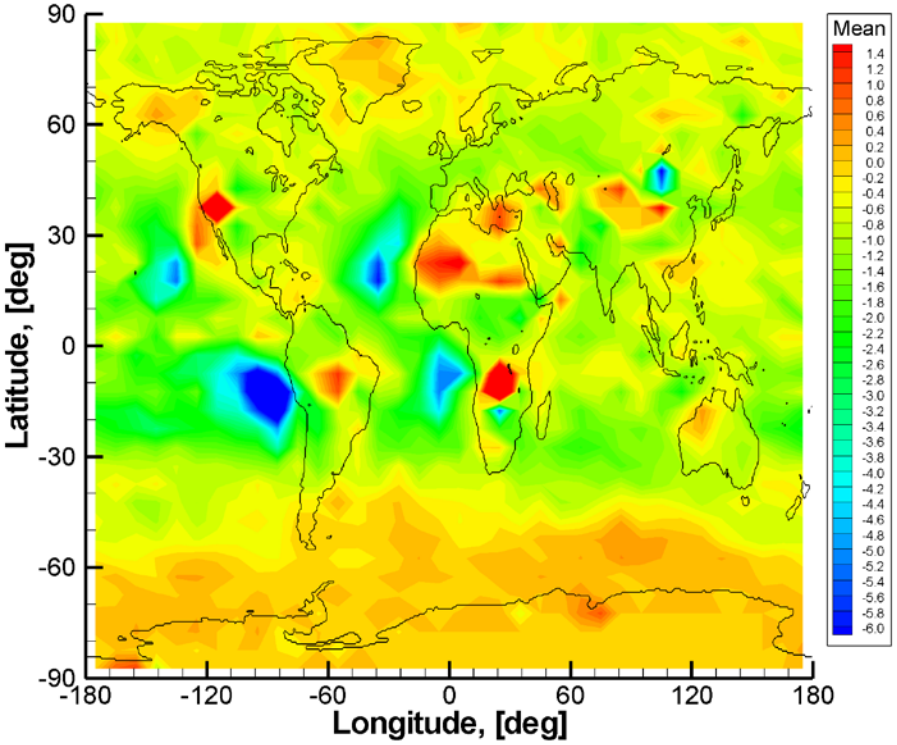

Fig. 70. Statistical comparison of COSMIC–ECMWF refractivities (O-B/B, %) at an altitude of 1.0 km for summer.

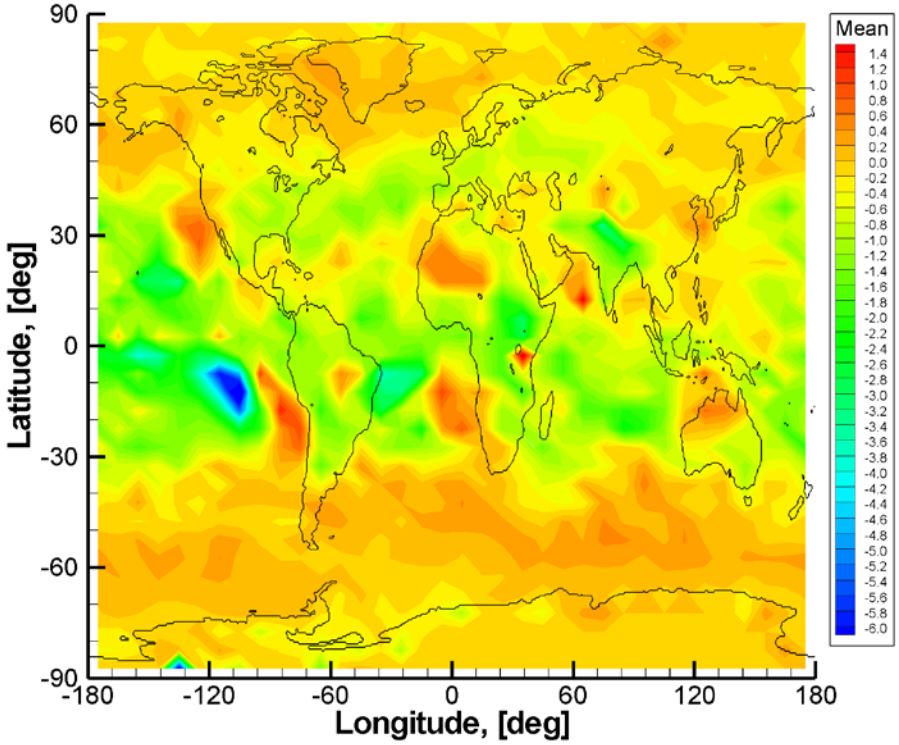

Fig. 71. Statistical comparison of COSMIC–ECMWF refractivities (O-B/B, %) at an altitude of 1.5 km for autumn.

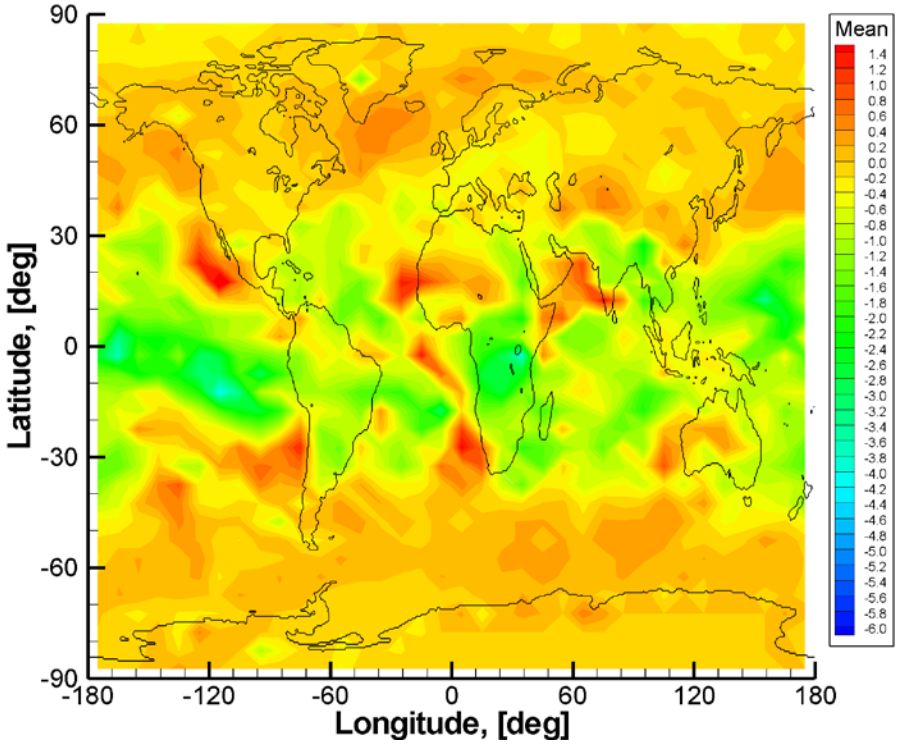

Fig. 72. Statistical comparison of COSMIC–ECMWF refractivities (O-B/B, %) at an altitude of 1.5 km for winter.

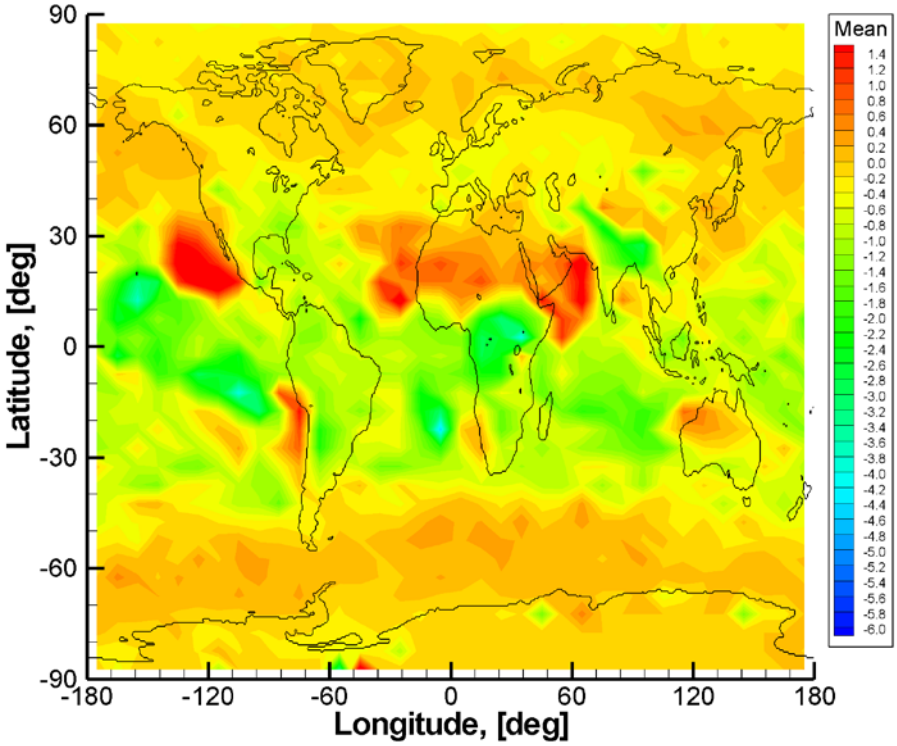

Fig. 73. Statistical comparison of COSMIC–ECMWF refractivities (O-B/B, %) at an altitude of 1.5 km for spring.

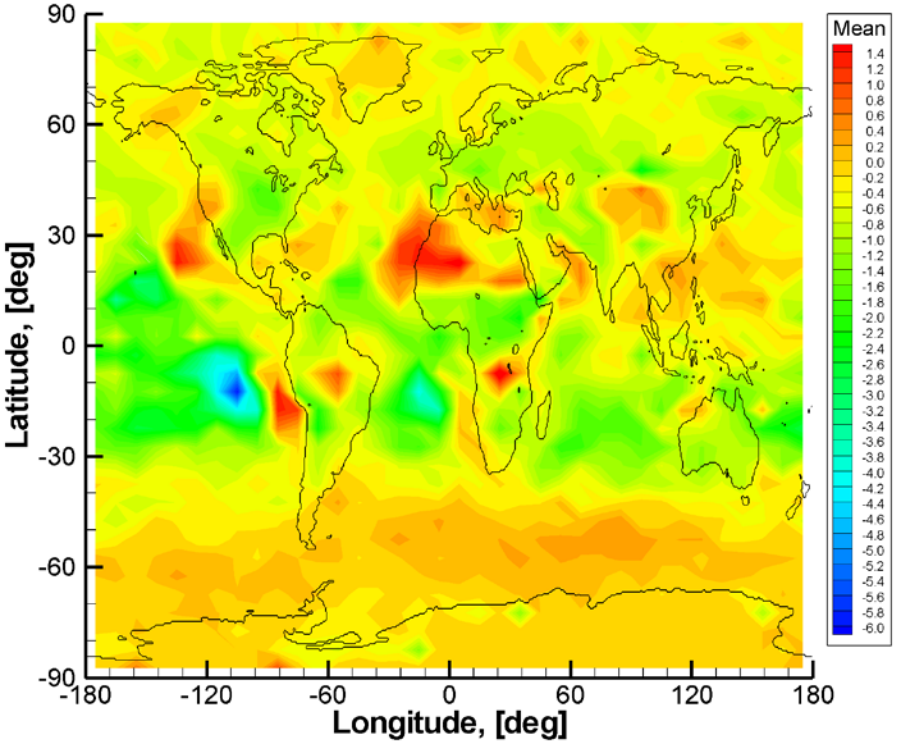

Fig. 74. Statistical comparison of COSMIC–ECMWF refractivities (O-B/B, %) at an altitude of 1.5 km for summer.

The effect of marine boundary layer is most pronounced for the autumn season. In winter the super-refraction region is broken into multiple smaller sub-regions.

3. Statistical Analysis of GRAS/METOP Data

Fig. 75 through Fig. 80 show the statistical comparisons of refractivities retrieved from GRAS/METOP-A observations for year 2009 with ECMWF analyses. The number of GRAS/METOP-A observations is significantly smaller than that of COSMIC. This makes the statistical analysis more susceptible to outliers. Still, we observe the same areas with the large negative bias of refracitivity.

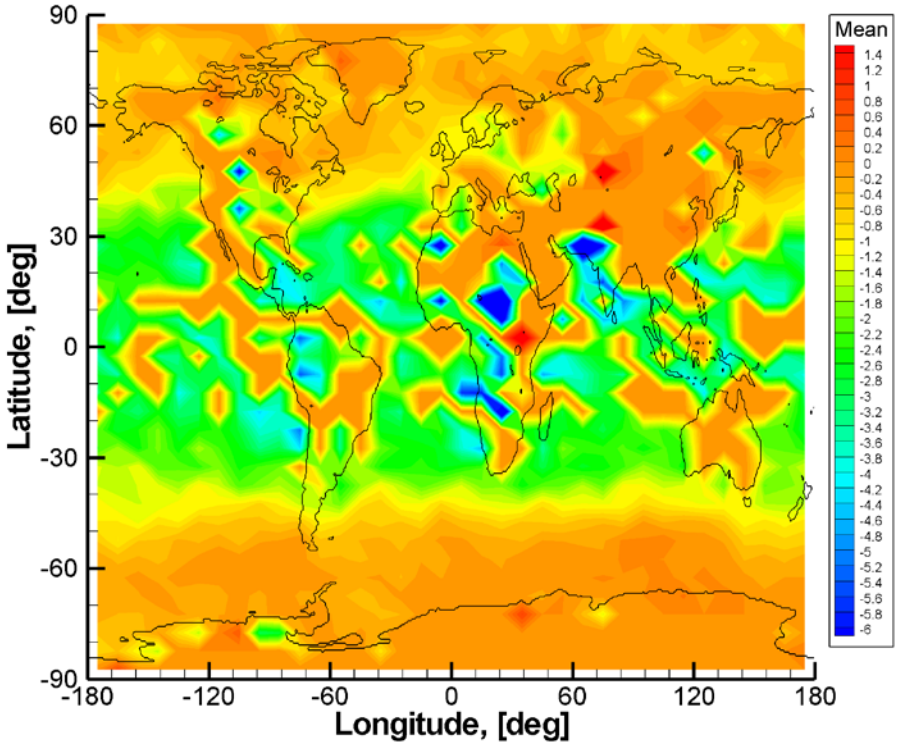

Fig. 75. Statistical comparison of GRAS–ECMWF refractivities (O-B/B, %) at an altitude of 0.2 km.

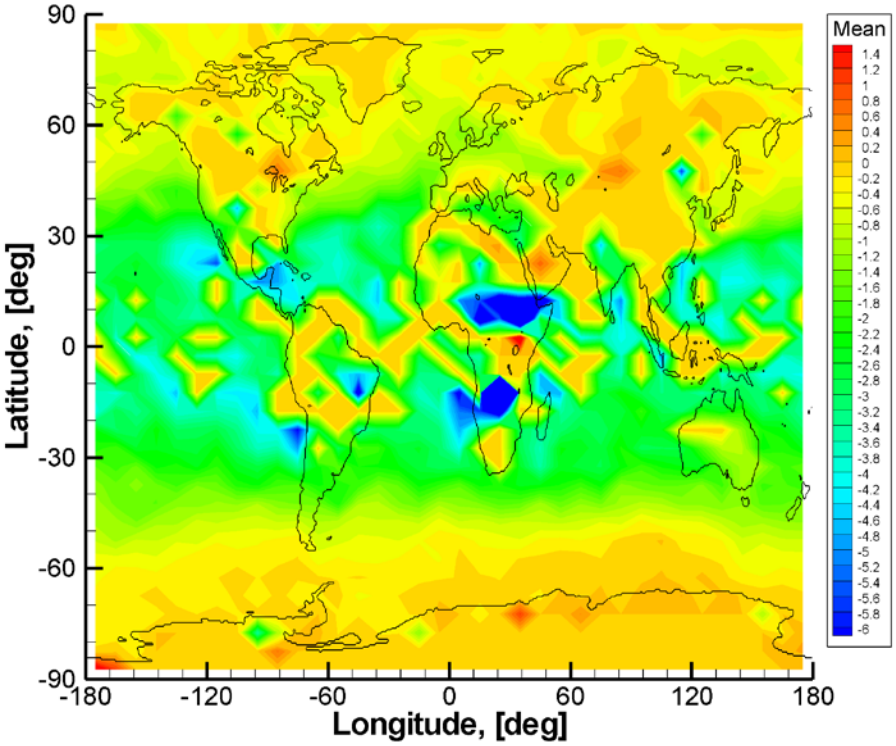

Fig. 76. Statistical comparison of GRAS –ECMWF refractivities (O-B/B, %) at an altitude of 0.3 km.

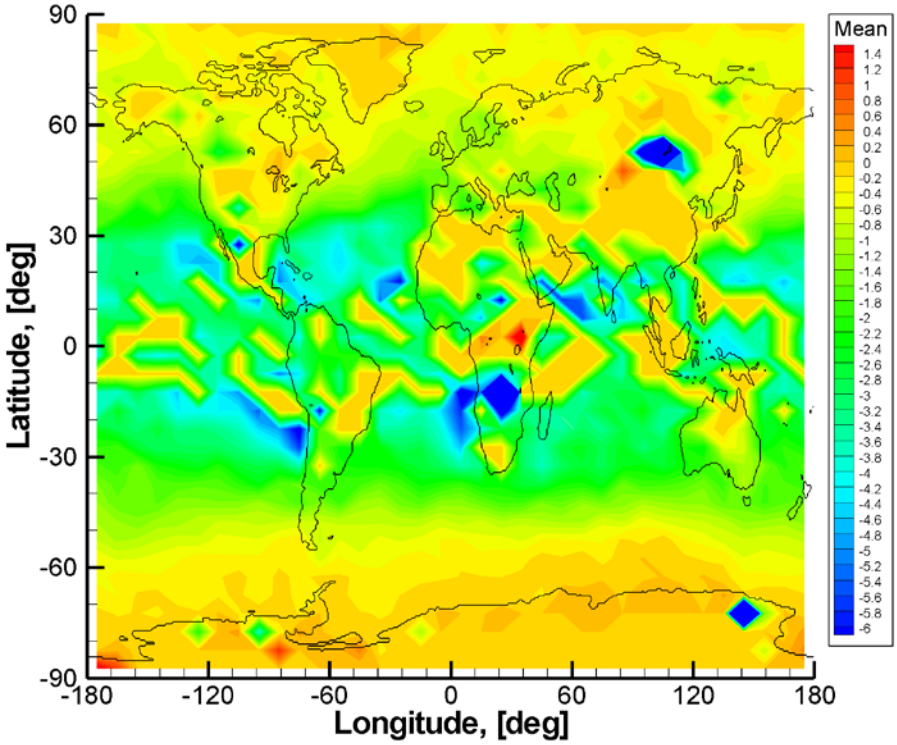

Fig. 77. Statistical comparison of GRAS –ECMWF refractivities (O-B/B, %) at an altitude of 0.4 km.

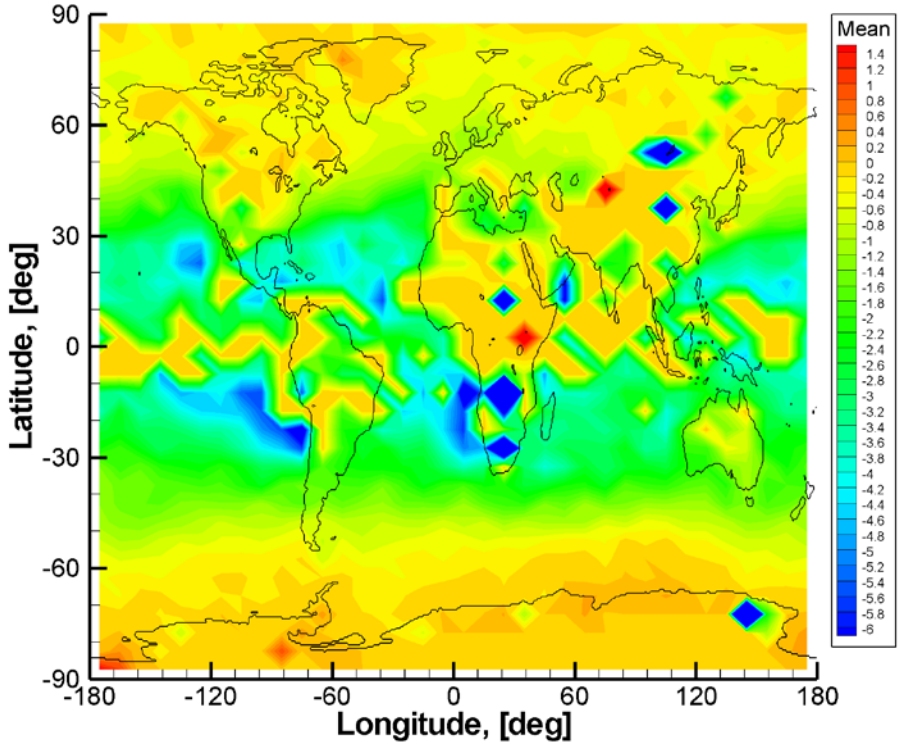

Fig. 78. Statistical comparison of GRAS –ECMWF refractivities (O-B/B, %) at an altitude of 0.5 km.

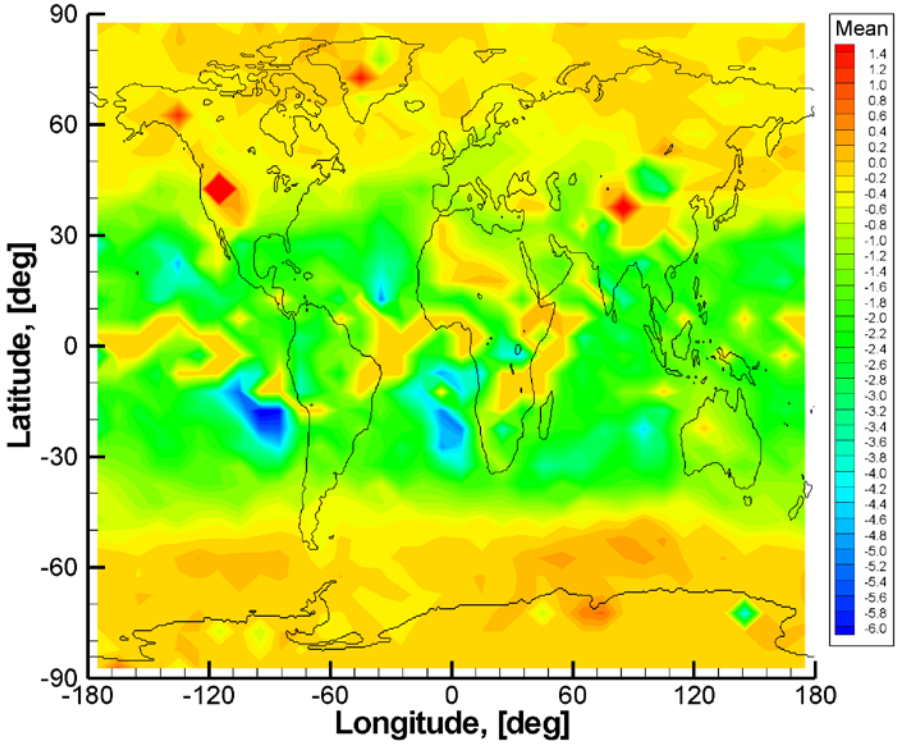

Fig. 79. Statistical comparison of GRAS –ECMWF refractivities (O-B/B, %) at an altitude of 1.0 km.

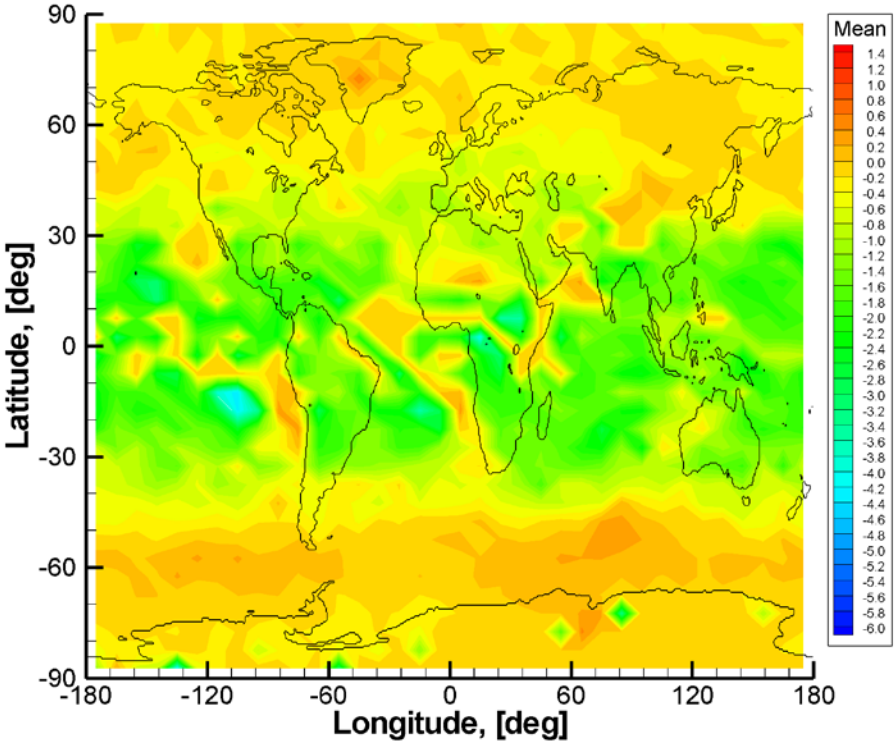

Fig. 80. Statistical comparison of GRAS –ECMWF refractivities (O-B/B, %) at an altitude of 1.5 km.

4. Numerical Simulations

4.1 Simulation of Wave Propagation in Turbulent Atmosphere

Our method of simulation of wave propagation in turbulent atmosphere uses the phase screen method. Similar simulations were described in [20,21]. In those papers, random realizations of the field of turbulent fluctuations of atmospheric refractivity was generated, and the resulting sum of the regular refractivity and its fluctuations was employed in the phase screen method. Such an approach may require large computational resources, when modeling small scale turbulence, because in this case the step between screens must also be small. We modify this approach. Instead of modeling random realizations of the fluctuations of atmospheric refractivity, we generate random realization of the screen-to-screen phase path (further referred to as the phase thickness). This allows for modeling even isotropic small-scale turbulence without decreasing the scree-to-screen step.
In order to derive the statistical properties of the phase thickness of a screen. Consider a plane layer of the turbulent medium with thickness Δx between plane phase screen located at x and $x+\Delta x$, where x is the coordinate along the propagation direction. Phase thickness is function $\Psi(x,\Delta x,y,z)$, where y and z are the spatial coordinates transverse to x. The function is understood as a realization of 2D random field as function of y,z with some fixed x and Δx. Consider the corresponding realization of 3D field of refractivity fluctuations $\Delta N(x,y,z)$. The following relation between fluctuations of refractivity and fluctuations of the phase thickness $\Delta\Psi$ can be written:

$$\Delta\Psi(x,\Delta x,y,z)=\int_{x}^{x+\Delta x}\Delta N(x',y,z)\,dx'. \tag{1}$$

The field of $\Delta N(x,y,z)$ is assumed to be statistically homogeneous and isotropic with the spectral density $\Phi_{\Delta N}(\boldsymbol{\kappa})=\Phi_{\Delta N}(\kappa)$, where $\boldsymbol{\kappa}=(\kappa_x,\kappa_y,\kappa_z)$ is the vector of spatial frequencies, $\kappa=|\boldsymbol{\kappa}|$. The correlation function is given by the standard relationship [22]:

$$\left\langle \Delta N(\mathbf{r}_1)\Delta N^{*}(\mathbf{r}_2)\right\rangle=\int\exp\left(i\boldsymbol{\kappa}(\mathbf{r}_1-\mathbf{r}_2)\right)\Phi_{\Delta N}(\boldsymbol{\kappa})\,d^3\boldsymbol{\kappa}. \tag{2}$$

Consider the correlation of the phase thickness:

$$\left\langle \Delta\Psi(x,\Delta x,y',z')\Delta\Psi(x,\Delta x,y'',z'')\right\rangle=$$

$$=\int_{x}^{x+\Delta x}\int_{x}^{x+\Delta x}\left\langle \Delta N(x',y',z')\Delta N(x'',y'',z'')\right\rangle dx'\,dx''= \tag{3}$$

$$=\int_{x}^{x+\Delta x}\int_{x}^{x+\Delta x}\int\exp\left(i\left(\kappa_x(x'-x'')+\kappa_y(y'-y'')+\kappa_z(z'-z'')\right)\right)\Phi_{\Delta N}(\boldsymbol{\kappa})\,d^3\boldsymbol{\kappa}\,dx'\,dx''.$$

Integrating here over $dx'\,dx''$, we arrive at the following integral expression:

$$\int_x^{x+\Delta x} \exp\left(i\kappa_x x'\right) dx' \int_x^{x+\Delta x} \exp\left(-i\kappa_x x''\right) dx'' =$$

$$= \frac{1}{i\kappa_x}\left[\exp\left(i\kappa_x\left(x+\Delta x\right)\right)-\exp\left(i\kappa_x x\right)\right]\frac{1}{-i\kappa_x}\left[\exp\left(-i\kappa_x\left(x+\Delta x\right)\right)-\exp\left(-i\kappa_x x\right)\right] = \quad (4)$$

$$= \frac{1}{\kappa_x^2}\left[\exp\left(i\kappa_x\Delta x\right)-1\right]\left[\exp\left(-i\kappa_x\Delta x\right)-1\right] = \frac{2\left(1-\cos\left(\kappa_x\Delta x\right)\right)}{\kappa_x^2} = \Delta x^2\,\mathrm{sinc}^2\left(\frac{\Delta x\,\kappa_x}{2}\right).$$

Substituting this into (3), we obtain the following formula:

$$\left\langle \Delta\Psi\left(x,\Delta x,y',z'\right)\Delta\Psi\left(x,\Delta x,y'',z''\right)\right\rangle = \quad (5)$$

$$= \Delta x^2 \int \exp\left(i\left(\kappa_y\left(y'-y''\right)+\kappa_z\left(z'-z''\right)\right)\right)\mathrm{sinc}^2\left(\frac{\Delta x\,\kappa_x}{2}\right)\Phi_{\Delta N}\left(\boldsymbol{\kappa}\right)d^3\boldsymbol{\kappa}.$$

Because the following relationship must hold:

$$\left\langle \Delta\Psi\left(x,\Delta x,y',z'\right)\Delta\Psi\left(x,\Delta x,y'',z''\right)\right\rangle = \quad (6)$$

$$= \int \exp\left(i\mu_y\left(y'-y''\right)+i\mu_z\left(z'-z''\right)\right)\Phi_{\Delta\Psi}\left(\boldsymbol{\mu}\right)d\mu_y\,d\mu_z,$$

we conclude that

$$\Phi_{\Delta\Psi}\left(\boldsymbol{\mu}\right) = \Delta x^2 \int \mathrm{sinc}^2\left(\frac{\Delta x\,\kappa_x}{2}\right)\Phi_{\Delta N}\left(\kappa_x,\mu_y,\mu_z\right)d\kappa_x. \quad (7)$$

For large Δx the essential contribution into this integral comes from the vicinity of 0, because the kernel $\mathrm{sinc}^2\left(\frac{\Delta x\,\kappa_x}{2}\right)$ has a sharp maximum there and for $\Delta x \to \infty$ the kernel is approximated as δ-function up to a factor that will defined below. We can, therefore, write:

$$\Phi_{\Delta\Psi}\left(\boldsymbol{\mu}\right) = \Phi_{\Delta N}\left(0,\mu_y,\mu_z\right)\int \Delta x^2\,\mathrm{sinc}^2\left(\frac{\Delta x\,\kappa_x}{2}\right)d\kappa_x. \quad (8)$$

Evaluate this integral using the representation of kernel (4):

$$\int_x^{x+\Delta x}\int_x^{x+\Delta x} \exp\left(i\kappa_x\left(x'-x''\right)\right)dx'\,dx''\,d\kappa_x = \quad (9)$$

$$= 2\pi \int_x^{x+\Delta x}\int_x^{x+\Delta x} \delta\left(x'-x''\right)dx'\,dx'' = 2\pi\Delta x.$$

Therefore, for a layer of medium with a thickness exceeding the external scale of turbulence, we can write:

$$\Phi_{\Delta\Psi}\left(\boldsymbol{\mu}\right) = 2\pi\,\Delta x\,\Phi_{\Delta N}\left(0,\mu_y,\mu_z\right). \quad (10)$$

This expression describes the 2D spectrum of phase thickness. In our simulations, we use 1D phase screens. The corresponding 1D spectrum is evaluated as follows:

$$\Phi^{1D}_{\Delta\Psi}\left(\boldsymbol{\mu}\right) = 2\pi\,\Delta x \int \Phi_{\Delta N}\left(0,\mu_y,\mu_z\right)d\mu_y. \quad (11)$$

For the turbulent fluctuations of refractivity, we will adopt the Kolomogorov – von Kármán spectrum:

$$\Phi_{\Delta N}(\kappa) = 0.033 C_n^2\left(\kappa^2+\kappa_0^2\right)^{-11/6}\exp\left(-\kappa^2/\kappa_m^2\right), \quad (12)$$

where C_n^2 is the structural constant, $\kappa_0 = 2\pi / L_0$, L_0 is the external scale, $\kappa_m = 5.92 / l_0$, and l_0 is the internal scale of turbulence.

In the simulations C_n^2 is assumed to be a function of altitude z. Because the real turbulence is not necessarily isotropic, $C_n^2(z)$ is treated not as the actual structural constant, but as an effective turbulence magnitude, which we select in such a way that the fluctuations of the simulated field should have realistic values. In particular, we assumed $C_n^2(0\ \text{km}) = 8\times10^{-10}\ \text{m}^{-2/3}$ and $C_n^2(4\ \text{km}) = 10^{-14}\ \text{m}^{-2/3}$.

In nature, turbulence can be synergetic with super-refraction and has an average latitudinal dependence. We did not simulate these effects and assumed C_n^2 to only be a function of altitude.

4.2 Results

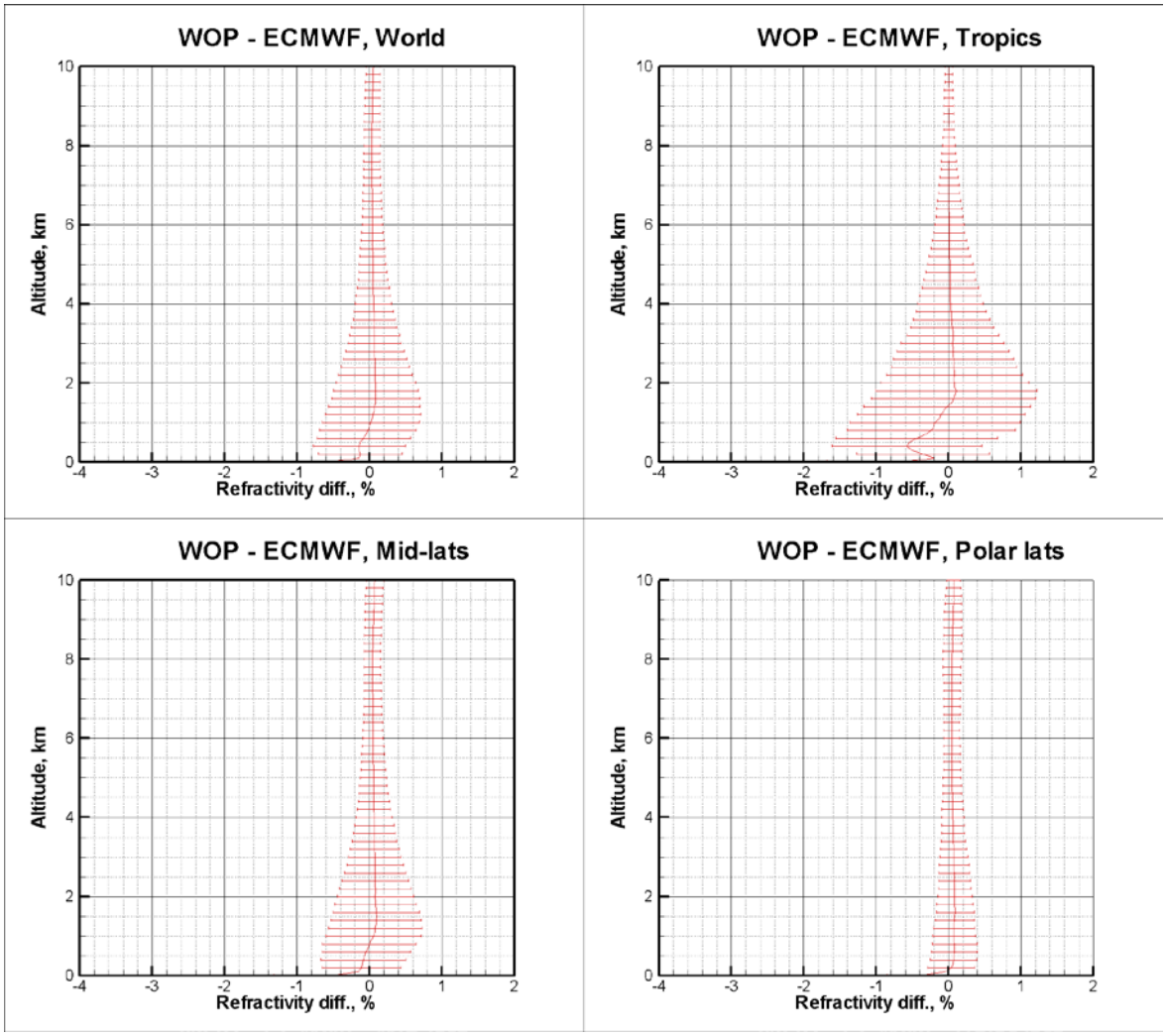

Fig. 81. End-to-end simulations without turbulence. Differences between retrieved and local profiles. Systematic errors are caused by super-refraction and horizontal gradients.

Fig. 81 present the statistical result for simulations without turbulence. In the tropics, we observe the negative systematic retrieval error. The error magnitude is much smaller than that observed in COSMIC–ECMWF comparisons. The systematic error comes from both super-refraction and horizontal gradients.

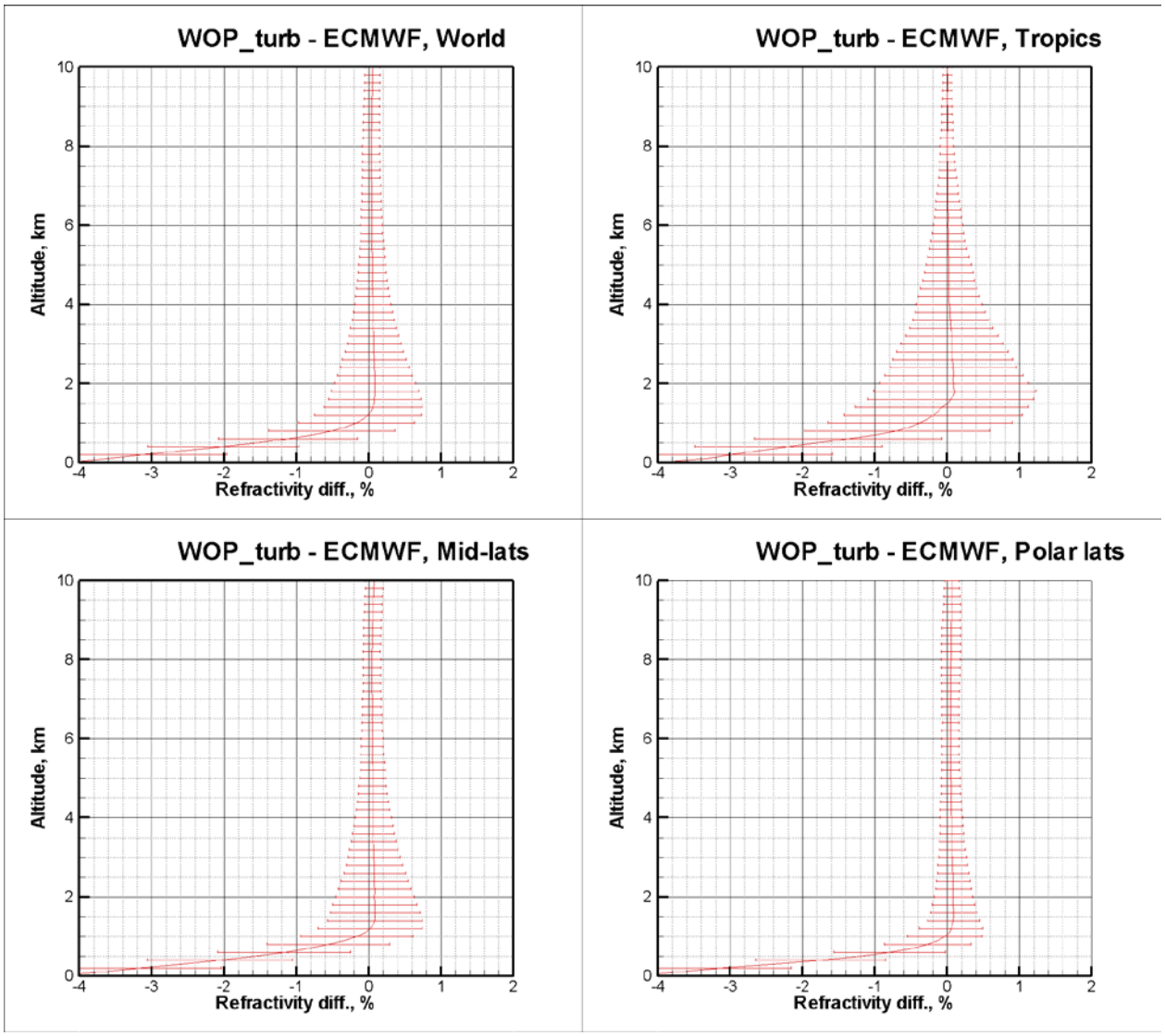

Fig. 82. End-to-end simulation with turbulence: differences of refractivities.

Fig. 82 shows the difference of the retrieved refractivity in simulations with turbulence. The introduction of turbulence results in a negative bias of refractivity.

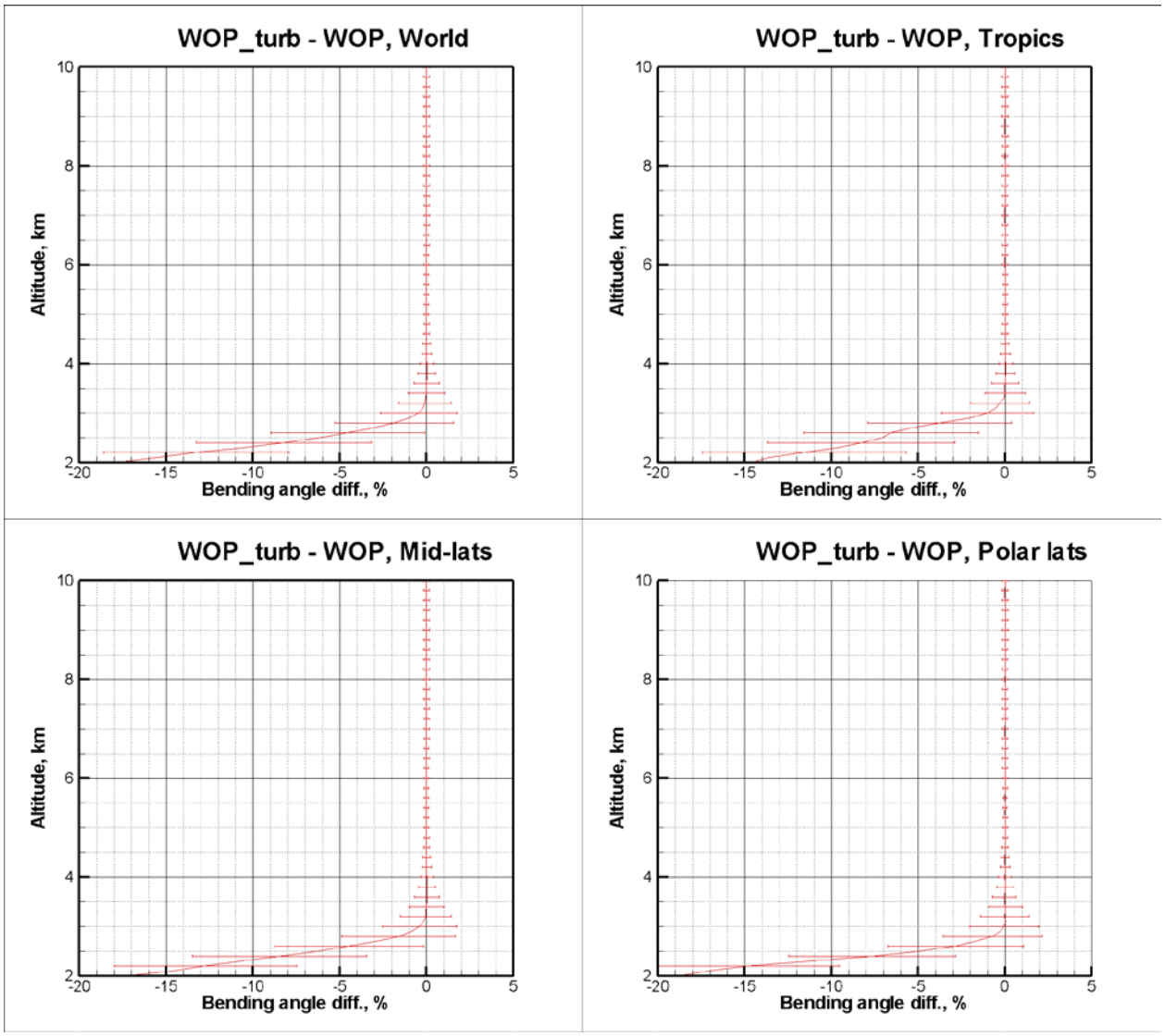

Fig. 83. End-to-end simulation with and without turbulence: differences of bending angles.

Fig. 83 shows the results for bending angles: turbulence results in the negative bias of bending angles. The following considerations indicate that random turbulence must result in a negative bias of bending angles (V.Vorob'ev, private communication).
In [22] there is a discussion of the evaluation of mean field in the 1st order of the smooth perturbation method. In [23] the equation for the mean field in the Markov approximation is derived and solved.
Consider the plane incident wave in the turbulent medium:

$$E = \exp(\chi + i\phi) \tag{13}$$

If the fluctuations of logarithmic amplitude χ and phase ϕ are normally distributed, the following relation for the mean field can be written:

$$\begin{aligned} \langle E \rangle &= \exp\left(\langle \chi \rangle + i\langle \phi \rangle + \frac{1}{2}\left\langle (\chi + i\phi)^2 \right\rangle \right) = \\ &= \exp\left[\langle \chi \rangle + \frac{1}{2}\langle \chi^2 \rangle - \frac{1}{2}\langle \phi^2 \rangle + i\left(\langle \phi \rangle + \langle \chi\phi \rangle \right) \right] \end{aligned} \tag{14}$$

In the Markov approximation, the following expression for the mean field is obtained:

$$\langle E \rangle = \exp\left[-\frac{1}{2} \langle \phi^2 \rangle \right] \tag{15}$$

Because expressions (14) and (15) must be identically equal, the following relations must hold:

$$< \chi > + \frac{1}{2} < \chi^2 >= 0 \tag{16}$$

$$< \phi > + < \chi\phi >= 0 \tag{17}$$

From (17) the following relation is inferred:

$$< \phi >= - < \chi\phi > \tag{18}$$

Therefore, turbulence changes the mean phase $\langle \phi \rangle$ of the field. In the smooth perturbation method [22], under the condition $\lambda L >> l_0^2$, where L is the propagation distance, the following relation is derived:

$$< \chi\phi >= \mathrm{ctg}(\frac{\pi}{12}) < \chi^2 > \approx 3.7 < \chi^2 > \tag{19}$$

The value of $\langle \phi \rangle \approx -3.7 \langle \chi^2 \rangle$ is negative. We see, therefore, that turbulence results in a negative bias of the mean phase. Because the bias of the mean phase decreases with the impact height, this will also imply a negative bias of bending angles.

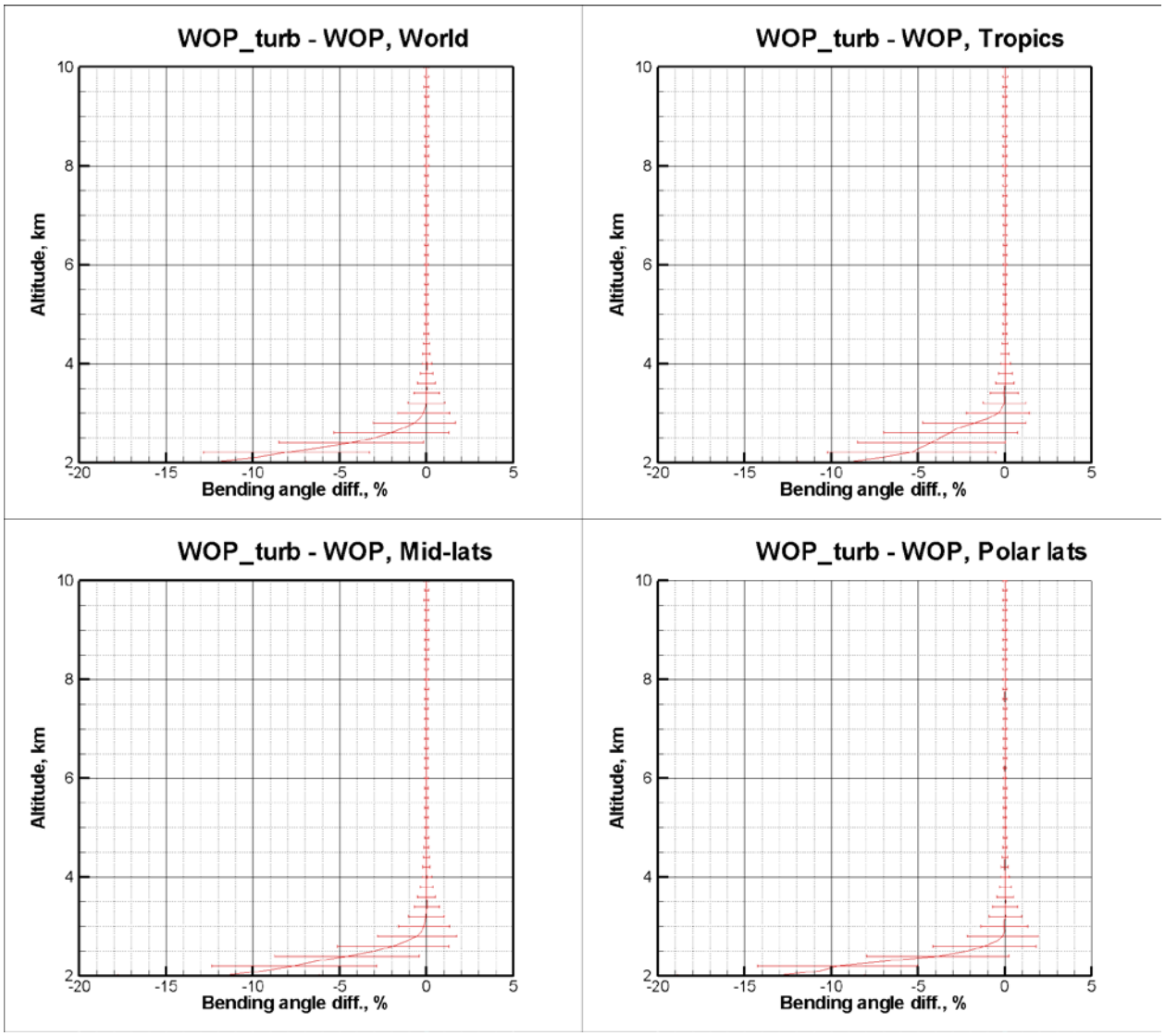

Fig. 84. End-to-end simulation with and without turbulence: differences of bending angles. Turbulence is two times weaker as compared to Fig. 83. The systematic effect caused by turbulence is proportional to the turbulence strength described by C_n^2.

The phase bias is quadratic with respect to random fluctuations of refractivity. This implies that the negative bias must be proportional to C_n^2. In order to verify this, we conducted another numerical simulation, where C_n^2 was two times lesser than in the previous runs. The results are shown in Fig. 84. The resulting biases in bending angles also decreased twice.

Fig. 85 through Fig. 90 present the detailed statistics of refractivity retrieval for end-to-end simulations without turbulence.

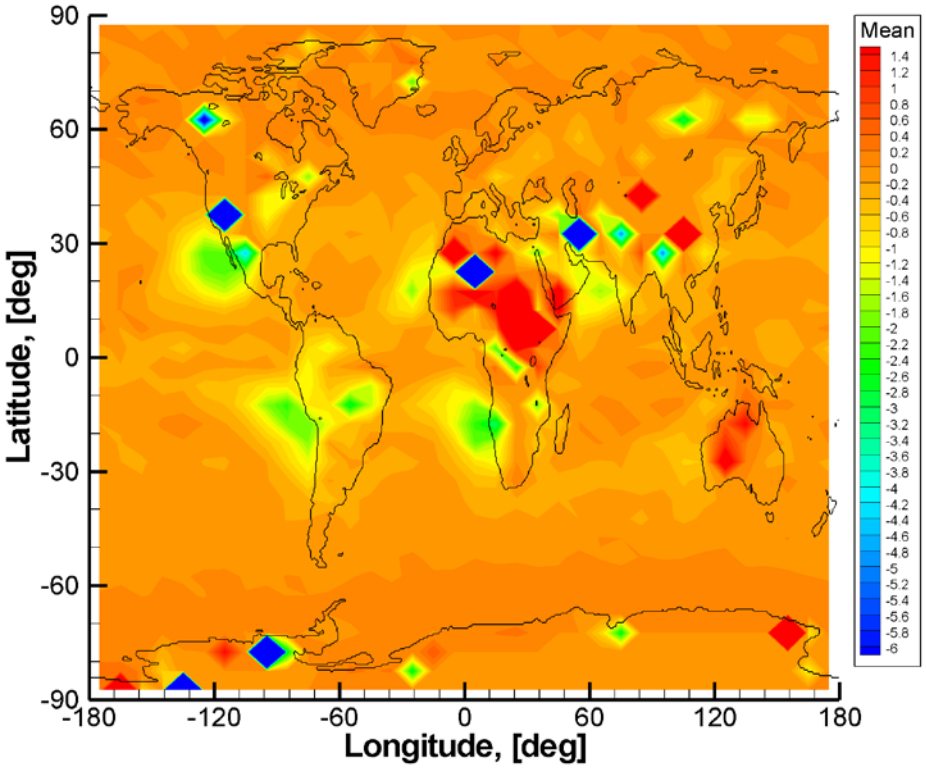

Fig. 85. Systematic error of ECMWF refractivity retrieval in end-to-end simulation with WOP (O-B/B, %) at an altitude of 0.2 km.

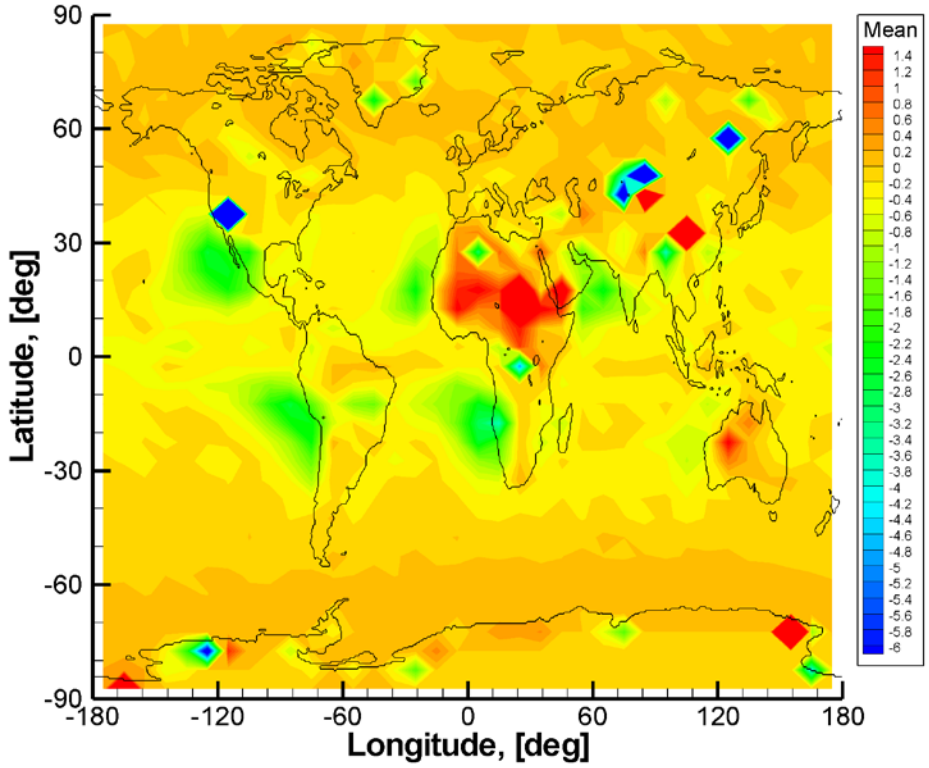

Fig. 86. Systematic error of ECMWF refractivity retrieval in end-to-end simulation with WOP (O-B/B, %) at an altitude of 0.3 km.

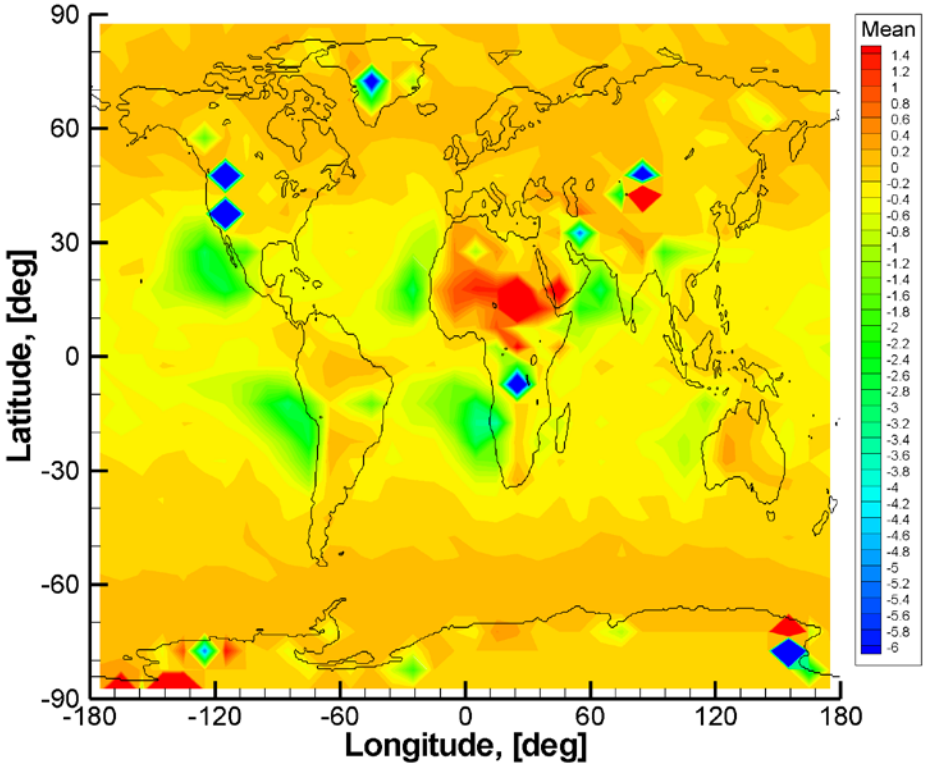

Fig. 87. Systematic error of ECMWF refractivity retrieval in end-to-end simulation with WOP (O-B/B, %) at an altitude of 0.4 km.

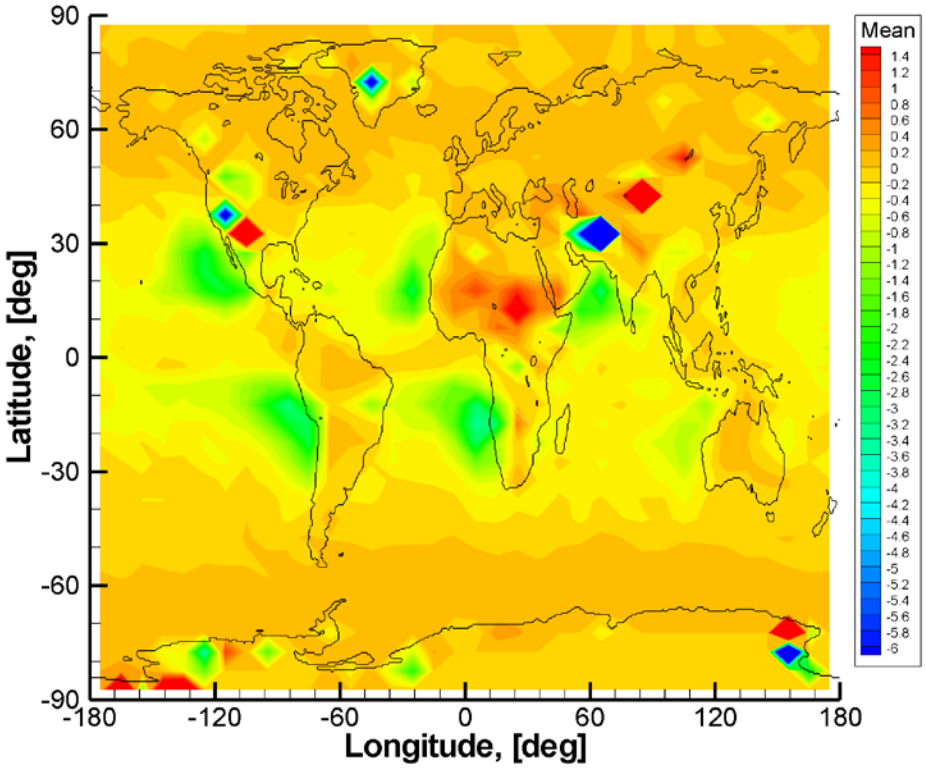

Fig. 88. Systematic error of ECMWF refractivity retrieval in end-to-end simulation with WOP (O-B/B, %) at an altitude of 0.5 km.

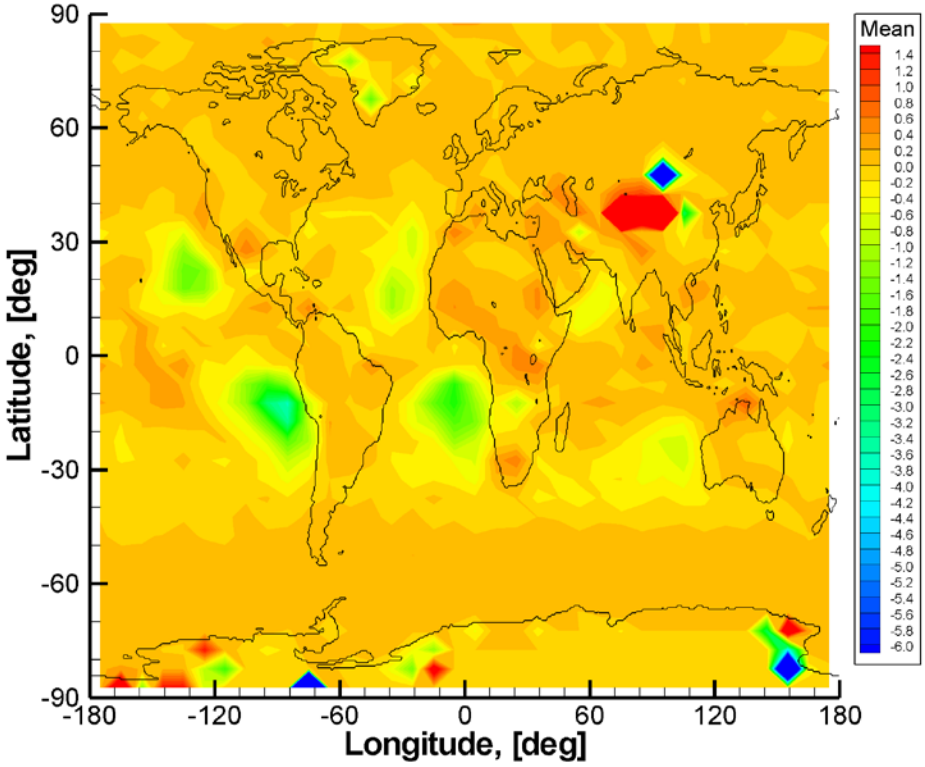

Fig. 89. Systematic error of ECMWF refractivity retrieval in end-to-end simulation with WOP (O-B/B, %) at an altitude of 1.0 km.

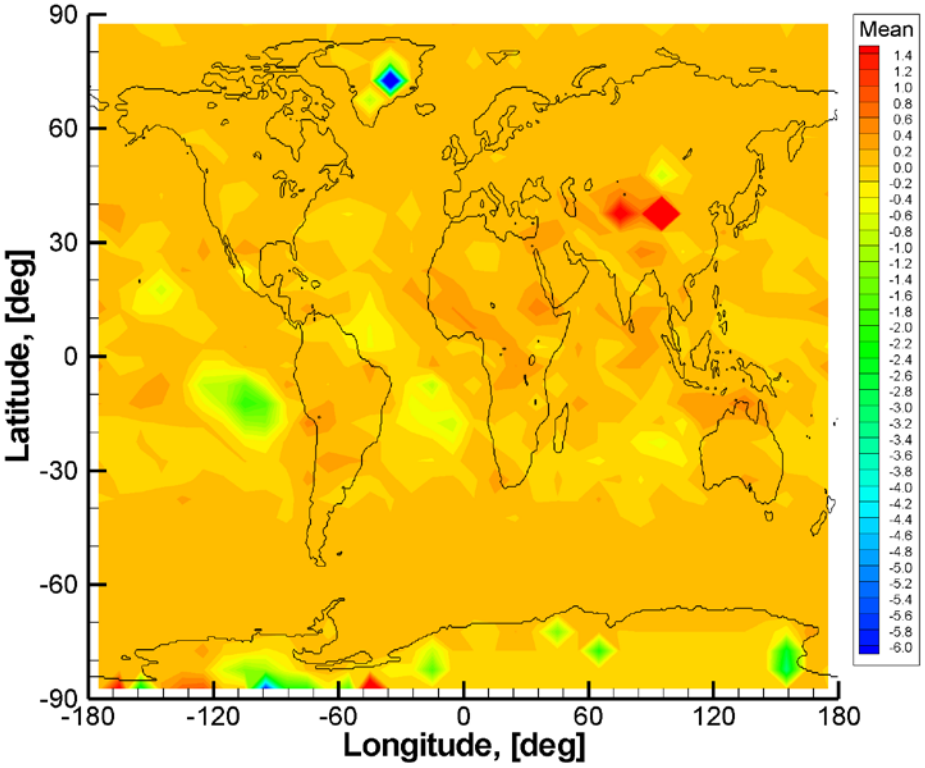

Fig. 90. Systematic error of ECMWF refractivity retrieval in end-to-end simulation with WOP (O-B/B, %) at an altitude of 1.5 km.

These simulations reproduce the areas with pronounced negative bias due to super-refraction. The magnitude of the bias is weaker than in the COSMIC–ECMWF comparisons, still these areas are clearly distinguished from the other regions.
Fig. 91 through Fig. 96 present the statistical analysis of end-to-end simulations with turbulence.

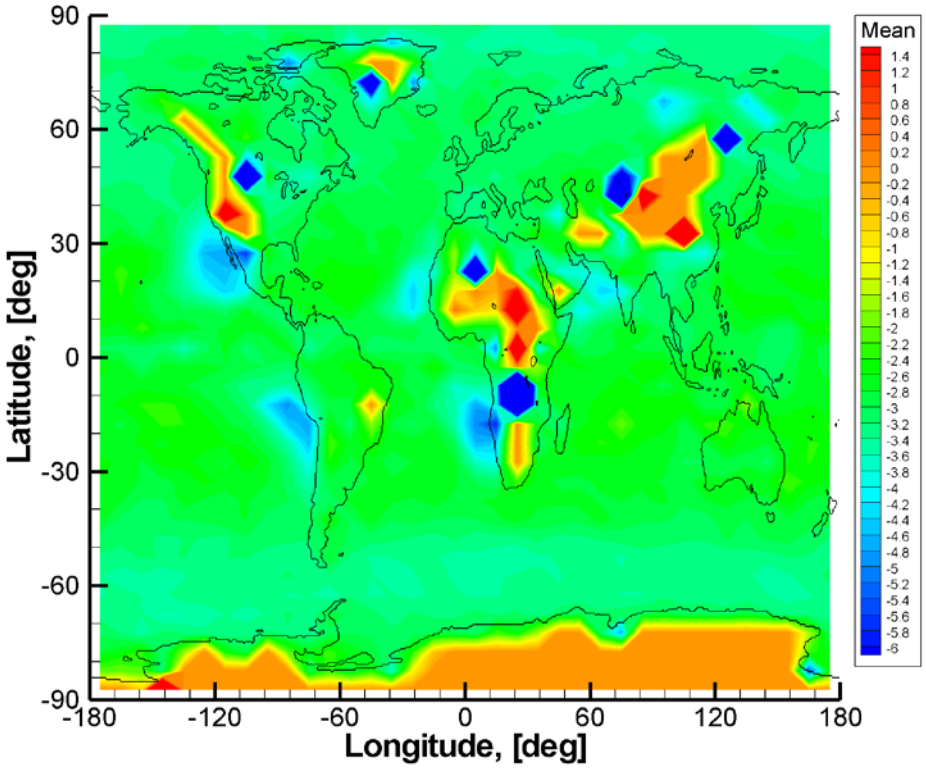

Fig. 91. Systematic error of ECMWF refractivity retrieval in end-to-end simulation with WOP including turbulence (O-B/B, %) at an altitude of 0.2 km.

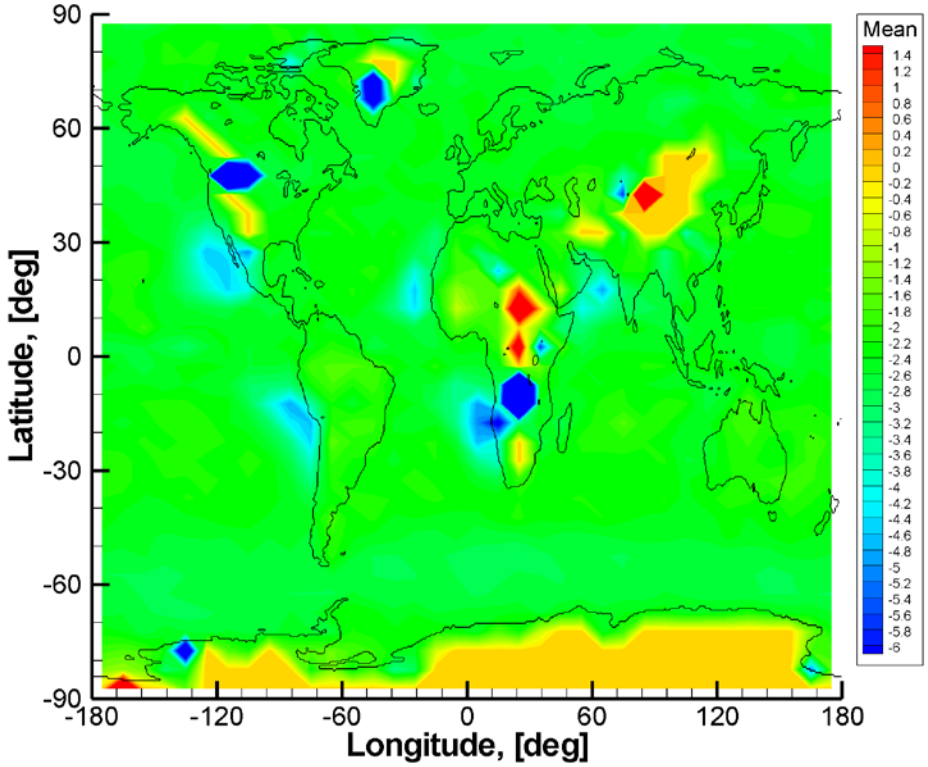

Fig. 92. Systematic error of ECMWF refractivity retrieval in end-to-end simulation with WOP including turbulence (O-B/B, %) at an altitude of 0.3 km.

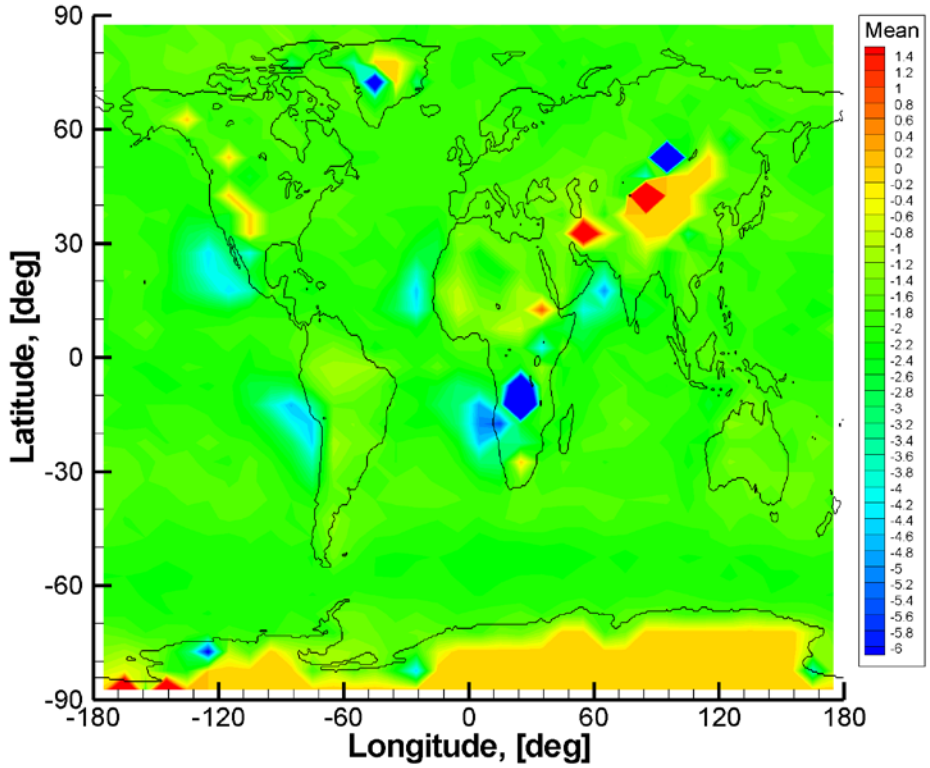

Fig. 93. Systematic error of ECMWF refractivity retrieval in end-to-end simulation with WOP including turbulence (O-B/B, %) at an altitude of 0.4 km.

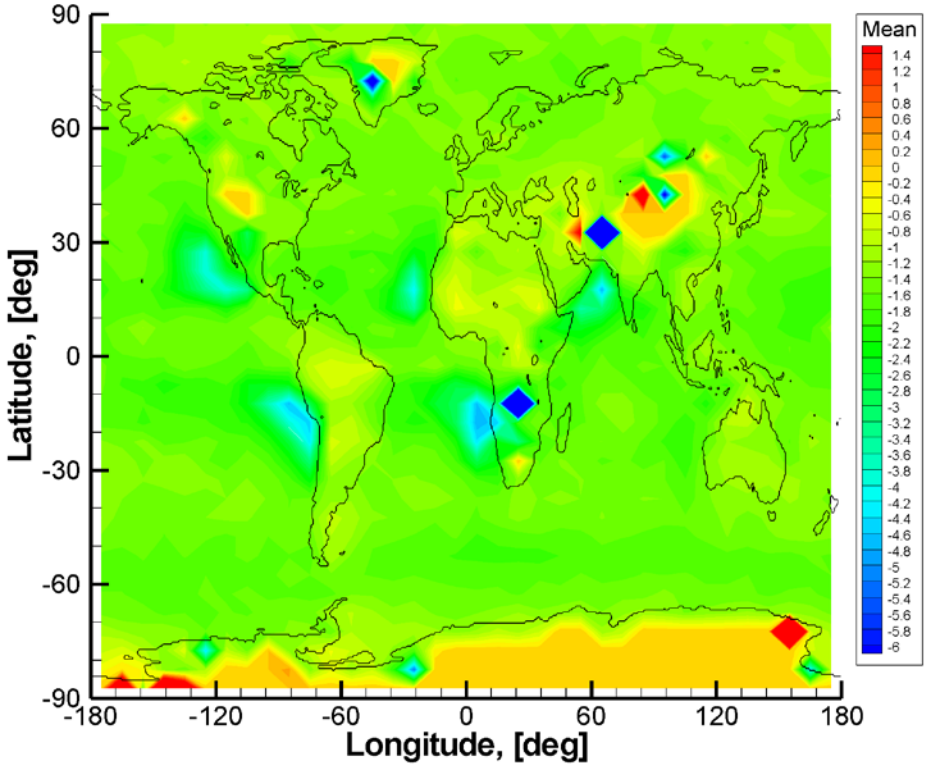

Fig. 94. Systematic error of ECMWF refractivity retrieval in end-to-end simulation with WOP including turbulence (O-B/B, %) at an altitude of 0.5 km.

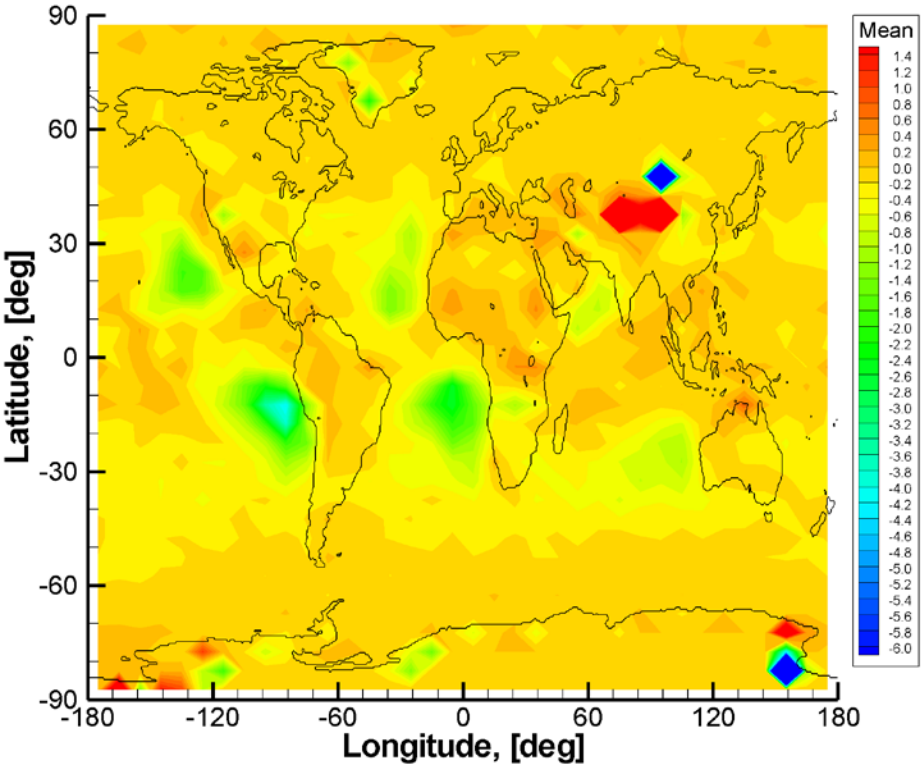

Fig. 95. Systematic error of ECMWF refractivity retrieval in end-to-end simulation with WOP including turbulence (O-B/B, %) at an altitude of 1.0 km.

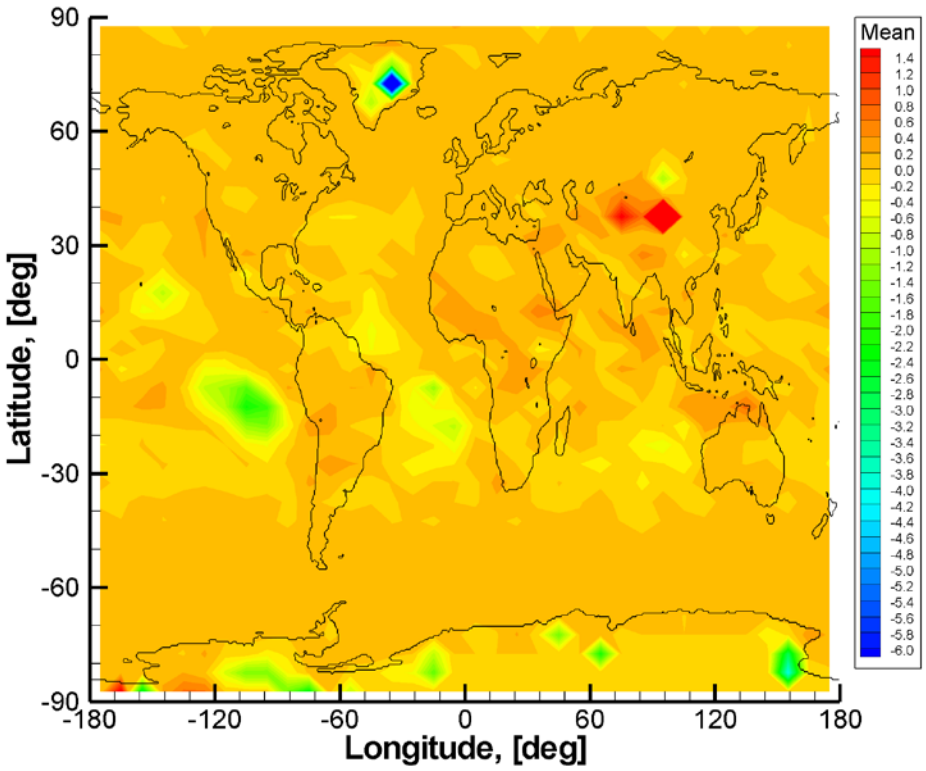

Fig. 96. Systematic error of ECMWF refractivity retrieval in end-to-end simulation with WOP including turbulence (O-B/B, %) at an altitude of 1.5 km.

In these simulations, turbulence amplifies the negative bias, and the results in the tropics get closer to the COSMIC–ECMWF comparisons. Note, we use uniform profile $C_n^2(z)$ independent from latitude, while in reality turbulence must decrease when approaching polar areas.
Fig. 97 through Fig. 109 show bending angle errors due to turbulence, from the same numerical simulations.

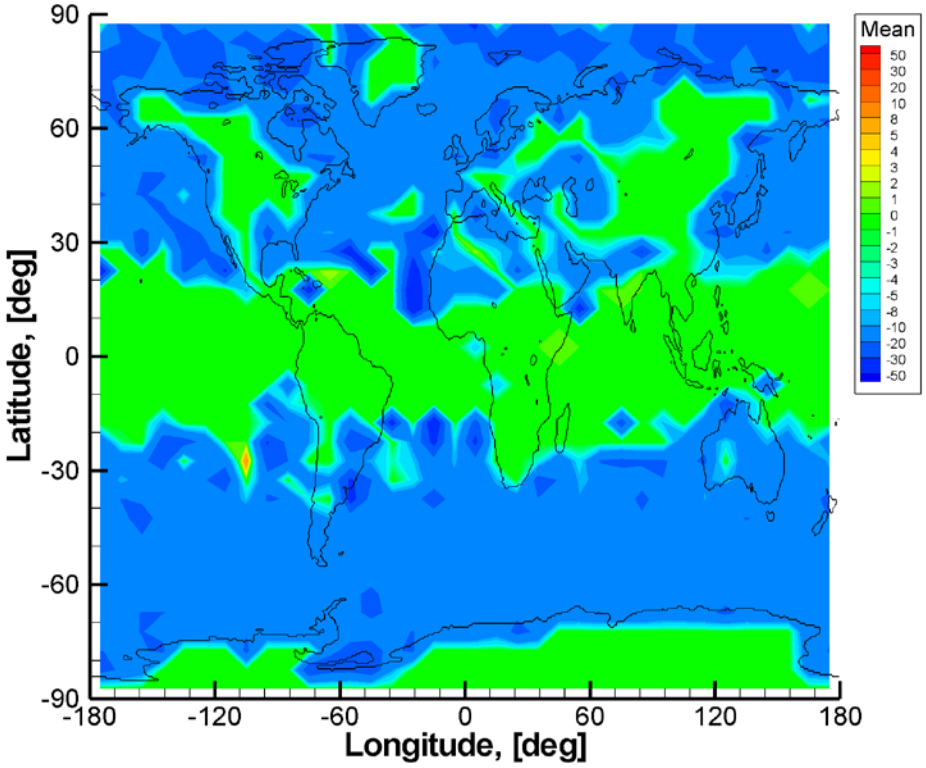

Fig. 97. Systematic difference of ECMWF bending angles simulated with WOP with and without turbulence (O-B/B, %) at an impact height of 2.0 km.

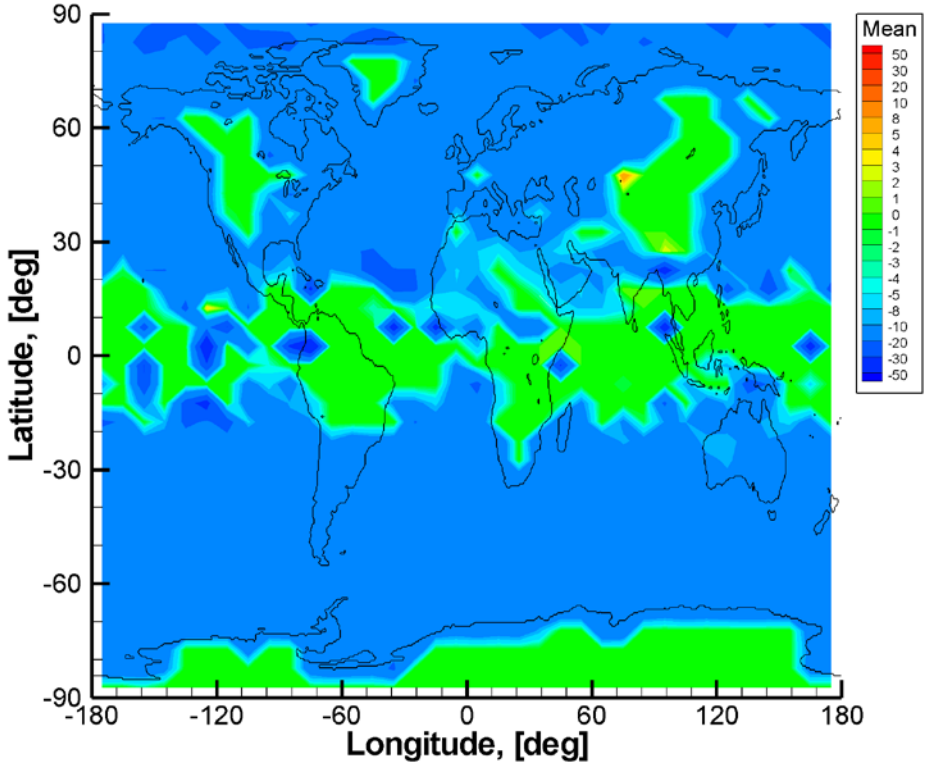

Fig. 98. Systematic difference of ECMWF bending angles simulated with WOP with and without turbulence (O-B/B, %) at an impact height of 2.1 km.

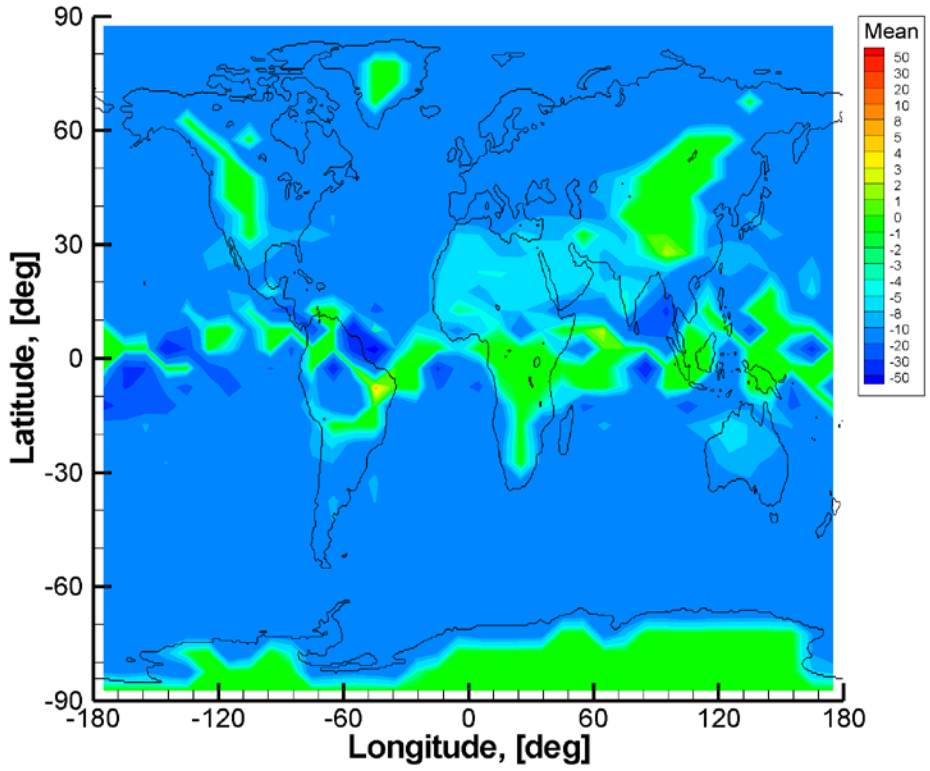

Fig. 99. Systematic difference of ECMWF bending angles simulated with WOP with and without turbulence (O-B/B, %) at an impact height of 2.2 km.

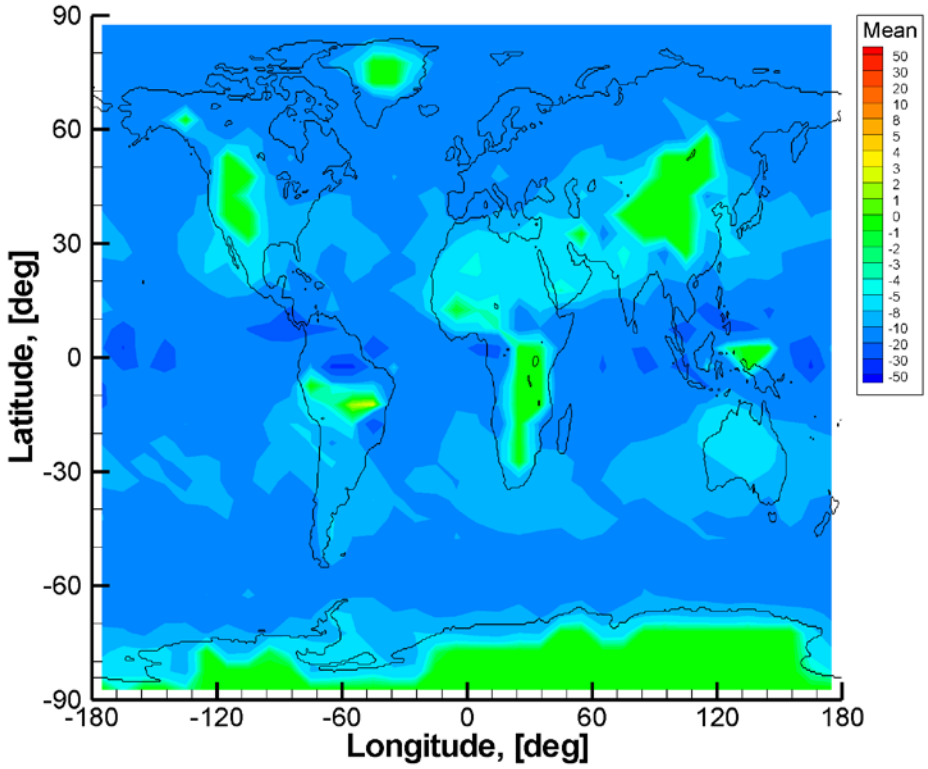

Fig. 100. Systematic difference of ECMWF bending angles simulated with WOP with and without turbulence (O-B/B, %) at an impact height of 2.3 km.

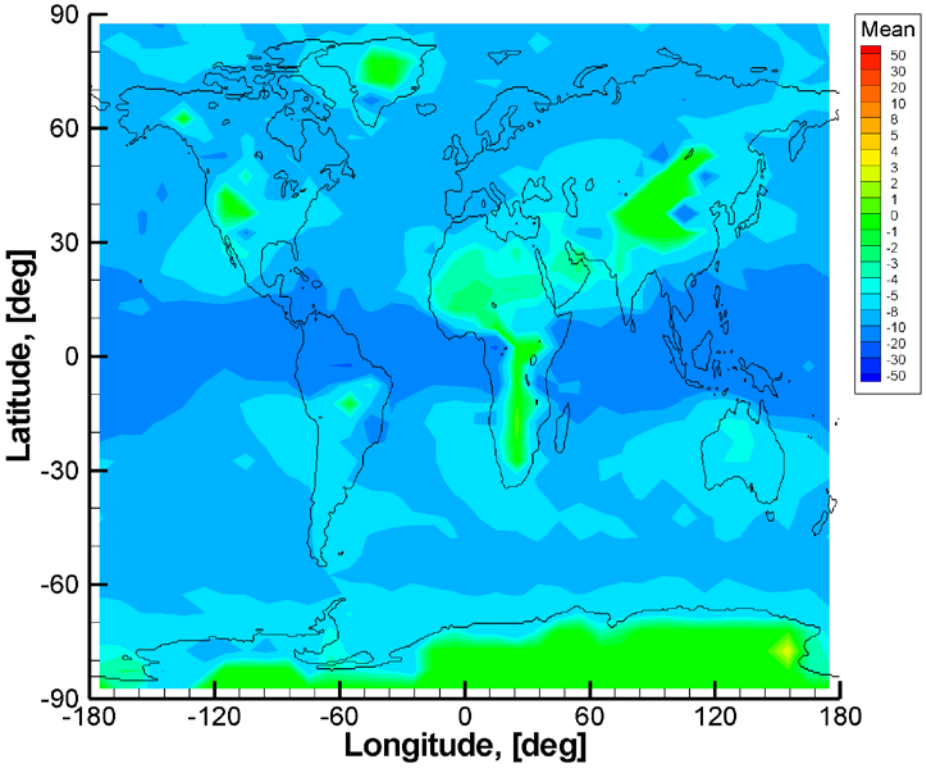

Fig. 101. Systematic difference of ECMWF bending angles simulated with WOP with and without turbulence (O-B/B, %) at an impact height of 2.4 km.

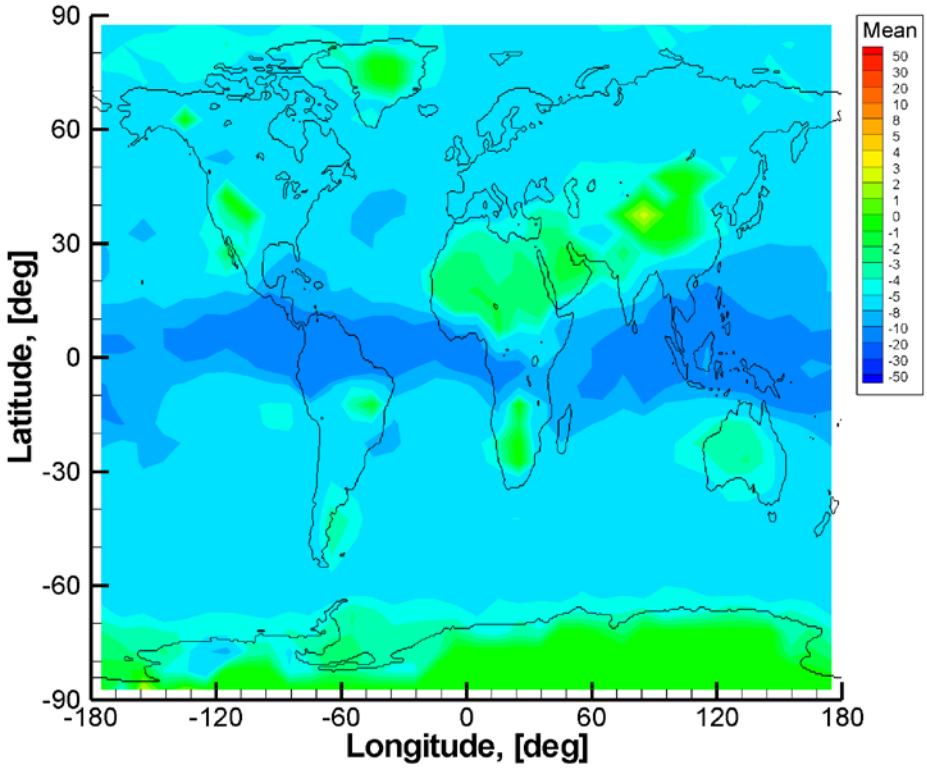

Fig. 102. Systematic difference of ECMWF bending angles simulated with WOP with and without turbulence (O-B/B, %) at an impact height of 2.5 km.

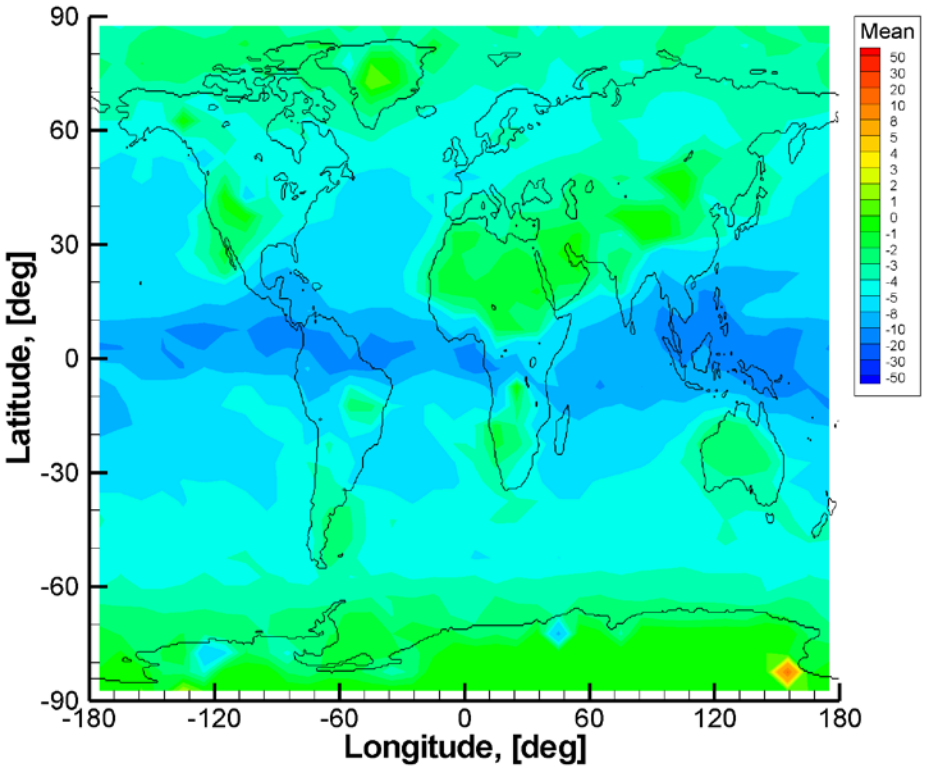

Fig. 103. Systematic difference of ECMWF bending angles simulated with WOP with and without turbulence (O-B/B, %) at an impact height of 2.6 km.

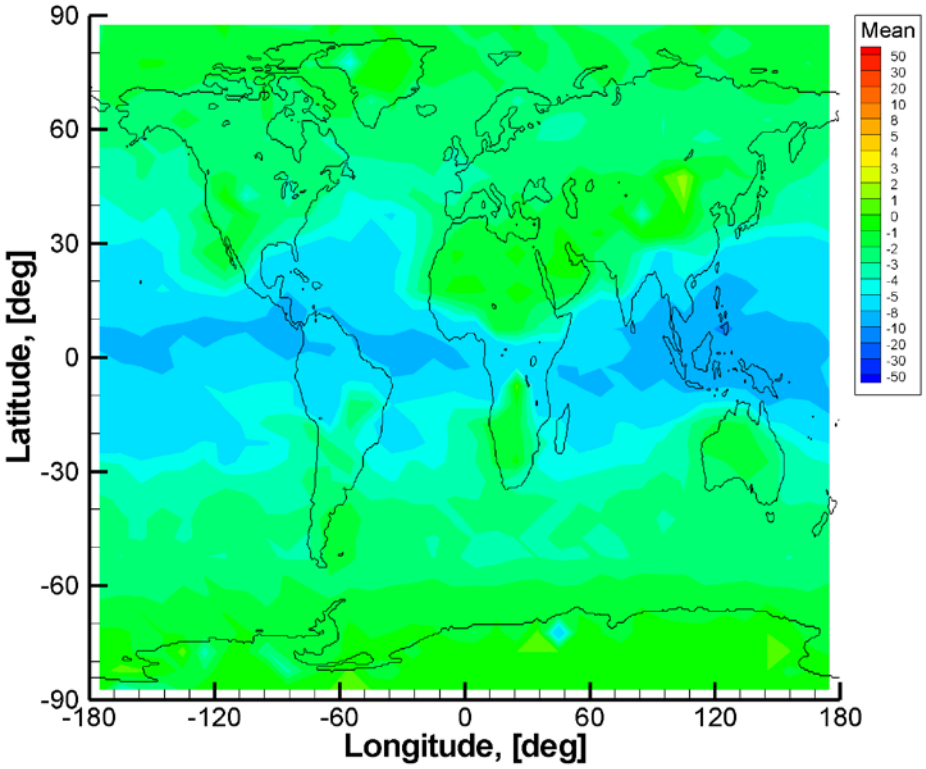

Fig. 104. Systematic difference of ECMWF bending angles simulated with WOP with and without turbulence (O-B/B, %) at an impact height of 2.7 km.

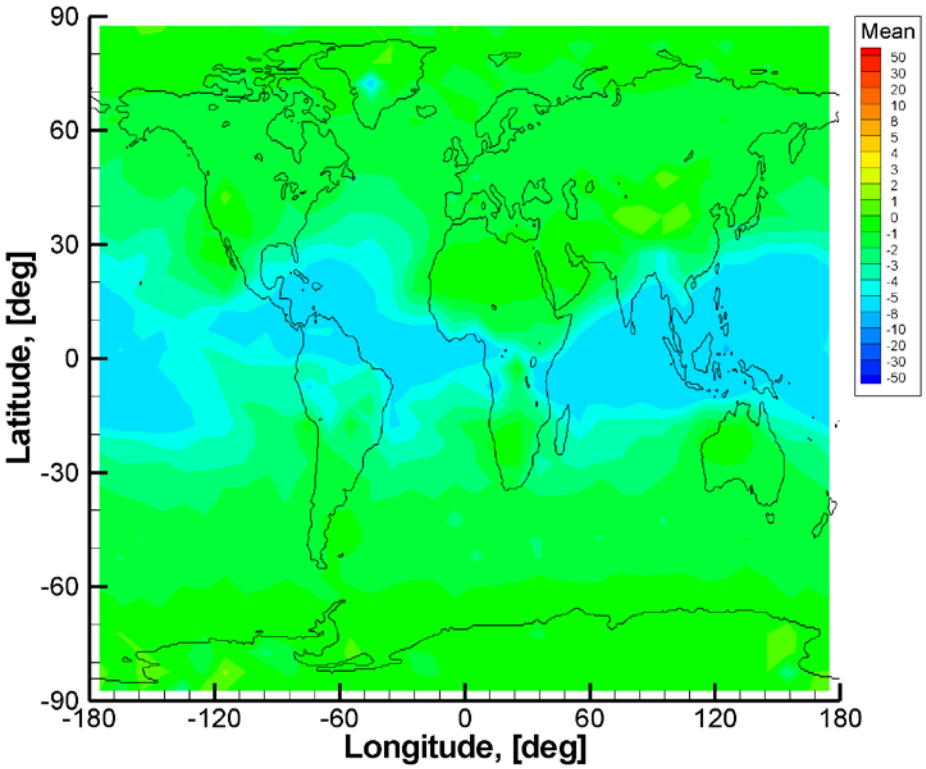

Fig. 105. Systematic difference of ECMWF bending angles simulated with WOP with and without turbulence (O-B/B, %) at an impact height of 2.8 km.

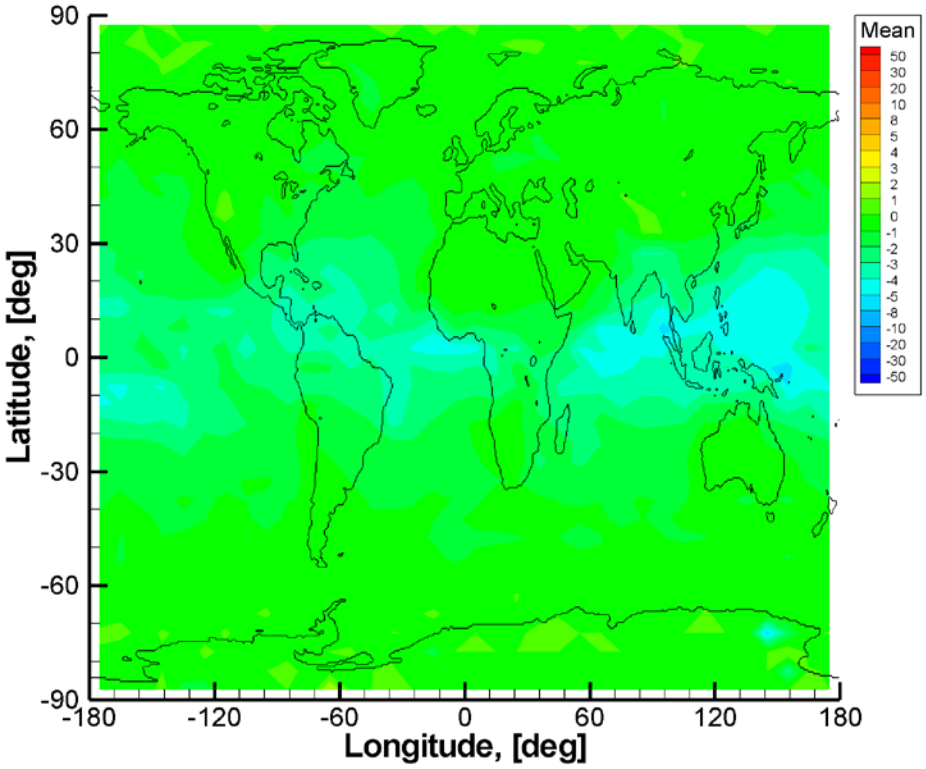

Fig. 106. Systematic difference of ECMWF bending angles simulated with WOP with and without turbulence (O-B/B, %) at an impact height of 2.9 km.

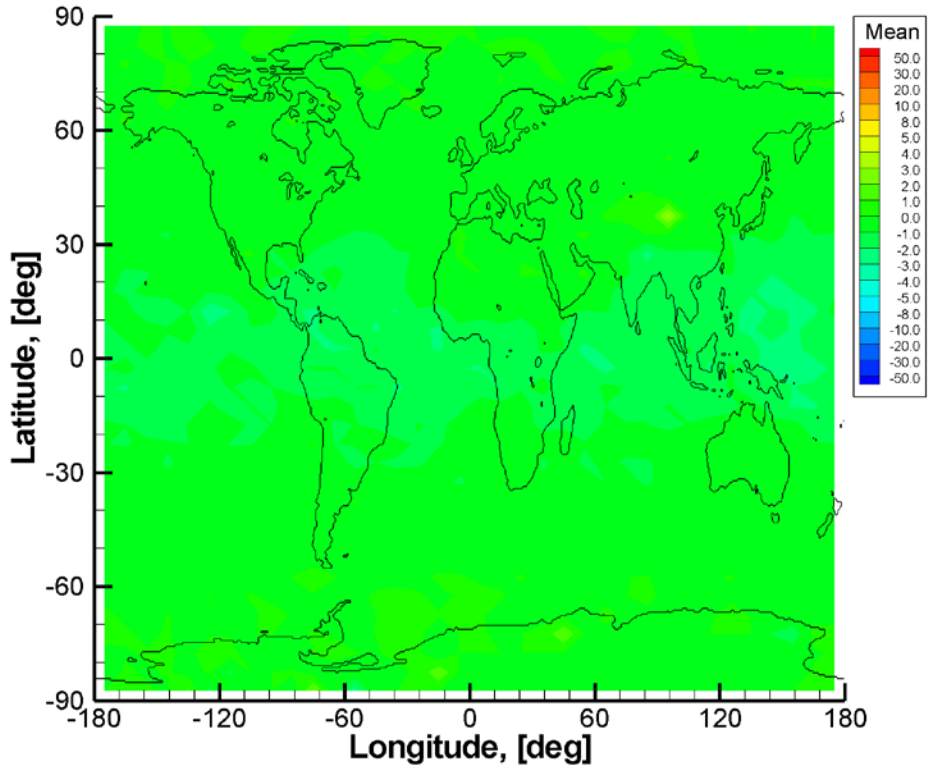

Fig. 107. Systematic difference of ECMWF bending angles simulated with WOP with and without turbulence (O-B/B, %) at an impact height of 3.0 km.

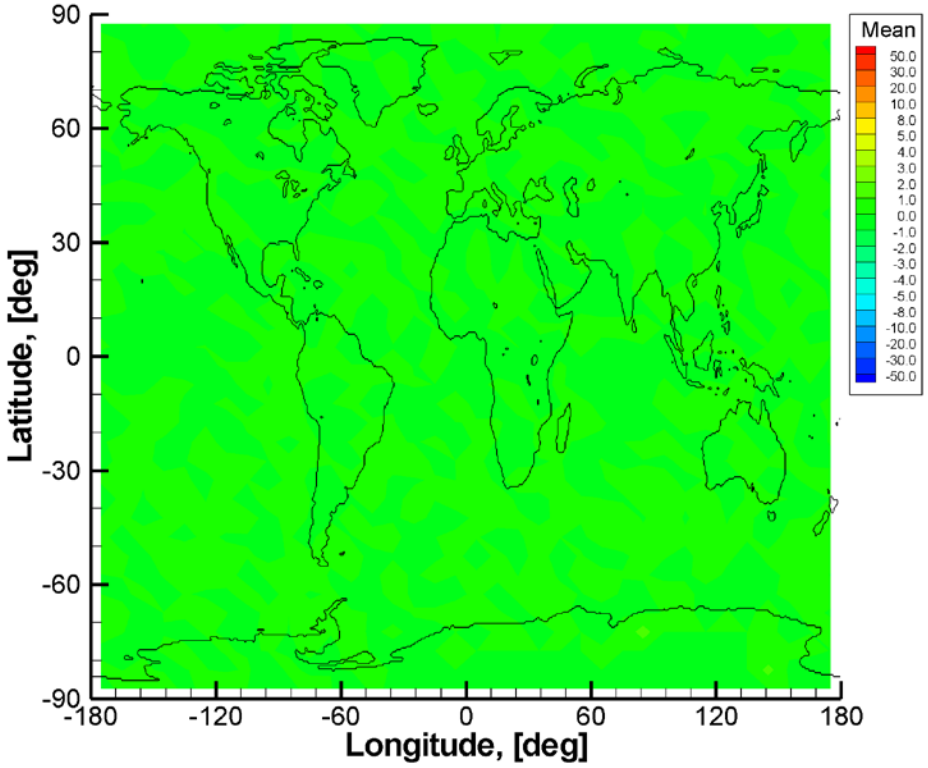

Fig. 108. Systematic difference of ECMWF bending angles simulated with WOP with and without turbulence (O-B/B, %) at an impact height of 3.5 km.

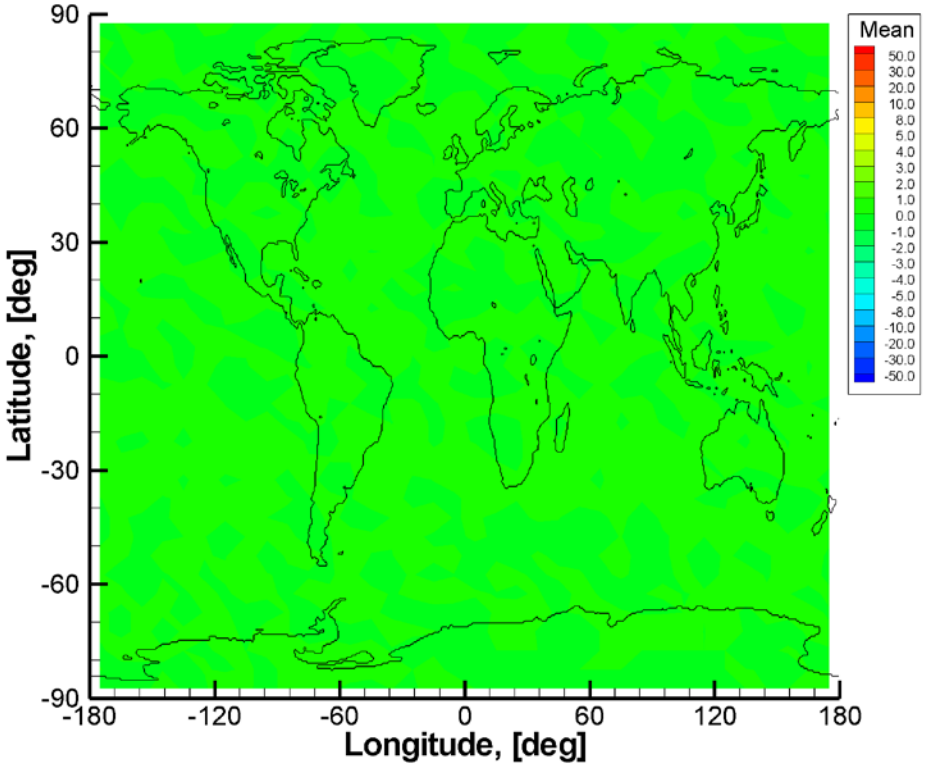

Fig. 109. Systematic difference of ECMWF bending angles simulated with WOP with and without turbulence (O-B/B, %) at an impact height of 4.0 km.

In this plots, bending angles do not indicate any significant increase in the areas of strong super-refraction in marine boundary layer, because we do not model the measurement noise and the cut-off of large bending angles.

5. Statistical Analysis of WOP-ITT Data

In a previous study 55 cases of COSMIC and GRAS RO events were selected by ECMWF in the framework of study of optimization of tracking strategies for radio occultation (WOP-ITT) [24]. Here we include a small set of figures in order to allow an easy comparison to the results and figures in chapter 4 for turbulence simulations. For the detailed comparison the reader is referred to [24].

The results of the statistical comparison of the WOP-ITT case with ECMWF analyses are presented in Fig. 110 and Fig. 111.

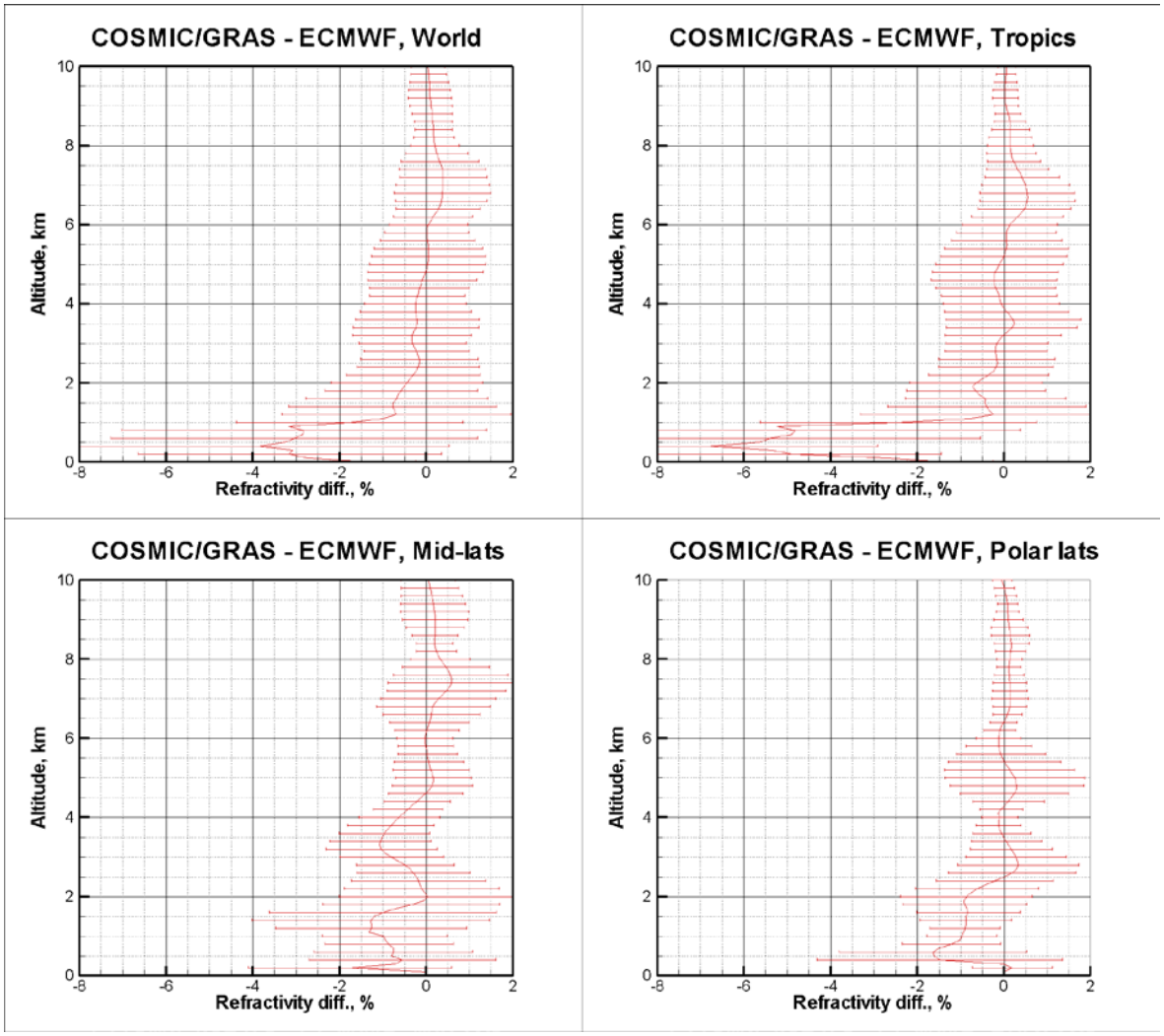

Fig. 110. WOP-ITT cases: statistical comparison of retrieved refractivity with ECMWF analyses.

Fig. 110 shows the statistics for refractivity retrieval. For the tropics, the statistics is characterized by a large negative bias sharply reaching 6% below 1 km height.

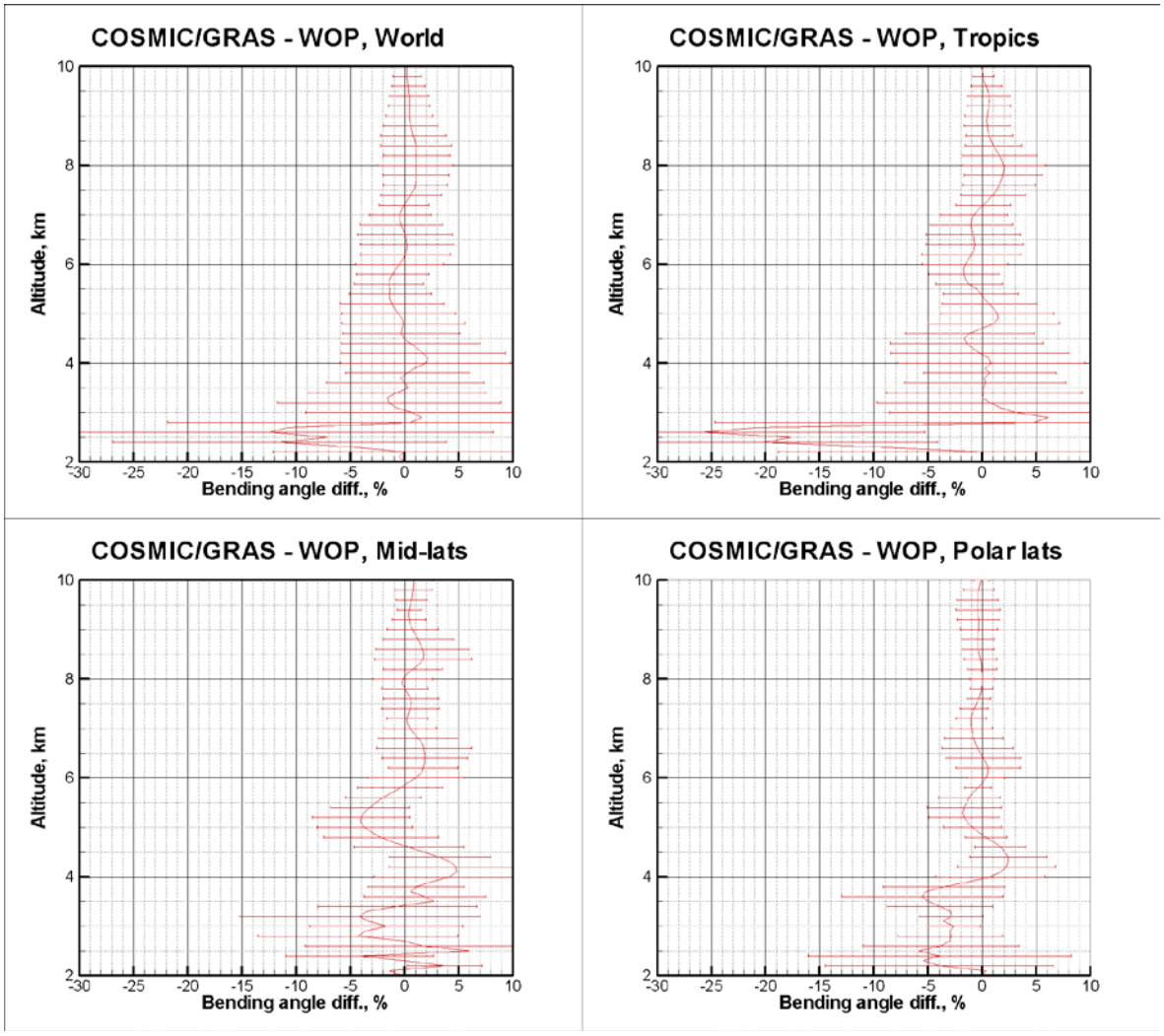

Fig. 111. WOP-ITT cases: statistical comparison of bending angles with ECMWF analyses.

Fig. 111 shows the statistical comparison of bending angles compared to simulated ones based on ECMWF analyses, without turbulence model. The statistics of the bending angles is also characterized by a sharp occurrence of a negative bias reaching 25% below 3 km impact height. The negative bias for the WOP-ITT selected cases exceeds the mean bias from all the observations (Fig. 1 and Fig. 2). This allows for the characterization of the selected cases as extreme ones.

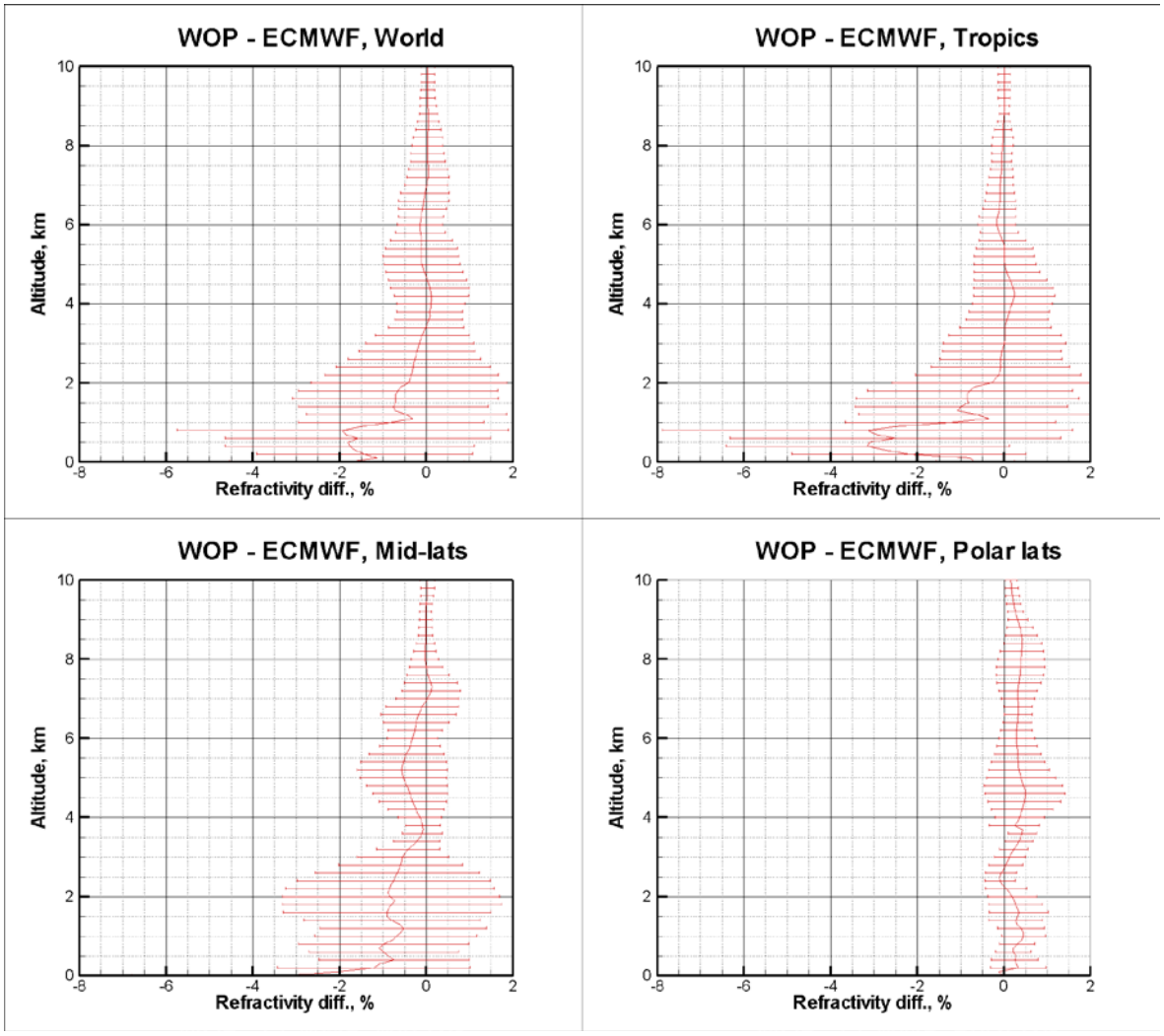

Fig. 112. WOP-ITT cases: statistical comparison of refractivity retrieved from ECMWF-simulated bending angles with 'true' values.

Fig. 112 shows the error of the retrieved refractivity in the end-to-end simulation. In the tropics, it also exceeds the error shown in Fig. 81. This indicates that the tropical WOP-ITT cases are located in super-refraction areas.

6. Statistical Analysis of Simulations with Radiosonde Data

In this chapter we present examples which address the difference in simulations based on ECMWF fields and radiosondes. Our objective is to understand the negative bias for low altitudes and a simulation assuming a spherically symmetric atmosphere (based on a radiosonde) will tend to exaggerate this. This is explained as follows. Local radiosonde profile often indicate a complicated structure with strong gradients exceeding the critical value. This may only represent local horizontally-inhomogeneous structure that do not necessarily corresponds to super-refraction. Taking local profile as a spherically-symmetric medium will, thus, overestimate the effect of super-refraction.

We performed end-to-end numerical simulations with radiosonde profiles available at http://weather.uwyo.edu/upperair/sounding.html. We chose about 100 radiosonde profile for January 2014 located in Colorado and Mexico from the following stations: Ft Worth (32.83°N, 97.30°W), Cancun (21.02°N, 86.85°W), Manzanillo (19.05N, 104.32W).
In the simulation, the vertical profiles were used for the simulation of a spherically symmetric atmosphere without horizontal gradients.

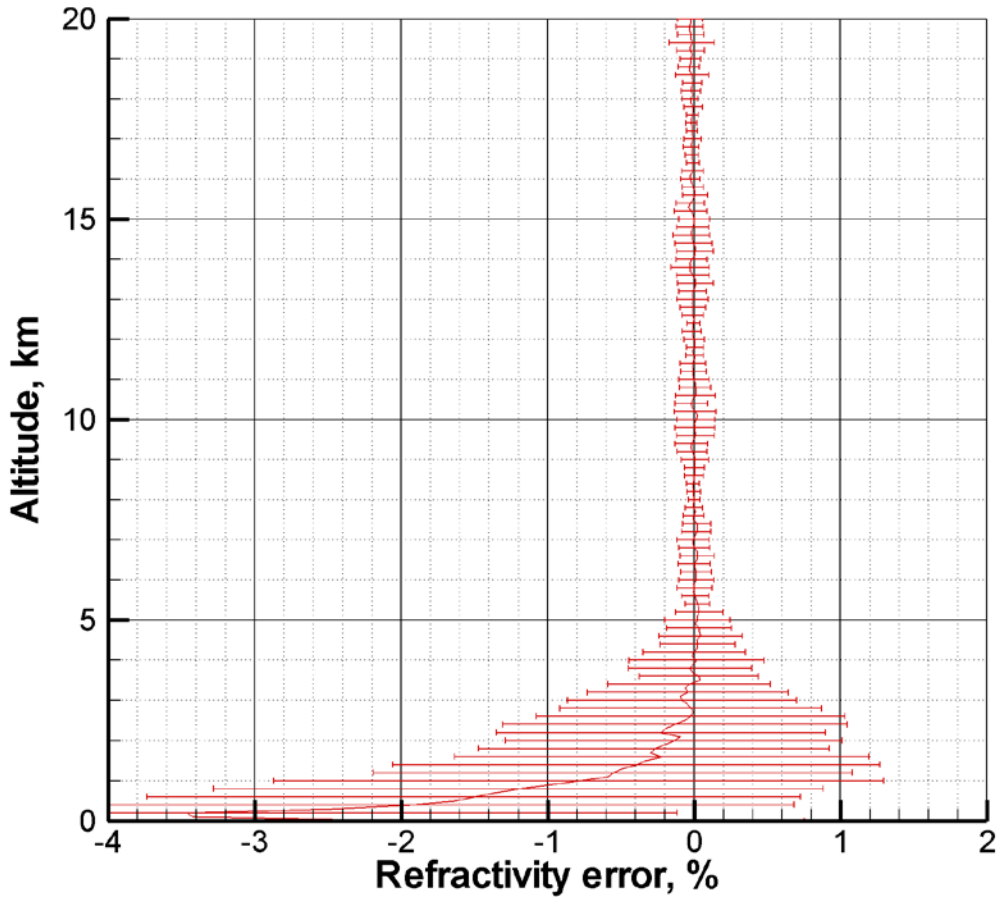

Fig. 113. Refractivity retrieval error in end-to-end simulation based on radiosonde data.

Fig. 113 shows the statistics of the refractivity retrieval error. Below 3 km a negative bias is observed, which is attributed to the artificially introduced super-refraction, due to the spherical symmetric simulation.

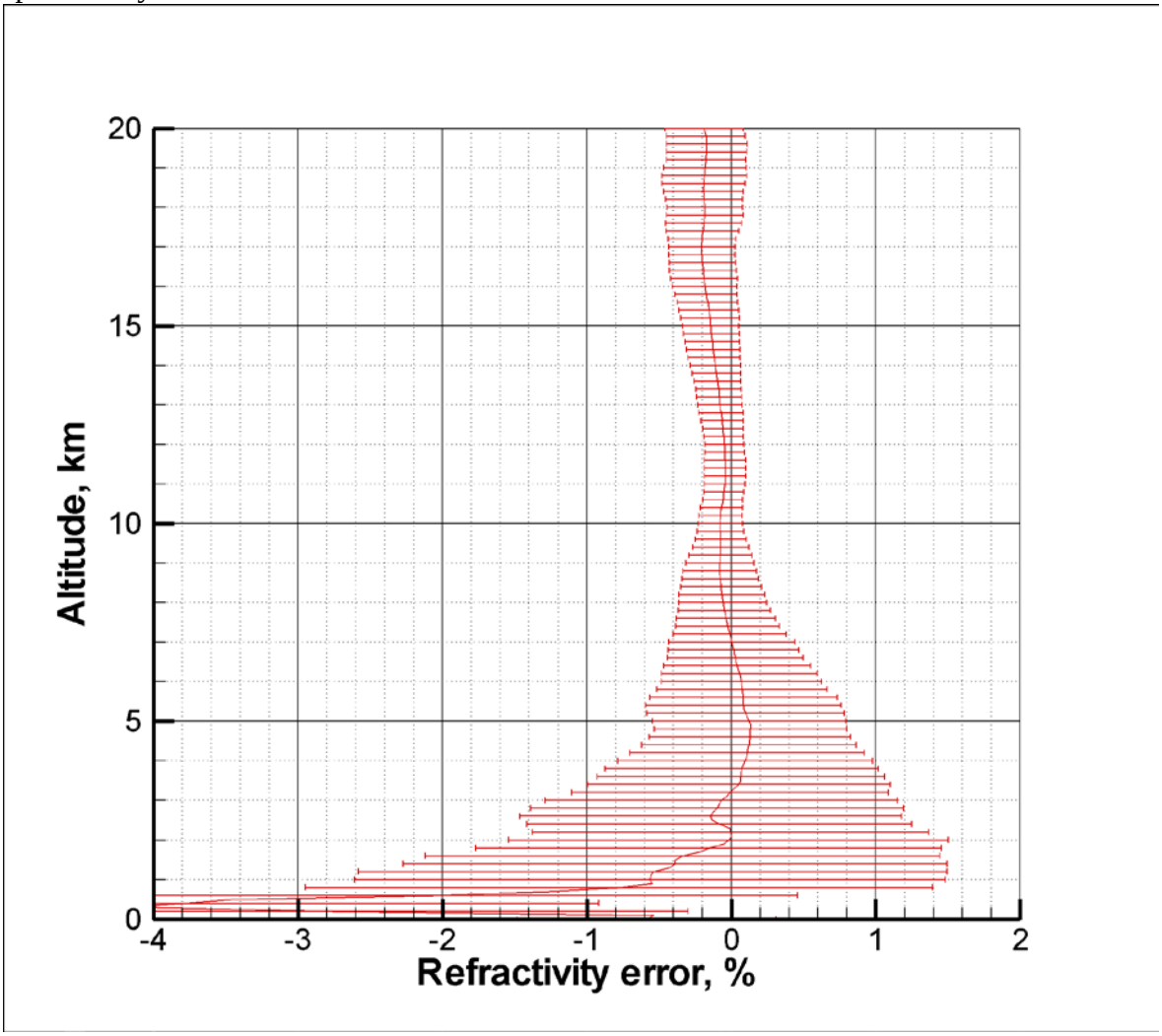

Fig. 114. Statistical comparison of refractivity from COSMIC observations and ECMWF analyses around 22.5°N 105.5°W.

Fig. 114 shows the statistical comparison of refractivity retrieved from COSMIC observations and ECMWF analyses for the region around 22.5°N 105.5°W, which corresponds to the location of the radiosonde observations. Here, the bias begins below 2 km and is weaker than that for radiosonde simulations in the height interval 1–2 km, but it is much stronger below 1 km.

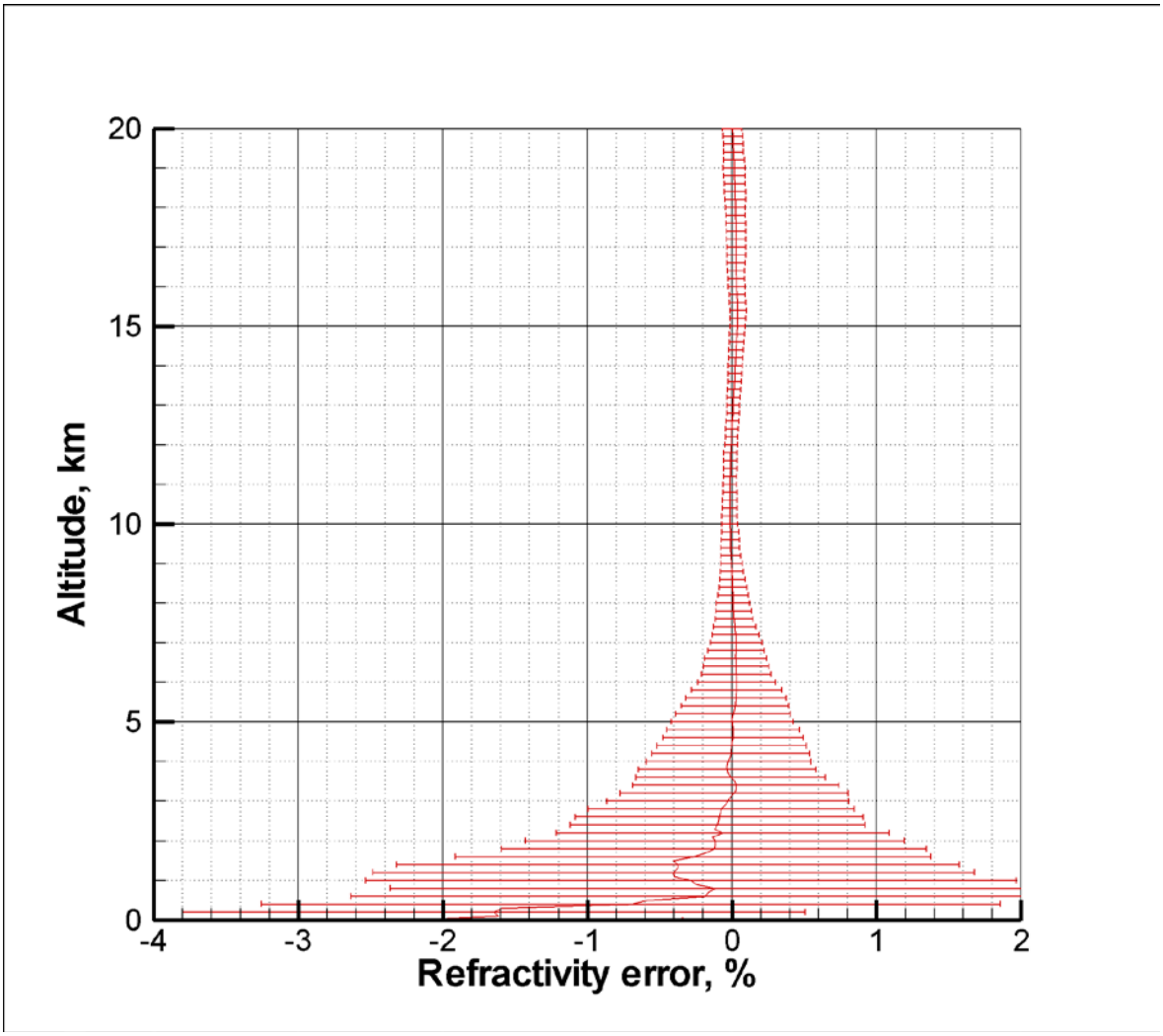

Fig. 115. End-to-end simulations without turbulence in region around 22.5°N 105.5°W. Differences between retrieved and local profiles.

Fig. 115 shows the refractivity retrieval error in the end-to-end simulation with ECMWF without turbulence analyses in the same region. These simulations also indicate a negative bias. In the height range 1–3 km the simulated bias is close to that in the observations. Below 1 km the simulated bias is weaker than that in the observations.

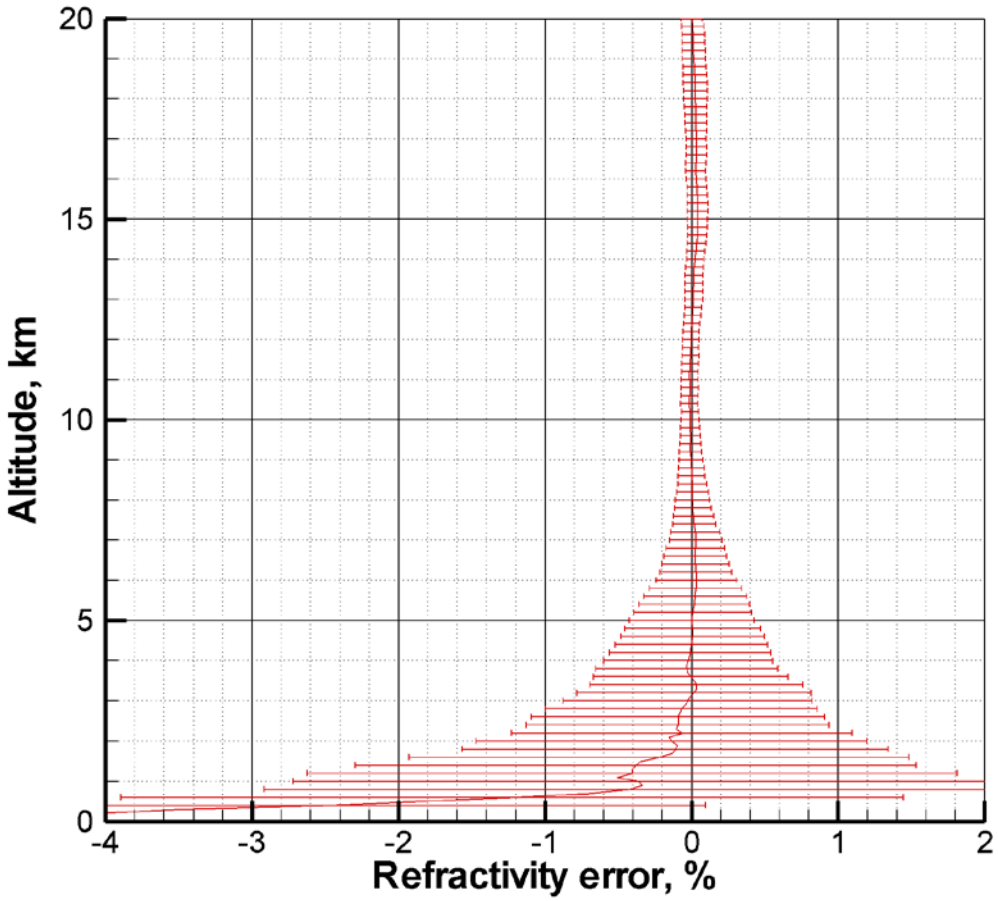

Fig. 116. End-to-end simulations with turbulence in region around 22.5°N 105.5°W. Differences between retrieved and local profiles.

Fig. 116 show similar end-to-end simulation, but with turbulence. The bias in this simulations is the closest to that in the real observations.

7. Conclusions

Negative bias of RO-retrieved refractivity with respect to the most accurate and up-to-date fields of atmospheric parameters produced by the most advanced models of global atmospheric circulation was noticed already during processing of the data of the first RO experiment, GPS/MET. Experiment CHAMP indicate very much the same value of the negative bias. It was recognized an important source of the bias was the closed-loop receiver. Under conditions of large phase excess rate and strong fluctuations, the receiver started to systematically lose cycles. Much hope was placed to open-loop receivers. Open-loop scheme was implemented in COSMIC experiment, and later in GRAS receiver carried by the METOP satellite. Although the open loop significantly improved the accuracy of observations in the lower troposphere and decreased systematic errors, the problem of the negative bias still persisted. After many studies it was recognized that it is not a single factor that results in the bias. The bias is a result of many different effects with different statistical properties.

The most notorious effect resulting in the N-bias is super-refraction. Super-refraction results in the negative bias even for unbiased bending angles. However, super-refraction under the realistic measurement conditions is also responsible for negative bias of bending angles. The reason is that large spikes of bending angles require measurement of very weak signals below the noise level. Statistical analysis of COSMIC data indicates that there are compact areas of very strong super-refraction in the marine boundary layer. Negative bias of bending angles is also caused by horizontal gradients resulting in bending angle being multi-valued functions of impact parameter. In this case retrieval algorithm may systematically lose sharp spikes of bending angle profiles.

In this report, we show that negative bias of bending angles correlates with the value of bending angle. Bending angles below 0.025 rad are unbiased, while for larger bending angles the bias increases. This may be used in the assimilation schemes. In particular, bending angles exceeding this value may be either bias-corrected or cut-off.

We reveal another factor resulting in the negative bias of bending angles: random fluctuations of atmospheric refractivity. In our numerical simulations, we modeled turbulence with the Kolmogorov – von Kármán power-law spectrum. We found an effective profile of the structural coefficient $C_N^2(z)$ resulting in realistic values of the fluctuations of simulated signals. With this profile, we found a bias of bending angles proportional to C_N^2 and reaching a realistic magnitude of about 20%. In the end-to-end simulations with ECMWF fields including turbulence, we obtained a realistic pattern of negative bias of refractivity in the tropics. We assume that in nature turbulence must be synergetic with super-refraction, because vertical strong-gradients of density enhance the turbulence strength.

For reference, we performed a statistical analysis of the 55 cases chosen for the previous EUMETSAT WOP-ITT study aimed at the optimization of occultation tracking strategy [25]. It was found that the tropical WOP-ITT cases are located in super-refraction areas. We performed a series of simulations with tropical radiosondes. It was shown that such simulations may overestimate the negative systematic retrieval error in the height range of 1–3 km. On the other hand, simulation based ECMWF with turbulence provide a more realistic patter of N-bias that significantly increase in the lowest 1 km. Thus, we conclude that radiosondes are not good for this type of end to end simulations.

7.1 Acknowledgements

Author is grateful to S. Healy and V. Vorob'ev for useful discussions and to S. S. Leroy for providing access to the high-capacity computation facilities of Harvard University. Work on Section 4.1 was supported by Russian Foundation for Basic Research (grant RFBR No. 12-05-00335-a). Work on Section 4.2 was supported by Russian Science Foundation (grant RSCF No. 14-27-00134).

8. References

1. S. Sokolovskiy, C. Rocken, W. Schreiner, and D. Hunt, On the uncertainty of radio occultation inversions in the lower troposphere, Journal of Geophysical Research, V. 115, D22111, doi:10.1029/2010JD014058, 2010.
2. M. E. Gorbunov and A. S. Gurvich, Algorithms of inversion of Microlab-1 satellite data including effects of multipath propagation, International Journal of Remote Sensing, 1998, 19(12), 2283–2300.
3. M. E. Gorbunov, and A. S. Gurvich, Microlab-1 experiment: multipath effects in the lower troposphere, Journal of Geophysical Research - Atmospheres, 1998, 103(D12), 13,819–13,826.
4. M. E. Gorbunov, Canonical transform method for processing GPS radio occultation data in lower troposphere, Radio Science, 2002, 37(5), 10.1029/2000RS002592, 9-1–9-10.
5. M. E. Gorbunov, and K. B. Lauritsen, Canonical Transform Methods for Radio Occultation Data, Scientific Report 02-10, Danish Meteorological Institute, Copenhagen, Denmark, 2002.
6. M. E. Gorbunov and K. B. Lauritsen, Analysis of wave fields by Fourier Integral Operators and its application for radio occultations, Radio Science, 2004, 39(4), RS4010, doi:10.1029/2003RS002971.
7. M. E. Gorbunov, K. B. Lauritsen, S. S. Leroy, Application of Wigner distribution function for analysis of radio occultations, Radio Science, 2010, V. 45, RS6011, doi:10.1029/2010RS004388.
8. M. E. Gorbunov, K. B. Lauritsen, S. S. Leroy, Analysis of RO data retrieved from the Wigner distribution function, International Radio Occultation Working Group, 2nd Workshop, 28th March – 3rd April 2012, Stanley Hotel in Estes Park, CO, USA, 2012.
9. Jensen, A. S., M. S. Lohmann, H. Benzon, and A. S. Nielsen (2003), Full spectrum inversion of radio occultation signals, Radio Sci., 38(3), 1040, doi:10.1029/2002RS002763.
10. Jensen, A. S., H.-H. Benzon, M. S. Lohmann, and A. S. Nielsen (2006), Processing radio occultation data by full spectrum inversion techniques: An overview and recent developments, in Atmosphere and Climate, Studies by Radio Occultation Methods, edited by U. Foelsche, G. Kirchengast, and A. Steiner, pp. 96–112, Springer, New York.
11. Jensen, A. S., M. S. Lohmann, A. S. Nielsen, and H. Benzon (2004), Geometric optics phase matching of radio occultation signals, Radio Sci., 39, RS3009, doi:10.1029/2003RS002899.
12. Sokolovskiy, S. (2001), Modeling and inverting radio occultation signals in the moist troposphere, Radio Sci., 36(3), 441–458, doi:10.1029/1999RS002273.
13. Sokolovskiy, S. (2003), Effect of superrefraction on inversions of radio occultation signals in the lower troposphere, Radio Sci., 38(3), 1058, doi:10.1029/2002RS002728.
14. F. Xie, D. L. Wu, C. O. Ao, E. R. Kursinski, A. J. Mannucci, and S. Syndergaard, Super-refraction effects on GPS radio occultation refractivity in marine boundary

layers, Geophysical Research Letters, V. 37, L11805, doi:10.1029/2010GL043299, 2010.

15. M. Gorbunov, Wave Optics Propagator Package: Description and User Guide, Technical Report for CONTRACT EUM/CO/10/460000812/CJA Order 4500005632, 2011.
16. M. E. Gorbunov, A. V. Shmakov, S. S. Leroy, and K. B. Lauritsen, COSMIC radio occultation processing: Cross-center comparison and validation, Journal of Atmospheric and Oceanic Technology, 2011, V. 28, No. 6, 737–751, doi: 10.1175/2011JTECHA1489.1.
17. Gorbunov M. E. Ionospheric correction and statistical optimization of radio occultation data. – Radio Science. 2002. V. 37. No. 5. – p. 17-1–17-9, doi: 10.1029/2000RS002370.
18. M. E. Gorbunov, and L. Kornblueh, Analysis and validation of GPS/MET radio occultation data, Journal of Geophysical Research, 2001, 106(D15), 17,161–17,170.
19. M. E. Gorbunov, and L. Kornblueh, Analysis and validation of Challenging Minisatellite Payload (CHAMP) radio occultation data, Journal of Geophysical Research, 2003, 108(D18), 4584, doi:10.1029/2002JD003175.
20. M. E. Gorbunov and G. Kirchengast, Influence of anisotropic turbulence on X/K band radio occultation signals and related transmission retrieval quality, Tech. Rep. for ESA/ESTEC No. 1/2007, 21 pp, Wegener Center, Univ. of Graz, Austria, 2007.
21. M. E. Gorbunov and G. Kirchengast, Fluctuations of radio occultation signals in X/K band in presence of anisotropic turbulence, Radio Science, 2007, V. 42, RS4025, doi:10.1029/2006RS003544.
22. V. I. Tatarskii, Wave propagation in a turbulent medium, MacGraw-Hill, New York, 1961.
23. S. M. Rytov, Yu. A. Kravtsov, and V.I. Tatarskii, Principles of Statistical Radiophysics: Wave Propagation Through Random Media, V. 4, Springer-Verlag, 1989.
24. S.B. Healy, Optimised Tracking Strategies for Radio Occultation, Task 1 – the profile data set, ECMWF Technical Memorandum, October 4, 2011
25. EUMETSAT study on Optimised Tracking Strategies for Radio Occultation (“WOP ITT study”), EUM/CO/10/460000812/CJA, 2011.

9. List of Acronyms

CHAMP	CHAllenging Minisatellite Payload
COSMIC	Constellation Observing System for Meteorology, Ionosphere, and Climate
ECMWF	European Centre for Medium-range Weather Forecasts
EUMETSAT	EUropean organisation for the exploitation of METeorological SATellites
GNSS	Global Navigation Satellite System
GPS	Global Positioning System (USA)
GPS/MET	GPS Meteorology
GRAS	GNSS Receiver for Atmospheric Sounding, carried by Metop
Metop	Meteorological Operational Satellite
NetCDF	Network Common Data Form
NWP	Numerical Weather Prediction
OCC	Radio occultation processing package developed by M. Gorbunov
RO	Radio Occultation
ROM SAF	Radio Occultation Meteorology (ROM) Satellite Application Facility (SAF) (EUMETSAT)
ROPP	Radio Occultation Processing Package developed by ROM SAF
WOP	Wave Optics Propagator package developed by M. Gorbunov
WOP-ITT	EUMETSAT Study on Optimised Tracking Strategies for Radio Occultation